Dissertation

Performance of ATLAS Muon Precision Drift Chambers in a High Radiation Environment

ausgeführt zum Zwecke der Erlangung des Doktorgrades der technischen
Wissenschaften unter der Leitung von

Ao. Univ. Prof. Dr. Christian W. Fabjan

Atominstitut der Österreichischen Universitäten (E141)

eingereicht an der Technischen Universität Wien
Technisch-Naturwissenschaftliche Fakultät

von

Dipl.-Ing. Claus Cernoch

Matrikelnummer: 9325777
geboren am 4. April 1974
Wulzendorfstrasse 48, A-1220 Wien

Genf, am 27. August 2003

Kurzfassung

ATLAS ist ein Universalexperiment für den zukünftigen Large Hadron Collider (LHC) am CERN, welches es ermöglichen wird in neue Gebiete der elementaren Physik vorzudringen. Dabei wird ein Energiebereich erschlossen, welcher weit über jenen heutiger Experimente hinausreicht. Das Müonenspektrometer des ATLAS-Detektors benötigt Präzisionsdriftkammern mit einer Gesamtfläche von $5500\,m^2$, mit welchen die Müonenbahnen in einem Magnetfeld von $\sim 0.5\,T$ rekonstruiert werden. Etwa 370 000 Driftrohre, gefüllt mit $800\,m^3$ Driftgas (Ar-CO_2 Gasmischung), bilden an die 1200 dieser Driftkammern (Monitored Drift Tubes MDT), mit welchen eine Impulsauflösung von $10\,\%$ für Müonen mit einem Transversalimpuls von $p_T = 1\,TeV$ erreicht werden soll, um das volle Entdeckungspotential des LHC auszuschöpfen. Dieses ambitionierte Ziel muss selbst bei dem auftretenden Photonen- und Neutronenhintergrund erfüllt werden, welcher zu Hintergrundzählraten von bis zu $300\,kHz$ pro Driftrohr führt. Diese Hintergrundstrahlung bewirkt einerseits eine Verschlechterung der Detektoreigenschaften und kann andererseits Alterungsprozesse an den Elektroden hervorrufen.

In der vorliegenden Arbeit wurde zum ersten Mal ein Langzeittest einer MDT-Kammer in einer Hochratenumgebung durchgeführt, vergleichbar der im ATLAS-Betrieb. Auch die nötige Infrastruktur der Driftkammer wurde weitgehend dem Endsystem entsprechend realisiert: Eine Ausleseelektronik ähnlich der Endversion wurde zur Driftzeitdatennahme verwendet und ein Prototyp eines zirkulierenden Gassystems versorgte die Kammer. In dieser Arbeit wurde dieser hochreine Gassystemprototyp mit samt seiner Ansteuerung konzipiert, technisch realisiert und auf Stabilität und Verhalten im Dauerbetrieb getestet. Die gewonnenen Erfahrungen bestätigten die Umsetzbarkeit des Konzeptes fuer das entgültige MDT Gassystem.

Weiters wurden die Auswirkungen der Gaszirkulation auf das Alterungsverhalten im Detail studiert, indem eine Hälfte der Kammer zirkulierend und die andere im Durchfluss betrieben wurde. Im Laufe des Alterungstests wurde von den Driftrohren eine Ladung aufgenommen, welche jener entspricht, die während 4 Jahren ATLAS-Betrieb im schlimmst angenommenen Fall anfallen würden. Das Signalverhalten der Driftrohre wurde im Laufe des Langzeittests mit Refenzmessungen kosmischer Müonen verfolgt. Der Test zeigte keine Art von Alterung in den Rohren des offenen Gassytems bei der akkumulierten Strahlungsdosis. Die Driftrohre, welche vom zirkulierenden System versorgt wurden, zeigten ein Sinken der Pulshöhen in den ersten $\sim 30\,cm$ der Seite des Gaseinlasses. Dieser Effekt wurde ausführlich untersucht und als Silikonpolymerisation am Anodendraht identifiziert – ein Indiz dafür, dass die Alterung nicht durch das zirkulierende Driftgas selbst verursacht wurde, sondern durch Gasverunreinigungen. Letztendlich wurde der Ursprung der Verunreinigung ausfindig gemacht. Die Ergebnisse dieses Tests haben einen wesentlichen Einfluß auf die Konstruktion des MDT Gassystems.

Abstract

ATLAS (A Large Toroidal LHC ApparatuS) is a general-purpose experiment for the future Large Hadron Collider (LHC) at CERN which will offer the opportunity to explore new aspects of fundamental physics by advancing to an energy scale well beyond that achieved by current experiments. The muon spectrometer of the ATLAS detector requires an area of around $5500\,m^2$ of precision tracking chambers, which will reconstruct the muon tracks in a magnetic field of $\sim 0.5\,T$. Approximately 370 000 high pressure drift tubes (MDTs), filled with $800\,m^3$ drift gas (Ar-CO$_2$ gas mixture), form about 1200 of these tracking chambers, aiming to reach a momentum resolution of 10 % for muons with a transverse momentum of $p_T = 1\,TeV$, to exploit the LHC physics discovery range. This demanding performance requirement has to be fulfilled in the presence of a very high particle background of photons and neutrons leading to background counting rates of up to $300\,kHz$ per drift tube. This background irradiation deteriorates the detector performance and may induce ageing processes on the electrodes.

In the presented work for the first time a long-term study with a MDT chamber in a high-background environment, similar to the ATLAS operational environment, has been performed. Also the required infrastructure of the drift chamber was to a large extend realised according to the final system: A front-end electronics close to the final version was utilised to take drift time data and a recirculating gas prototype was supplying the chamber. Within this work the high purity gas prototype and its control system was designed, realised and tested for stability and system behaviour in permanent operation. The gained experiences certified the feasibility of the final MDT gas system.

Moreover the impact of gas recirculation on the ageing behaviour of the drift chamber was studied in detail, by operating half of the chamber in recirculated and the other half in flushed gas mode. In the course of the ageing test a charge corresponding to 4 years of ATLAS operation, assuming a conservative worst-case irradiation, were accumulated by the drift tubes. The signal pulseheight spectra of the MDTs were followed up with reference measurements of cosmic muons during this long-term test. The test proved that no ageing occurred in the drift tubes of the open gas system within the accumulated irradiation dose. The drift tubes connected to the circulated gas system showed a local pulseheight drop in the first $\sim 30\,cm$ on the gas inlet side. This effect was studied intensively and found to be caused by silicone polymerisation on the anode wire – an evidence that the ageing was not caused by the drift gas and gas circulation itself, but by accumulating gas impurities. The source of the contamination was found eventually. The results of this test has a significant influence on the construction of the MDT gas system.

Acknowledgements

Meinen Eltern
in Dankbarkeit
gewidmet

Contents

Chapter 1

Introduction

1.1 The Standard Model

According to the theoretical developments and experimental discoveries of the past decades a set of theories has emerged, that describes all of the known elementary particle interactions except gravity. The current understanding of the nature of matter and their interaction forces is summarised in the so-called Standard Model of particle physics, which incorporates the Glashow-Weinberg-Salam theory of electro-weak processes and Quantum Chromodynamics (QCD) of strong interactions. In the view of the Standard Model, all matter is made of two kinds of elementary particles: leptons and quarks. The interactions between these particles are explained via the exchange of force mediator particles. The particles building matter are called fermions, which have half-integer spin, whereas the particles mediating forces are called bosons with integer spin.

gener-ation	Leptons ($S = \frac{1}{2}$)			Quarks ($S = \frac{1}{2}$)		
	flavour	mass $[GeV/c^2]$	electric charge	flavour	mass $[GeV/c^2]$	electric charge
1	ν_e electron neutrino	$< 1.5 \times 10^{-5}$	0	**u** up	3×10^{-3}	$+\frac{2}{3}$
	e electron	0.511×10^{-3}	-1	**d** down	6×10^{-3}	$-\frac{1}{3}$
2	ν_μ muon neutrino	$< 0.19 \times 10^{-3}$	0	**c** charm	1.3	$+\frac{2}{3}$
	μ muon	0.106	-1	**s** strange	0.1	$-\frac{1}{3}$
3	ν_τ tau neutrino	< 0.018	0	**t** top	175	$+\frac{2}{3}$
	τ tau	1.777	-1	**b** strange	4.3	$-\frac{1}{3}$

Table 1.1: Basic properties of the fundamental fermions [1]

The fundamental fermions, classified in leptons and quarks, can be grouped further into three generations as shown in table 1.1. Each generation consists of two quarks and

two leptons. The elements of the first generation make up the stable matter which surrounds us. Protons and neutrons, as building blocks of every atomic nucleus, are actually a combination of three first generation quarks, *uud* for the proton and *udd* for the neutron. The particles of the other generations are heavier and only exist in cosmic radiation or in man-made particle sources.

Each particle of table 1.1 has a corresponding anti-particle with opposite electric charge respectively opposite charge of the strong interaction, called colour charge. All fundamental fermions have been detected experimentally[1].

interaction:	gravitational	weak	electromagnetic	strong
acts on:	mass - energy	flavour	electric charge	colour charge
particles experiencing:	all	quarks, leptons	charged particles	quarks, gluons
particles mediating:	graviton	W^+, W^-, Z^0	γ	gluons
mass of the mediators:	0	$m_{W^\pm} = 80.4 \frac{GeV}{c^2}$ $m_{Z^0} = 91.2 \frac{GeV}{c^2}$	0	0
rel. strength[2] at: $10^{-18}m$	10^{-41}	0.8	1	25
$3 \times 10^{-17}m$	10^{-41}	10^{-4}	1	60

Table 1.2: Basic properties of the fundamental interactions and their mediator particles [1]

Every type of interaction has its force mediator particle. The graviton, the mediator particle of the gravitational field, must have a rest mass of zero due to the long range of the **gravitational interaction**. Although there is indirect astronomical evidence, laboratory searches have not yet yielded direct proof of the existence of gravitons, as their effects, which can be studied on a laboratory scale, are very small. The gravitational force couples to the mass of all particles and is always attractive. In contrast to the electromagnetic and strong force it therefore is not vanishing on a macroscopic scale, despite of its intrinsic weakness. For high energy physics, the gravitational force is of minor importance since the masses of currently known elementary particles are very far below the scale where gravity would become appreciable.

The mediator bosons of the other three interactions have been observed in experiments and are included in the Standard Model. The **electromagnetic interaction** is described in extremely good agreement with experiments by quantum electrodynamics (QED). It explains the force between particles carrying electric charge via a massless spin 1 gauge boson, the photon.

The **weak interaction** is mediated by three massive bosons W^+, W^- and Z^0. The $W^\pm$ exchange results in change of charge of the lepton or hadron[3] taking part in the

---

[1]A historical overview of the discovery of elementary particles is for example given in [2]

[2]relative to the electromagnetic interaction between two *u* quarks at the specified distance

[3]A hadron is a particle consisting of two or more quarks.

interaction and is called charged-current reaction, while the Z^0 exchange does not, and is called a neutral-current reaction. The weak interaction acts on all constituents of matter. Due to the heavy masses of the mediating bosons it is very weak at low energies, and is covered by the electromagnetic and strong interaction, unless these are forbidden by conservation rules. The electromagnetic and weak force are described within the Standard Model in the framework of the electroweak model, a gauge field theory with the symmetry group $SU(2) \times U(1)$. It has been checked that the couplings of quarks and leptons to the weak gauge bosons are indeed precisely as described by the gauge symmetry, which verified that the gauge symmetry is unbroken. On the other hand there is immediate evidence that the symmetry is strongly broken for the particle masses. In fact $SU(2) \times U(1)$ gauge symmetry does not include masses for any of the particles which have been observed so far. Thus, the currents are conserved but the particle states are not symmetric, which is called spontaneous symmetry breaking.

The simplest implementation of spontaneous symmetry breaking is via the Higgs mechanism [3]. The Higgs particle itself has not been found so far. Although within the model there is no guidance about the Higgs mass itself, some constraints can be derived from perturbative calculations within the Standard Model, leading to a favoured Standard Model Higgs boson mass range[4] of $100 - 170\,GeV$. If the Higgs will not be found in this region new physics beyond the Standard Model is expected.

The mediators of the **strong interaction** are 8 massless gluons. This interactions takes place between the constituent quarks which make up hadrons. While for the electromagnetism there are only two charges, in the theory of the strong force, the quantum chromodynamics (QCD), there are six types of strong charge, called colour. A quark can carry one of the three colours and an antiquark the corresponding anticolour. Colour symmetry is supposed to be exact, that is the quark-quark force is independent of the colours involved.

The exact nature of the various couplings has been determined with high precision and is based on many experiments, in particular on the experiments performed at the LEP[5] collider at CERN (Geneva, Switzerland) from 1989 to 2000. The goal to discover the origin of the spontaneous symmetry breaking mechanism in the electroweak sector of the Standard Model, and hence explaining the origin of the different particle masses, is one of the main reasons to construct the Large Hadron Collider (LHC) at CERN. Furthermore searches for supersymmetric particles, heavy quark systems, as well as investigations of theories which go beyond the Minimal Standard Model will guide the physics program at the future LHC.

1.2   The Large Hadron Collider

The discussion of the Standard Model and some of its extensions shows that there are good reasons to expect very interesting physics at the TeV energy scale. In order to explore it, the LHC [5] is currently built at CERN [6], the European Organisation for

---

[4]a lower limit $m_H > 114\,GeV$ was established at the upgraded LEP2 [4]

[5]Large Electron Positron collider
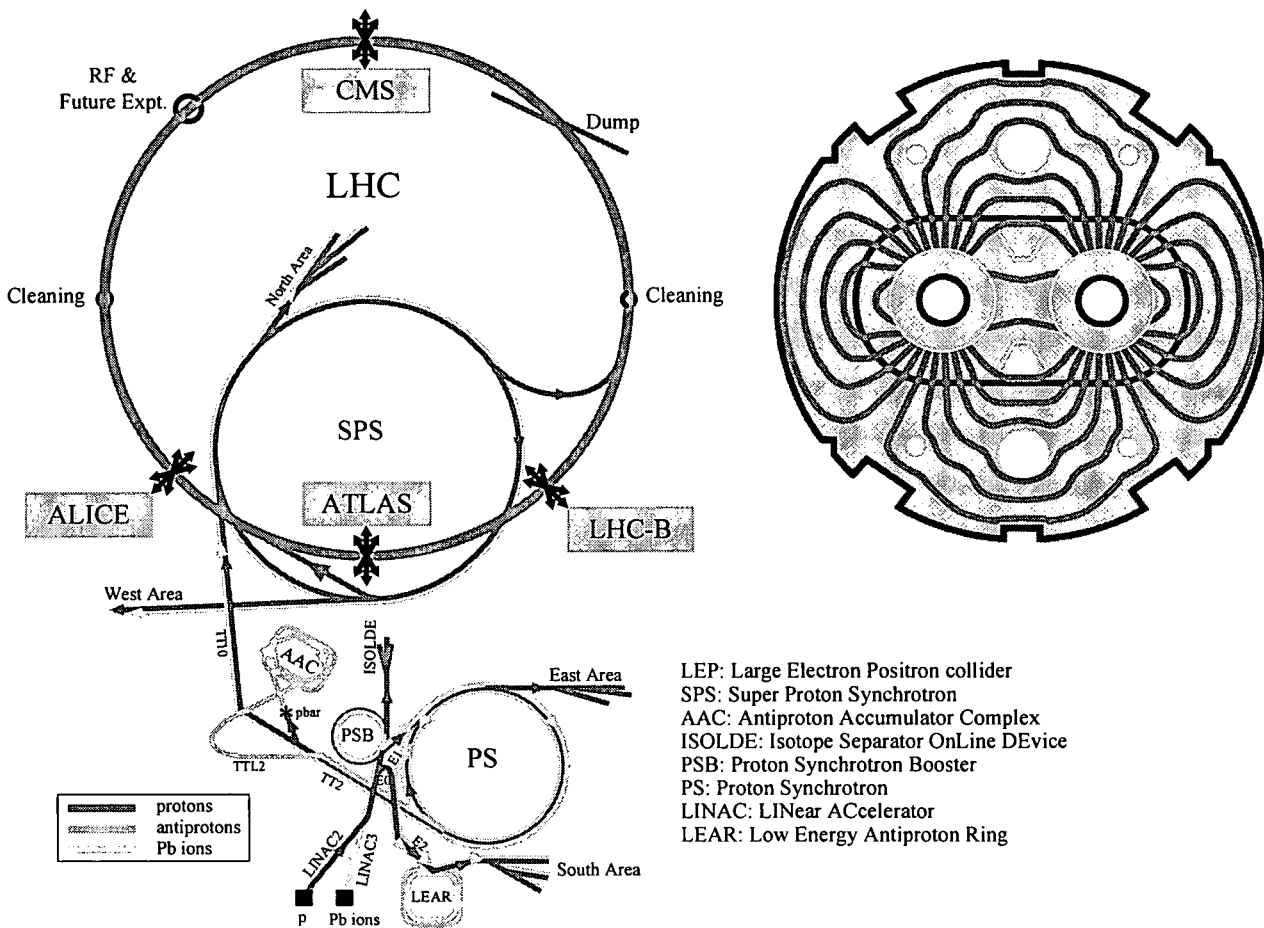
Figure 1.1: *left:* illustration of the LHC accelerator complex; *right:* schematic of the cross-section of the LHC twin dipoles

Nuclear Research in Geneva, and will become operational in 2007. This accelerator will collide protons at a center of mass energy of $7 + 7\ TeV$, at a design luminosity of $10^{34}\ cm^{-2}\ s^{-1}$ (or $10\ nb^{-1}\ s^{-1}$), which surpasses the highest luminosity reached ever before in a hadron collider by almost two orders of magnitude. Such conditions will recreate the environment thought to have existed $10^{-12}\ s$ after the Big Bang, when the temperature of the universe was 10^{16} degrees. Moreover the LHC will also be capable of colliding heavy ions such as lead, to study quark-gluon plasma, quark confinement and the collective effects of strong interactions, as were thought to have occurred $10^{-6}\ s$ after the Big Bang.

The LHC is constructed in the existing $27\ km$ tunnel at CERN, which formerly was housing the LEP machine. A schematic view of the LHC injection and acceleration scheme is shown in figure 1.1. Illustrated in the same figure are the circular Proton Synchrotron (PS) and Super Proton Synchrotron (SPS) accelerators, which served many experiments at CERN over the past decades and which will serve the LHC for the decades to come. The 630 m circumference PS, the oldest accelerator of CERN, was commissioned

in 1959 and has been in use to (pre-) accelerate protons, antiprotons, electrons, positrons and heavy ions. The SPS was operated in the 1980's as a $p\bar{p}$ colliding beam machine, the $Sp\bar{p}S$, which led to the first observation of the Z^0 and $W^{\pm}$ particles.

For the forthcoming LHC operation the produced protons are boosted by a dedicated $50\,MeV$ linear accelerator (LINAC) and a small circular accelerator, the $1.4\,GeV$ Proton Synchrotron Booster (PSB), before they are injected into the PS. The PS further increases the energy of the particles to $25\,GeV$ and injects them into the next element of the CERN acceleration chain: the 7 km circumference SPS. For the forthcoming LHC operation, the SPS will accelerate the protons up to an energy of $450\,GeV$ before injecting them into the LHC. Once in the LHC, the protons are accelerated up to the full LHC beam energy of $7\,TeV$.

Before the LHC, high center-of-mass energy colliders, like the LEP and the TEVATRON[6], always used collisions between particles and their anti-particles. The LHC opted for a scheme with proton-proton collisions, because high intensity proton beams are easier to realise than high intensity anti-proton beams. As a consequence, the LHC requires separate vacuum pipes for each proton beam, which demands a novel design of the superconductive dipole bending magnets: the twin aperture dipoles (see figure 1.1). These dipoles share a common yoke and cryostat to realise the opposite $8.3\,T$ magnetic fields to keep the two proton beams rotating on orbit in opposite directions. This twin dipole concept saves both space and cost. The magnet system consisting of 1232 superconductive dipole magnets, each of $14.3\,m$ length, which have to be cooled down in superfluid helium at temperatures below $2\,K$.

energy at injection	$450\,GeV$
energy at collision	$7\,TeV$
energy loss per turn	$6.7\,keV$
luminosity	$10^{34}\,cm^{-2}\,s^{-1}$
dipole field	$8.33\,T$
bunch spacing	$7.48\,m$
bunch separation	$24.95\,ns$
filled/total bunches	$2835/3564$
number of particles per bunch	1.1×10^{11}
beam lifetime	$10\,h$
beam current	$0.54\,A$
radiated power per beam	$3.8\,kW$
stored energy per beam	$350\,MJ$

Table 1.3: principle design parameters of the LHC machine [7]

A summary of the basic design parameters of the LHC is given in table 1.3. A bunch of protons will make one turn of the machine every $88.92\,\mu s$ and approximately $20\,\%$ will be

---

[6] a proton-antiproton collider at the Fermilab (Chicago, USA) with an interaction energy of $1.96\,TeV$ and a typical luminositiy of $0.016\,nb^{-1}s^{-1}$

empty to allow proton injection and extraction. The LHC will generate a continuously running clock signal at $40.08\,MHz$ to provide the synchronisation with the four LHC experiments. At the interaction points of the experiments, the bunches will have a transverse radius of $16\,\mu m$ and the length of a bunch will be $30\,cm$.

1.3   Experiments at the LHC

To exploit the full discovery potential of the LHC two general-purpose pp detectors (ATLAS and CMS) are installed at the beam crossings (see figure 1.1). In addition two specialised experiments (LHC-B and ALICE) are built.

- **ATLAS** (A Toroidal LHC ApparatuS) is characterised by two different magnetic field systems: A super-conducting solenoid will be installed around the Inner Detector cavity and large super-conducting air-core toroids consisting of independent coils will be arranged outside the calorimetry. This concept offers almost no constraints on calorimetry and inner detector, allowing non-compromised technological solutions and a high-resolution, large acceptance and robust muon spectrometer with excellent stand-alone capabilities. The next section is dedicated to the description of this experiment.

- **CMS** (Compact Muon Solenoid) has been optimised for the search of the standard model Higgs boson, but allows detection of a wide range of possible signatures from alternative electro-weak symmetry breaking mechanisms and is well adapted for the study of top, beauty, and tau physics at low luminosities. At the core of the CMS detector sits a large super-conduction solenoid generating a uniform magnetic field of $4\,T$. The choice of a strong field leads to a compact design for the muon spectrometer without compromising the momentum resolution up to rapidities of $\eta = 2.5$.

- **LHC-B**: This dedicated B-physics experiment at the LHC is an optimised open-geometry forward collider detector, which is designed to fully exploit the B-physics potential of the LHC. The large Lorentz boost of accepted B-mesons allows precise decay time measurements, which are complemented by excellent particle identification and efficient muon triggers.

- **ALICE** (A Large Ion Collider Experiment) is a general purpose heavy ion experiment designed to measure the flavour content and phase space distribution, event by event, for a large number of particles whose momenta and masses are of the order of the typical energy scale involved ($\Lambda_{QCD} \approx 200\,MeV$). In addition to addressing particular signals which look most promising today, ALICE will search for qualitative and quantitative differences between proton-proton and nucleus-nucleus collisions. An open geometry will facilitate future modifications and upgrades, if first physics results suggest focusing on specific signals, selective triggers or large acceptance.

The detailed descriptions of the experimental set-up of these detectors and their design considerations can be found in the respective detector technical proposals [8], [9], [10] and [11].

1.4 The ATLAS Detector
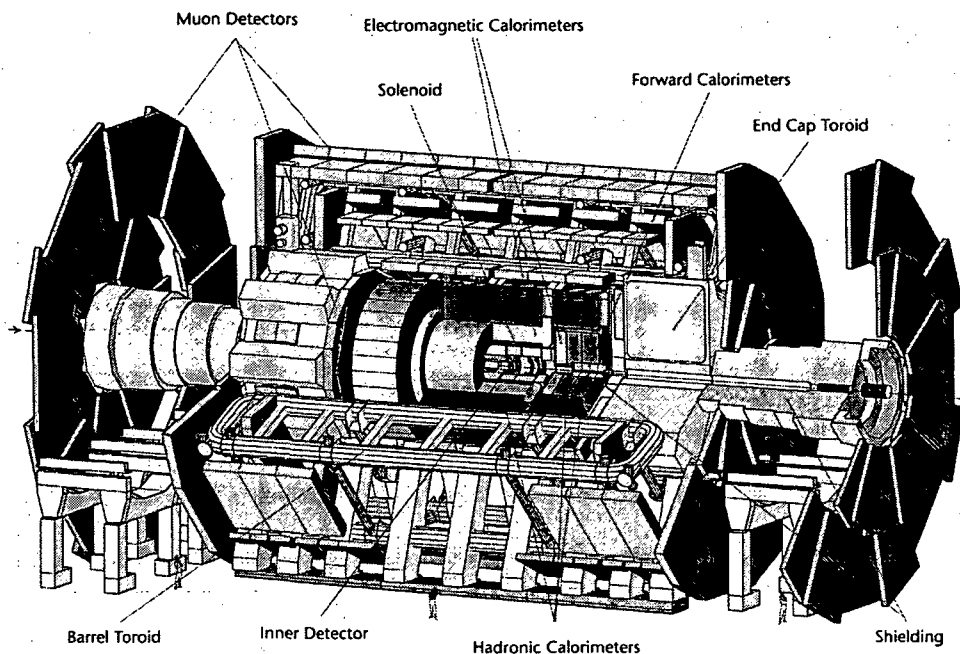
Figure 1.2: Three dimensional cut-away view of the ATLAS detector

Figure 1.2 shows a three dimensional cut-away view of the ATLAS detector. The inner detector surrounds the beam line and measures the trajectories, and thereby the momenta, of charged particles. A super-conducting solenoid, which generates a homogeneous $2T$ magnetic field in the inner detector volume, closes the inner detector. Directly outside this solenoid the electromagnetic and hadronic calorimeters are located. These calorimeters measure the energy of all particles, except muons and neutrinos. The outermost shell of the ATLAS detector is formed by the muon spectrometer, which measures the trajectories, and thereby the momenta, of muons, the only charged particles that are not stopped in the calorimeters. The magnetic field in thee muon spectrometer region is realised by three huge super-conducting air-core toroids. The average magnetic field strength is about $0.5T$.

1.4.1 The Inner Detector

The inner detector [12] (shown in figure 1.3) has to cope with the enormous event rate inherent to the LHC running environment. To keep the single channel occupancy at a modest level, a very high granularity is required. About 140 million silicon pixels for
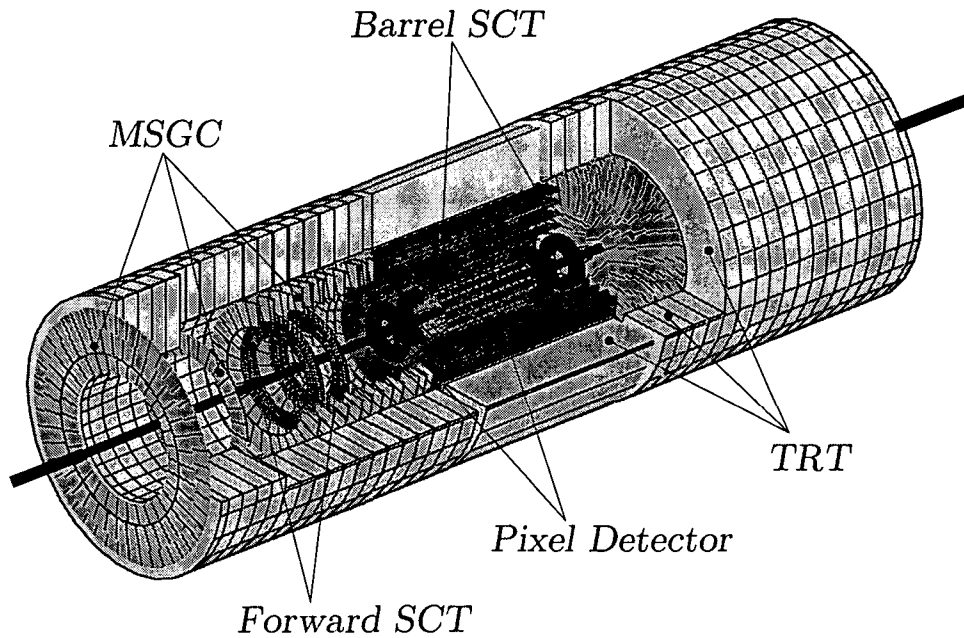
Figure 1.3: schematic view of the ATLAS inner detector consisting of the silicon pixel vertex detector, the Semi Conductor Tracker (SCT) and the Transition Radiation Tracker (TRT)

the detector nearest to the beam line, about 6 million silicon strips for the detector at intermediate distance from the beam line, and close to 370.000 straw tubes for the exterior detector. Together these three sub-detector systems fulfil the physics specification, which is, apart from the need to measure charged particle momenta, notably driven by the requirement to be able to tag long lived particles, which is a distinct feature of b-quark production. b-quarks are important in view of the large $H \to b\bar{b}$ branching ratio, in view of the study of CP violation in the B-system and in view of the dominant $t \to bW$ decay of t-quarks. The $2\,T$ solenoidal magnetic field together with the configuration chosen for the ATLAS detector typically achieves a momentum resolution of $\Delta p_T/p_T = 0.04\% \times p_T \oplus 2\%$ (p_T in GeV/c) and an impact parameter resolution of $15\,\mu m$.

The straw tubes occupy the $7\,m$ long shell with inner radius $0.6\,m$ and outer radius $1.1\,m$. The basic detector element is a gas-filled $4\,mm$ diameter straw tube operated as a standard drift tube. The straws are mounted together to form disks in the forward regions with radial straws and to form barrels in the central region with longitudinal straws. The large number of straws traversed by a single particle (typically 36) is crucial for the pattern recognition in the inner detector. The straw layers are interleaved with a radiator material to produce transition-radiation photons when very relativistic particles pass through. The straw tracker is therefore usually referred to as the **Transition Radiation Tracker** (TRT). The transition-radiation photons allows separation of ultra-relativistic particles (typically electrons) from the enormous $\pi^{\pm}$ background.

The silicon strip detectors, **Semi Conductor Tracker** (SCT) are stacked in a similar

fashion as the straw tubes, arranged as disks in the forward regions and as barrels in the central region. The strip pitch is $80\,\mu m$, and on average one track hits four strip layers. Despite the small number of silicon strips hit by a single particle, compared to the large number of TRT hits, the momentum resolution is significantly improved after the inclusion of the silicon strip hits. This is the result of the high spatial resolution of the individual silicon detector elements.

The **Silicon Pixel Vertex** detector, with a $50 \times 300\,\mu m^2$ pixel size, is again organised in disk and barrel structures. Even though on average a track traverses only three silicon pixel layers, the impact parameter resolution is mainly determined by this sub-detector system because it is mounted nearest to the beam line.

1.4.2 The Calorimeters
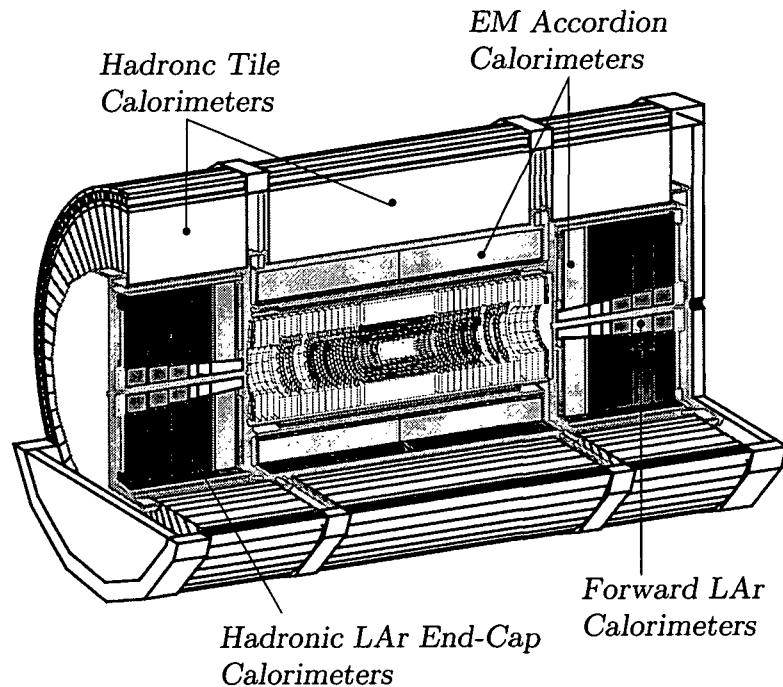
Figure 1.4: Schematic view of the ATLAS calorimetry system

The calorimeters [13] (shown in figure 1.4) are crucial for the discovery of a low mass Standard Model Higgs particle via the $H \rightarrow \gamma\gamma$ decay. They are also well suited to discover physics beyond the Standard Model using missing (transverse) energy as a signature. ATLAS has, like most colliding-beam high-energy physics experiments, two types of calorimeters: an electromagnetic calorimeter situated directly outside of the solenoid magnet of the inner detector, and a hadronic calorimeter is surrounding the electromagnetic one. Good photon identification capabilities call for a finely segmented electromagnetic calorimeter. Accurate jet energy measurement and excellent missing energy reconstruction requirements demand a large rapidity coverage. The ATLAS calorimeters therefore extend up to $\eta = 4.9$.

The **electromagnetic calorimeter** [14] is of the sampling type with accordion shaped lead absorber plates as passive medium interleaved with liquid argon as active medium. The ionisation charge created in the liquid argon gaps is collected on copper platted Kapton electrodes longitudinally segmented into three sections. The rapidity segmentation $\Delta\eta$ varies from 0.003 to 0.1, and the azimuthal segmentation $\Delta\Phi$ varies from 0.025 to 0.1. The total number of read-out channels is about 170 000. The thickness exceeds 24 radiation lengths in the barrel region and 26 radiation lengths in the end cap region. The energy resolution is $\Delta E/E = 11.5\%/\sqrt{E} \oplus 0.5\%$ (E in GeV). Due to the tight space constraints in the forward regions, a different layout is used with tungsten or copper instead of lead as passive absorber material.

The **hadronic calorimeter** [15] is of the sampling type, with iron absorber plates as passive medium and scintillating tiles as active medium. A novel feature of this calorimeter is the non-standard orientation of the scintillating tiles, placed in the radial direction and staggered in depth. This particular layout allows routing of the read-out fibres of the scintillators while maintaining the hermeticity of the calorimeter. The hermeticity is important in view of the missing energy reconstruction performance. The granularity in $\Delta\eta \times \Delta\Phi$ equals 0.1×0.1 . The total number of read-out channels is about 10 000. The total thickness exceeds 10 interaction lengths. Jets are reconstructed with an energy resolution of $\Delta E/E = 50\%/\sqrt{E} \oplus 3\%$ (E in GeV).

1.4.3   The Muon Spectrometer

The Muon spectrometer [16], as the outermost subdetector, dominates the huge size[7] of the ATLAS experiment. Its accurate muon momentum measurement is based on the magnetic deflection of the muon tracks, which is completely independent of the inner detector. This is achieved by integrating three large subsystems as shown in figure 1.5 and 1.6:

- The toroidal magnetic field is generated by a large air-core barrel toroid and two air-core end-cap toroids. Each toroid consists of eight super-conducting coils, producing an average magnetic field of $0.5\,T$. During ATLAS operation, the magnetic field is measured by a large number of three dimensional Hall probes mounted throughout the muon spectrometer volume.

- The muon first level trigger is extracted from the fast signals of dedicated trigger chambers: Resistive Plate Chambers (RPC's) with about 355 000 channels in the barrel region and Thin Gap Chambers (TGC's) with about 440 000 channels in the end-cap regions. These trigger chambers also determine the global reference time (bunch crossing identification) and the muon track coordinate in the non-bending direction with a spatial resolution of $5 - 10\,mm$.

- The muon tracks, and thereby the muon momentum, is measured with high precision by the Monitored Drift Tube (MDT) chambers. Only in the innermost ring of the end-cap inner-station ($2 < |\eta| < 2.7$), where particle fluxes are highest, Cathode Strip Chambers (CSC) are in use. The about 1200 MDT chambers amount

---

[7]a cylindrical volume of roughly $40\,m$ length and almost $24\,m$ diameter
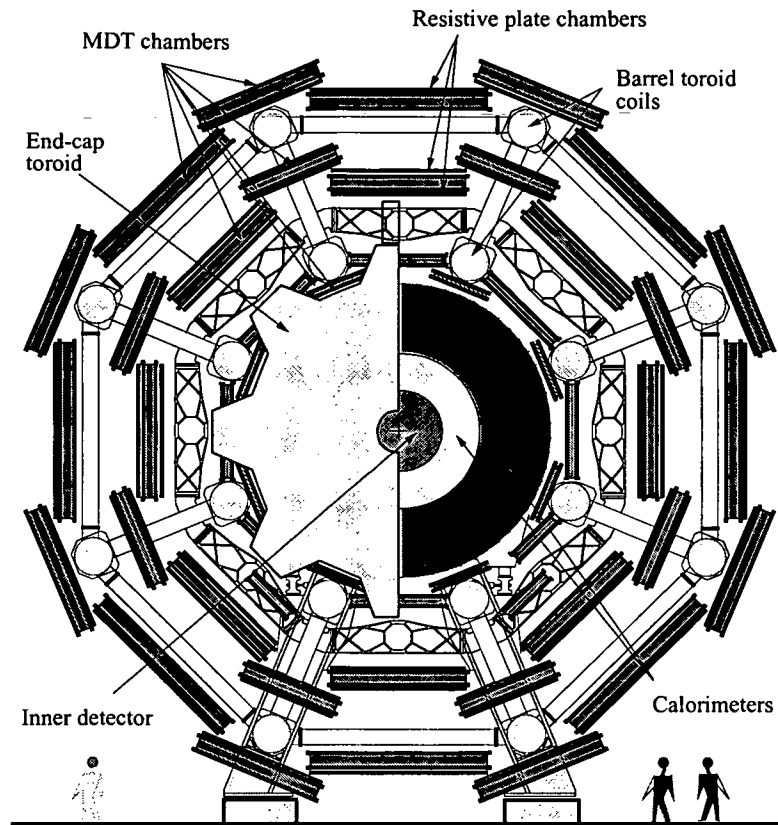
Figure 1.5: Transverse view of the barrel of the ATLAS muon spectrometer
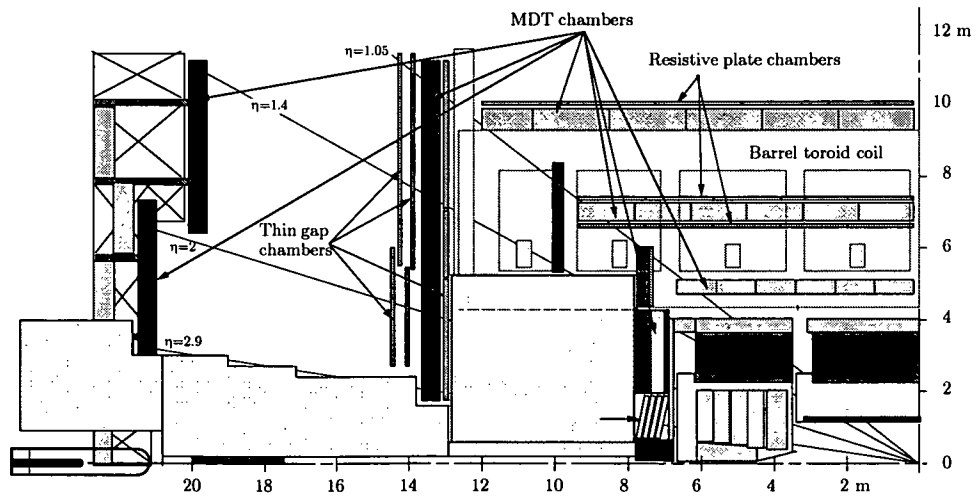
Figure 1.6: Longitudinal view of one quadrant of the ATLAS muon spectrometer

to a total of about 370,000 MDT channels. A single MDT measures a point on the trajectory of a muon with a precision of about $80\,\mu m$ in the bending direction. The relative positions of the MDT chambers are monitored by several thousand alignment sensors.

Together these systems allow a muon momentum measurement with a precision ranging from 2 to 3 % for $10 - 200\,GeV$ muons to about 10 % for $1\,TeV$ muons. This precision is more than adequate for the discovery of the Higgs particle using the $H \rightarrow \mu^+\mu^-\mu^+\mu^-$ decay channel. The muon spectrometer is also well suited to explore physics beyond the Standard Model whenever energetic muons are involved. Examples are a heavy supersymmetric Higgs A^0 in the $A^0 \rightarrow \mu^+\mu^-$ decay and the $Z' \rightarrow \mu^+\mu^-$ decay of a heavy Z' boson.

The MDT, RPC and TGC detectors are positioned at three locations along a muon track. In the barrel, the three detector stations (see figure 1.6) are mounted concentrically around the beam line at $5\,m$ (inner), $7\,m$ (middle) and $10\,m$ (outer) radial distance. In the end-cap, the disks are mounted perpendicular to the beam line at $9\,m$ (inner), $14\,m$ (middle) and $20\,m$ (outer) from the interaction point. With the barrel geometry the muon momentum can be determined accurately from the measured sagitta, defined as the distance from the point measured in the middle station to the straight line connecting the points in the inner and outer stations.

Within the end-cap geometry, with only a magnetic field in between the inner and middle stations, the momentum is determined with a point-angle measurement provided by one point in the inner station and an angle in the combined middle-outer stations. In the azimuthal (non-bending) direction, the assembly follows the eight-fold symmetry of the toroids, with in each octant small chambers, centered at the magnet coils, and large chambers in between adjacent magnet coils.

1.5 The Trigger System

The ATLAS trigger system [17] is designed to select a manageable number of events out of the overwhelming number of primary interactions. For LHC running at high-luminosity , the total proton-proton interaction rate reaches $1\,GHz$, and the ATLAS experiment must make it possible to pick out the interesting events, like evidence for Higgs production, hints of physics beyond the Standard Model, etc. To make this possible the usual strategy is a step-wise reduction procedure. The first steps are a real time pre-selection of interesting events ("triggering") to reduce the huge $40\,MHz$ bunch crossing rate to a manageable event rate of about $100\,Hz$, which are written to mass storage devices. The full reconstruction of the stored date takes place in the last step to yield quantities like tracks, energy clusters, jets, missing transverse energy, secondary decay vertices, etc. These quantities are subject to various physics selection criteria in offline analysis, for example to maximise the discovery potential for the Higgs particle. This paragraph outlines the online data reduction (trigger) scheme shown in figure 1.7.

The **first level trigger** (LVL1) is designed to operate at a maximum pass rate of $75\,kHz$. The LVL1 decision time (called latency) is $2\,\mu s$. The information of all detector channels

Latency   Rate

CALO   MUON   TRACKING

40 Mhz

LVL1
~2µs
(fixed)   pipline memories

75 kHz
                                               de-randomizing
                                               buffers

MUX   MUX   MUX   multiplex data

                                               digital buffer
                                               memories

LVL2   1 kHz

~1-10 ms
(variable)   Readout / Event Building   ~1-10 G B / s

                                               switch-farm
                                               interface
LVL3
processor
farm

                                               100 Hz

Data Storage

~10-100 M B / s
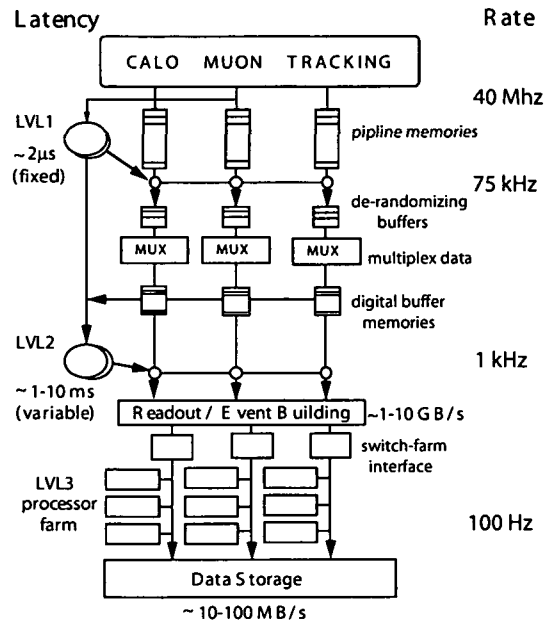
Figure 1.7: Functional schematic of the ATLAS Trigger/DAQ system

must be stored in pipeline memories, because the LVL1 latency extends over many of the 25 ns spaced LHC bunch crossings. The LVL1 decision is based on information with a coarse granularity of two sub-detector systems: the muon trigger chambers and the calorimeters. Quantities used in the LVL1 decision are typically: the estimated transverse momentum of muon candidates, the total energy deposited in the calorimeters, the missing (transverse) energy in the calorimeters and the occurrence of isolated energy depositions in the calorimeters. For events accepted by the LVL1, the information of all sub-detector systems is pre-processed and stored in the so-called Read-Out Buffers (ROB's).

The **second level trigger** (LVL2) uses both the LVL1 output and the data stored in the ROB's to further reduce the data rate to a maximum of 1 kHz. Even though the LVL2 has access to the full data, the selection is generally restricted to so-called Regions of Interest as flagged by the output of the LVL1. For a LVL1 muon trigger, the LVL2 will use the information from the precision MDT chambers to improve the muon momentum estimate, which allows a tighter cut on this quantity. For a LVL1 calorimeter trigger, the LVL2 has access to the full detector granularity, and has in addition the possibility to require a match with a track reconstructed in the inner detector. The LVL2 has an event dependent latency, which varies from 1 ms for simple events to about 10 ms for complicated events. For events accepted by the LVL2, the data fragments stored in the ROB's are collected by the so-called Event Builder and written into the Full Event Buffers.

The **third level trigger** stage is called LVL3 and uses the information stored in the Full Event Buffers to keep the event rate sent to mass storage below 100 Hz. The LVL3
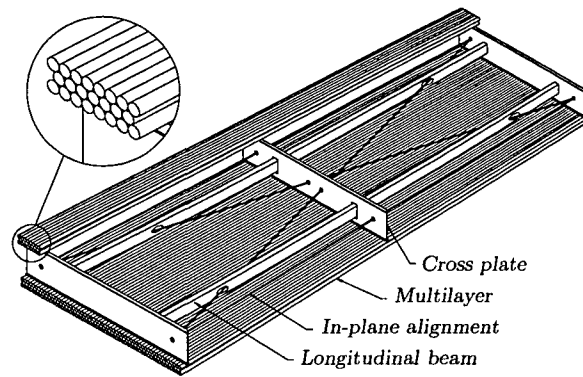
Figure 1.8: Three (or four) layers of MDT tubes are glued from each side to a support frame to form the two multilayers of a MDT chamber

can use complex offline algorithms like track reconstruction, vertex finding, etc., because it has access to the complete event. For the maximum trigger rate of $100\,Hz$, the data rate written to mass storage corresponds to $100\,MByte/s$. As one nominal LHC running year is estimated to be around $10^7\,s$ the recorded data amounts to a annually volume of $1\,PByte$ $(10^9\,MByte)$.

1.6   The Muon Precision Drift Chambers

As quoted in section 1.4.3 the sagittas of muon tracks are measured by precision drift chambers in an inner, middle and outer muon station. A $p_T = 1\,TeV$ muon shows a sagitta of $\approx 500\,\mu m$ in the average magnetic field of $0.5\,T$. Therefore a momentum resolution of 10 % requires a sagitta measurement accuracy of $50\,\mu m$. Given the large size of the spectrometer it is impossible to keep the shape of the muon chambers and their positions stable within this tracking accuracy. Instead a different concept was chosen for alignment: the chambers are mounted only with low precision on the millimeter scale, but their movements and deformations are continuously monitored with an optical alignment system [18]. The contribution of the alignment system to the sagitta measurement precision was specified to be better than $30\,\mu m$.

A muon chamber consists of two close-packed multilayers of so called Monitored Drift Tubes (MDT's) with a support structure between them figure 1.8. Depending on the position in the muon spectrometer, a multilayer consists of three or four layers of tubes. The chambers with 2 × 4 layers are located in the inner station, where the background rate is highest, so that the additional 2 layers improve the reliability of the challenging pattern recognition in this region.

A single drift tube is made out of aluminium tubes with a diameter of $3\,cm$ and a $50\,\mu m$ central wire that is connected to High Voltage (HV). The principle of operation is illustrated in figure 1.9.

Whenever a muon crosses the MDT the detector gas is ionised along its track. The
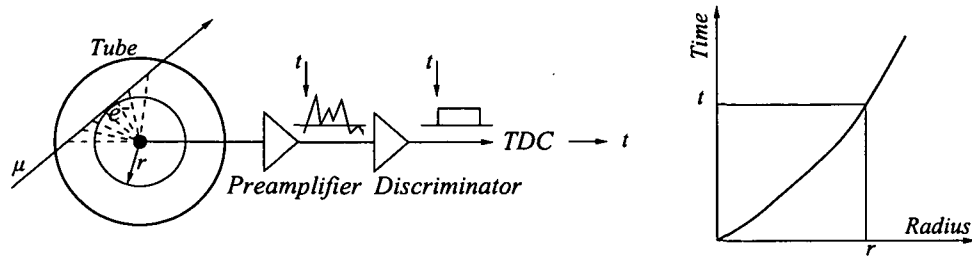
Figure 1.9: Principle of the MDT operation. The drift time of the ionised electrons is measured and converted to radius via a space-drifttime relation (rt-relation)

produced electrons drift towards the wire in the electric field and are multiplied in an avalanche process close to the wire due to the high field. The movement of the ions in turn induces a current signal on the wire which is amplified and converted with a Time to Digital Converter (TDC) to the digitised arrival time of the muon pulse, from which the electron drift time can be determined. By knowing the space-drifttime relation (rt-relation) the radius of the circle, which was tangent to the muon track, can be calculated. Taking into account such drift circle measurements from several MDT's the muon traversed, its track can be unambiguously reconstructed. The rt-relation is obtained by a so called auto-calibration procedure [19] (see also chapter 6).

Chapter 2

Requirements for the ATLAS Muon Chambers

The specifications for the ATLAS Monitored Drift Tube[1] (MDT) chambers derive from the performance requirements of the whole muon spectrometer. The two major performance numbers in this context are the momentum resolution (sec. 2.3) and the muon track reconstruction efficiency (sec. 2.5) which are strongly dependent on the given background environment (sec. 2.2). On the level of the single drift tube operation, these requirements are strongly connected to the spatial single tube resolution (sec. 2.4) as well as to the hit efficiency (sec. 2.5.1) and the 3σ-efficiency (sec. 2.5.2).

To keep the performance prerequisites over the whole LHC operation time at the expected background radiation, the MDT chambers have to fulfill the specified ageing requirements (sec. 2.6).

The first section gives a short introduction to the operation principle of drift tubes, the basic units of MDT chambers, and briefly explains important terms in this regards.

2.1 Working Principle of Drift Tubes

Drift tubes are ionisation detectors operated in proportional mode. The principle of their construction is simple: A thin wire is fastened in the center of a metal tube. The tube is filled with a suitable detector gas and the anode wire is kept on positive high voltage.

The importance of drift tubes for high energy physics stems from their capability of localising particle trajectories to a fraction of a millimeter. The principle of how the distance r_{min} of the particle track to the anode wire can be determined is described in the following. If not stated otherwise the operation with the nominal parameters of the MDT's, as summarised in table 2.1, is assumed.

---

[1]Tubes have been the choice of the detector volume as they have to stand a pressure of $3\,bar$. This is to reach a spatial resolution better than $80\,\mu m$.

drift gas	Ar-CO_2 (93:7)
gas pressure p	$3\,bar$
gas gain G	2×10^4
anode wire radius a	$25\,\mu m$
inner tube radius b	$16.4\,mm$
high voltage V_0	$3080\,V$
worst case background count rate	$1500\,Hz/cm$
worst case accumulated charge	$0.6\,C/cm$

Table 2.1: Nominal operating conditions for the MDT's [16]

2.1.1 Ionisation along the Particle Track
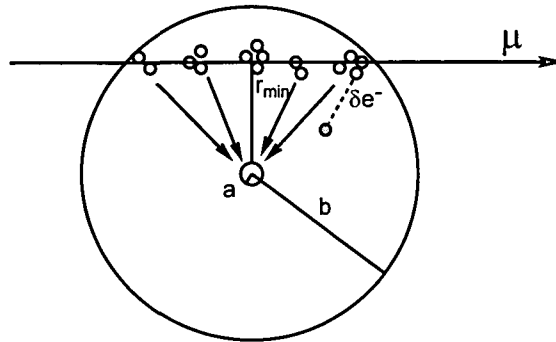
Figure 2.1: Ionisation of the gas along a particle track crossing the drift tube. The created primary electrons can cause further ionisation in their surrounding, known as clusters.

Whenever a charged particle, like a muon, crosses the tube filled with drift gas, the gas atoms along the track get ionised or excited. The mean energy for creating an ion-electron pair does not depend very strongly on the particle type or its incident energy and is about $26\,eV$ for Argon. The primary electrons can have sufficient energy to cause further gas ionisation themselves. Normally the range for this process is quite small so that they are spatial located with their secondary electrons, forming together a so called **cluster** (see figure 2.1). As the primary interactions of the traversing particle are independent of each other, the number of clusters per unit track length is Poisson distributed resulting in an exponential distribution of the distances between the interaction lengths. For an Ar-based gas at $3\,bar$ gas pressure about 100 clusters per cm are created (for $100\,GeV$ muons), with each cluster containing in average three electron-ion pairs.

The mean energy deposit[2] of a charged particle traversing a gas volume of a certain thickness Δx is dependent on the particle's energy and described by the Bethe Bloch

---

[2]the mean energy deposit of a $100\,Gev$ muon in a MDT is $\approx 14\,keV$ [16]

equation (figure 2.2). Fluctuations around this mean energy loss per track length in the gas are characterised with the Landau distribution (for details see section 5.3).
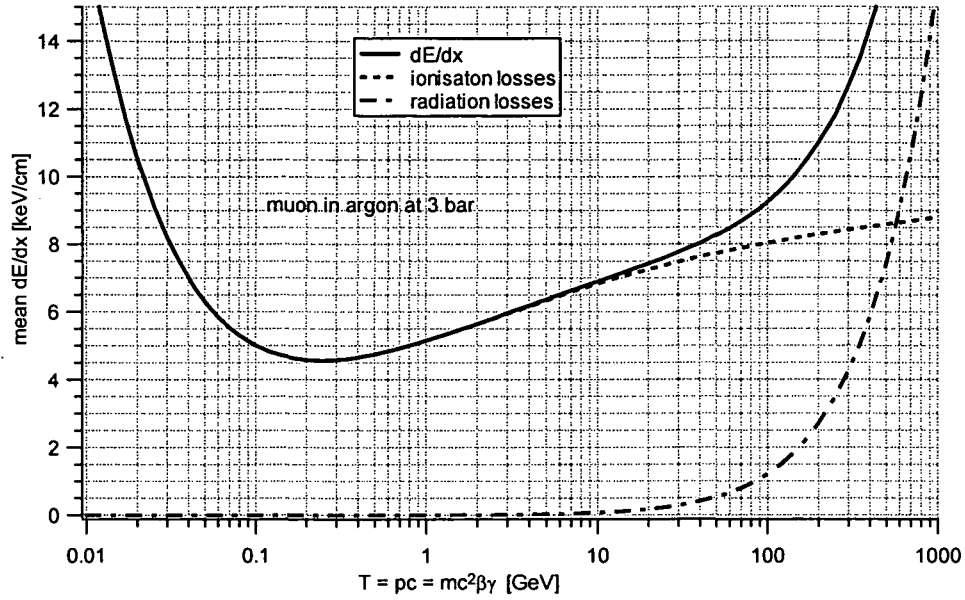
Figure 2.2: Average energy loss per path length of a muon with the kinetic energy T in argon at a pressure of $3\,bar$. The ionisation and radiation contributions to the overall energy loss are plotted separately with dashed lines [1].

The small fraction of primary electrons in the high energetic tail of the Landau distribution, called δ-**electrons** or δ-**rays**, have enough energy to create themselves ionisation tracks up to a length of several mm and can therefore can spoil the drift time measurement (see figure 2.1).

2.1.2 Electron Drift

The created electron-ion pairs along the particle track are separated by the radial electrical field

$$E(r) = \frac{V_0}{r \, ln\frac{b}{a}} \tag{2.1}$$

caused by the high voltage[3] V_0 of the anode wire (radius a) with regard to the tube wall (radius b). The electrons are drifting opposite to the field direction towards the anode, respectively on helical tracks in the presence of a magnetic field, as in the case of the muon spectrometer, where the magnetic field $\vec{B}$ is orientated parallel to the wire direction. In this configuration the drift electrons get deflected by the **Lorentz Angle**

$$\alpha = arctan\left(v_{drift}\,\frac{B}{E}\right) \tag{2.2}$$

---

[3]the corresponding values are give in table 2.1

from the radial direction. The drift velocity v_{drift} of the electrons is the macroscopic mean of two alternating processes: They get accelerated due to the electrical field and loose kinetic energy in collisions with gas atoms. Because of the gas specific scattering cross sections for such collisions the drift velocity dependence on the electric field is different for each detector gas. The collisions with the gas atoms are not only affecting the drift velocity, but also cause spatial diffusion of the clusters, which increases with drift distance. The diffusion processes along and transversal to the drift direction are independent from each other. The longitudinal diffusion is more relevant for the spatial resolution of the drift tube and is quantified by the **longitudinal diffusion** coefficient.

2.1.3 Avalanche Process

As the drifting electrons approach the wire, they gain enough energy to ionise the gas and an avalanche process starts[4]. With the First Townsend coefficient α which describes the increase in the number of free electrons dn over a path length dr

$$dn = n\,\alpha(r)\,dr \tag{2.3}$$

the gas amplification G in principle can be calculated with

$$G = \frac{n}{n_0} = exp\left[\int_a^{r_{min}} \alpha(r)\,dr\right] \tag{2.4}$$

Since the Townsend coefficient depends strongly on the gas mixture and the electric field and due to the multiplying manner of the avalanche process, such gas gain calculations are difficult, as already small uncertainties in $\alpha(r)$ are leading to large errors.

Another important mechanism for operating drift detectors is the **quenching** behaviour of the detector gas: In the avalanche process next to the wire surface also UV photons are generated. If such photons reach the conducting cathode, free electrons can be created by the photo-electric effect. These electrons will as well drift towards the wire, multiply and induce small signals, which are called **afterpulses**. Hence these signals are expected to be separated in time from the first avalanche by at least the maximum drift time. Organic molecules, with their many degrees of freedom, have large photo-absorption coefficients over a range of wavelengths that is wider than that for noble gases. Thus they are used as quencher gases. Common quencher gases are methane and other hydrocarbons, but also inorganic molecules like CO_2.

2.1.4 Induced Signal

The current which is induced from a moving charge q to the anode wire is given by Ramo's theorem [20]

$$i(t) = -\frac{q}{V_0}\,v(t)\,E(r(t)) \tag{2.5}$$

---

[4]at a distance of about 3 times the anode radius

where $v(t)$ is the velocity of the charge and $r(t)$ its radial distance to the wire. Applied to the electrons and ions produced by the avalanche process, this induction is caused by the electrons as well as by the ions, which are starting to move to the anode respectively to the cathode. As the electrons are absorbed already within $\approx 100\,ps$ by the anode wire, the main contribution to the signal comes from the ions drifting to the cathode.

If not stated otherwise, nominal MDT operation conditions are assumed: Ar-CO_2 (93:7), at a gas gain of 2×10^4, at $3\,bar$ and a high voltage of $3080\,V$.

2.2 Background Rates

The high background particle flux in the muon spectrometer results from a chain of complex interactions of primary collision products with the material of the spectrometer. The knowledge of this radiation background has a major impact on the design considerations of the whole spectrometer and define working parameters, like rate capabilities and ageing properties, to optimise the single tube performance.

The radiation background in the muon spectrometer is dominated by low energetic neutrons, photons, electrons, muons and hadrons originating from primary hadrons, which interacted with the forward calorimeters, shielding material, the beam pipe and other machine elements. Most of the charged particles are absorbed in electromagnetic shower processes, during their way through the spectrometer material. Mostly neutrons and associated photons, mainly produced by nuclear capturing of thermal neutrons via (n, γ) reactions, with typical γ energies from $100\,keV$ to several MeV, are remaining. They build a neutron/photon "gas" flowing through the ATLAS cavern in all directions with no time correlation to the primary pp-collisions.
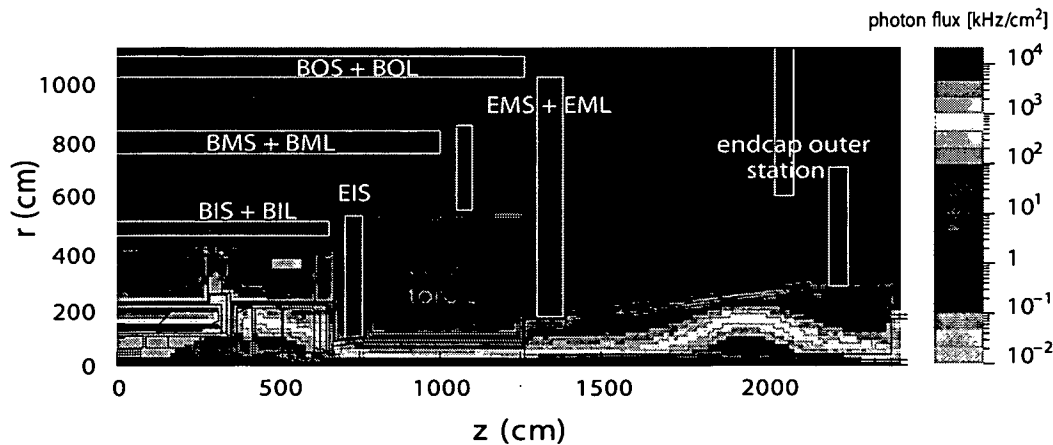
Figure 2.3: Simulated photon flux in the ATLAS cavern at a luminosity of $10^{34}\,s^{-1}cm^{-2}$ [16]. To get actual detector count rates (without safety factor) the numbers must be multiplied with the γ sensitivity of the detector ($\approx 10^{-2}$ for MDT's)

The neutron and photon (figure 2.3) fluxes have been computed [21] with Monte Carlo methods taking into account the material distribution and the magnetic field in the ATLAS detector. In a further step the neutron and photon efficiencies of the used gas detector types have been simulated for the corresponding energy range and validated with measurements. For the MDT's the average γ sensitivity is around 1 %, whereas the neutron sensitivity is one order of magnitude smaller.
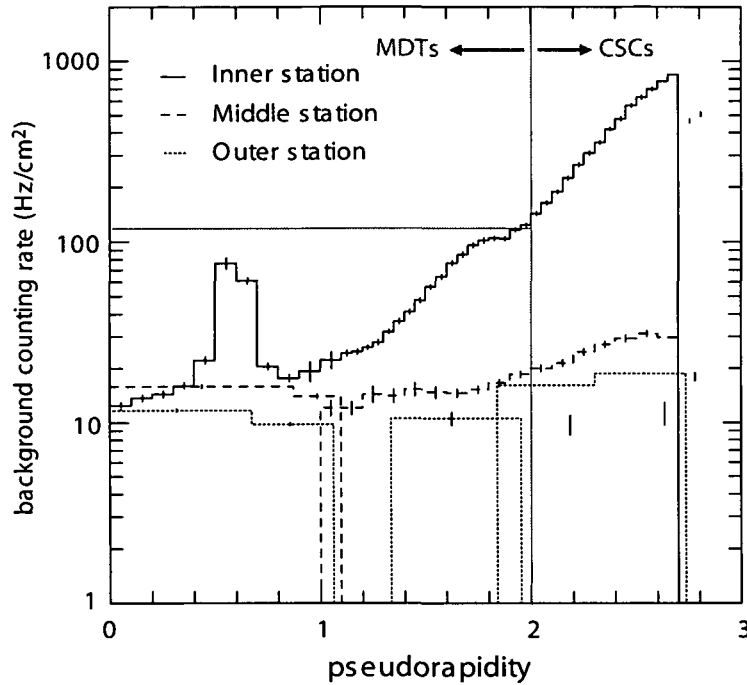
Figure 2.4: Expected total count rate due to uncorrelated background in the ATLAS muon precision chambers [16].

Applying these detector efficiencies for the MDT's to the corresponding neutron and photon fluxes, the expected background count rates affecting the drift tubes can be calculated for the different chamber positions within the spectrometer. As seen in figure 2.4 this rates amount to $100\,Hz/cm^2$ for inner station chambers.

Being aware of the following three uncertainties of the count rate calculations a conservative safety factor of 5 was defined by the ATLAS Muon collaboration, which results in a worst case count rate of $500\,Hz/cm^2$ or $1500\,Hz$ per cm tube length:

- **pp cross section:** Uncertainty factor related to the total pp cross section and to the multiplicity produced in the primary collisions is estimated to 1.3.

- **showering processes:** The limited knowledge of the showering processes in the absorber and of the (n,γ) cross sections is modifying the uncertainty up to a factor 1.2

- **detector sensitivities** The comparison of simulation results and measurements on chamber sensitivities suggests the numbers assumed could be in error by a factor of up to 1.5.

2.3   Momentum Resolution
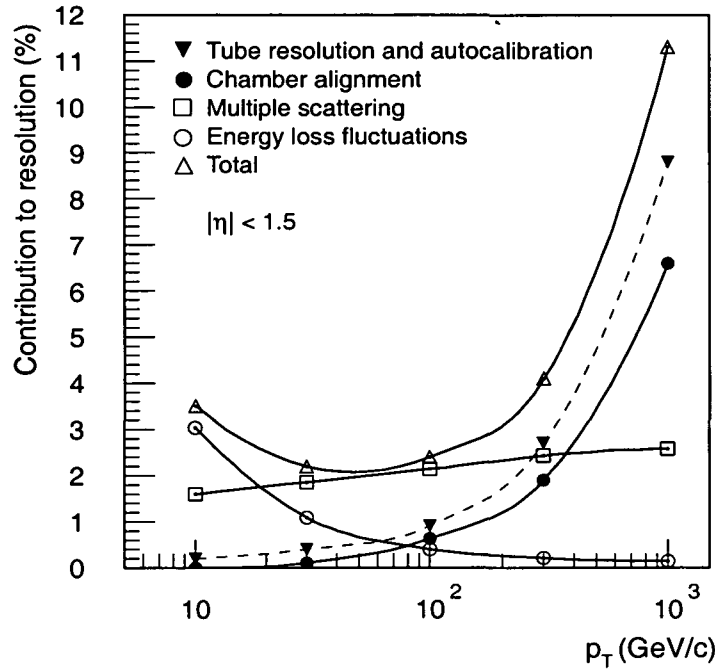
Figure 2.5: Individual contributions to the momentum resolution as a function of p_T. The average single tube resolution is assumed to be $80\,\mu m$ [16].

The most energetic muons expected at LHC have a transverse momentum of about $1\,TeV$. For these muons the physics requirements specify the momentum resolution to about 10 %. The momentum resolution of the spectrometer has been computed for a detailed geometry of all detectors and the distribution of material in the spectrometer [16]. The various contributions to the muon momentum resolution for the barrel region are shown in figure 2.5 as a function of the transverse momentum. One can clearly distinguish three resolution regimes:

- At **high momentum** $(p_T > 300\,GeV/c)$ the resolution is dominated by the precision with which the track deflection is measured. In this region the spectrometer resolution is therefore ruled by the single tube resolution and the chamber alignment. The single tube resolution was assumed to be $80\mu m$ for this simulation and is the topic of the next section.

- At **moderate momentum** $(30 < p_T < 300\,GeV/c)$ the resolution is increasingly limited by multiple scattering in the muon spectrometer for decreasing p_T. The

multiple scattering depends strongly on the amount of material traversed and on the distribution of the material along the track.

- At **low momentum** ($p_T < 30\,GeV/c$) energy loss fluctuations in the calorimeters become dominant. In this momentum range the inner detector, which does not suffer from the calorimeters, provides the more precise momentum measurement.

2.4 Single Tube Resolution

As outlined in the last section the single tube resolution has an major impact on the muon momentum resolution for high energetic muons. A upper limit of $80\,\mu m$ was required as average spatial resolution for a single drift tube in order to meet the momentum resolution requirements in the chosen magnetic field configuration. The average spatial tube resolution $\bar{\sigma}$ is given as the average of the local resolution $\sigma(r)$ over the drift radius r. As for track fitting the measured muon hits are weighted by $1/\sigma(r)^2$, a better figure concerning the resolution of a track fit, is the inverse quadratic average, defined by

$$\bar{\sigma} = \left\langle \frac{1}{\sigma^2} \right\rangle^{-\frac{1}{2}} \quad \text{with} \quad \left\langle \frac{1}{\sigma^2} \right\rangle = \frac{1}{b} \int_0^b \frac{1}{\sigma(r)^2}\, dr. \tag{2.6}$$

The local spatial resolution $\sigma(r)$ is obtained according to the following principle: First the rt-relation $\rho(t)$, for the tube under study, has to be known, e.g. with the autocalibration method (see section ??), before the drift radius $\rho(t_{meas})$ can be computed. The computed radii are then compared to the corresponding "true" drift radii r, which are obtained by a reference system like a silicon tracker, by building the residuals $\delta r_i = r_i - \rho(t_{meas,i})$. With these residuals histograms are filled for discrete slices of the drift radius. The resolution $\sigma(r)$ of such a r-slice is then defined as the Gaussian sigma of the fit applied to the corresponding residual distribution.

When the MDT chamber itself is used to reconstruct the reference tracks, by excluding the tube under study from the track fit, the algorithm becomes more complex, as the extrapolation errors of these track fits have to be taken into account.

A typical measurement of the MDT tube resolution for Ar-CO$_2$ (93:7) and in absence of any background radiation is shown in figure 2.6. The main contributions to the tube resolution are [22]:

- **Charge fluctuations**: the fluctuations of the number of primary electrons cause different signal rise times, which induces a time uncertainty for the discriminator threshold crossing. Therefore low threshold levels are favoured, but limited by the electronic noise level to about $5 \times \sigma_{noise}$ to avoid disturbing noise rates.

- **Cluster position fluctuations**: the position fluctuations of the primary electron clusters are affecting obviously also the resolution, as they introduce a uncertainty arrival time of the drift electrons. Since the time separation of the individual clusters is reduced for long drift distances, this fluctuations affect the resolution only close to the wire.
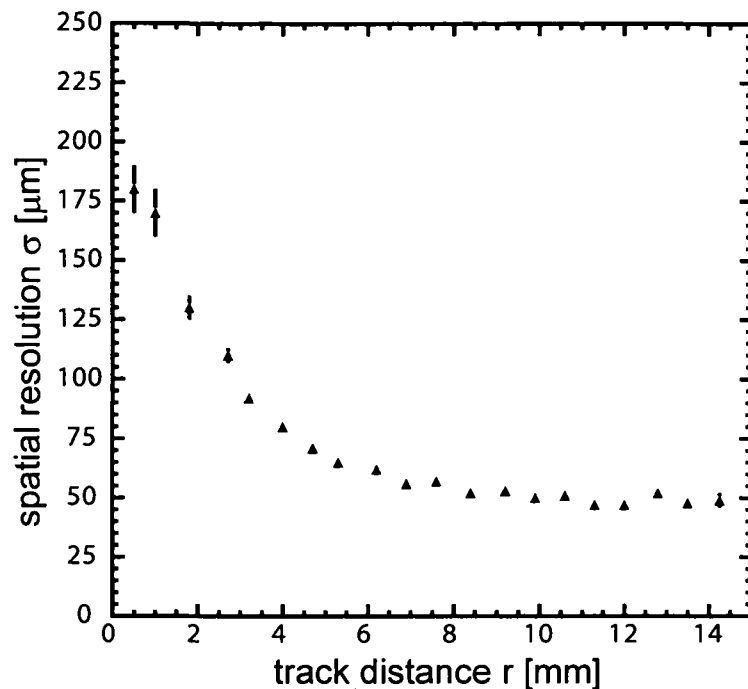
Figure 2.6: Spatial tube resolution as a function of the distance from the wire for Ar-CO$_2$ (93:7)

- **Diffusion** is an intrinsic property of the drift gas (section 2.1.2) and has only a little impact to the tube resolution for Ar-CO$_2$ (93:7).

Whenever exposing the MDT's to a high-rate background environment further effects, which decrease the spatial resolution must be taken into account. This high-rate effects can be divided in two groups [23]:

- **Electronic effects:** Depending on the electronic shaping scheme the baseline of the signal is piling up more or less for a high pulse rate. This **baseline shift** reduces the resolution in the same way as a higher threshold level. A second effect occurs because this baseline shift level is not constant in time, as the background pulses arrive not equally, but exponentially distributed in time. Therefore the **baseline is fluctuating**, which causes an additional jitter on the threshold crossing time. For bipolar shaping the pulses are compensated almost immediately after the signal which suppresses the base line shift. Bipolar shaping reduces both electronic effects to a minimum.

- **Space-charge effects:** At high rates a lot of ions are produced in the avalanche processes near the wire, which are drifting relatively slowly[5] back to the cathode. The space charge of this ion clouds are significantly changing the drift field, which is leading also to a **gas gain drop**. The reduced signals due to this gas gain drop deteriorate the resolution, assuming an unchanged discriminator threshold. On the

---

[5]the maximal ion drift time is 3.8 ms

other hand the **field variations** itself are causing drift time fluctuations as the drift velocity of the non-linear gas is sensitive to the electric field.

2.5   Reconstruction Efficiency

Beside the spectrometer's momentum resolution the reconstruction efficiency is another important performance criterion of the ATLAS muon spectrometer. The reconstruction efficiency is the ratio of correctly identified and reconstructed muon tracks to the whole number of muons traversing the spectrometer. This value is strongly dependent on the occupancy of a single drift tube, i.e. the fraction of time where a single MDT is occupied by an event and therefore can not contribute to the track reconstruction. The high background radiation (section 2.2) is resulting in large occupancies of the detector. Simulations [24] showed that with the applied shaping model (bipolar shaping) of the front end electronics multiple threshold crossings, and therefore multiple hits[6], will occur for a single gamma background signal. The resulting afterhits do not correspond to a real particle (photon or muon) anymore, which would complicate track reconstruction and moreover strongly stress data acquisition. To reduce the number of hits an artificial deadtime t_{dead} was implemented into the front end electronics. For a BIS chamber of the inner station, as used in this work, which suffers from a worst case background rate f_b of $250\,kHz$ [7] the occupancy due to the background yields, for a deadtime[8] t_{dead} of $600\,ns$, therefore up to

$$\mathcal{O}_{back} \approx f_b\, t_{dead} = 15\,\% \tag{2.7}$$

The reconstruction efficiency is moreover strongly influenced by the hit efficiency as well as by the 3σ-efficiency discussed in the following.

2.5.1   Hit Efficiency

The muon hit efficiency ε_{hit} of a drift tube is the probability for detecting a muon which crossed the gas volume. Therefore the hit efficiency is influencing directly the pattern recognition performance and has to be close to one [9] to ensure good pattern recognition even under high background conditions. Besides the overall hit efficiency a local hit efficiency $\varepsilon_{hit}(r)$ can be defined as the ratio between the number of registered hits, whenever a muon is traversing the tube in an radius interval $[r, r + dr]$ from the anode wire, to the total amount of muons which crossed at this interval:

$$\varepsilon_{hit}(r) = \frac{number\ of\ registered\ hits\ for\ \mu's\ at\ [r, r + dr]}{number\ of\ \mu's\ at\ [r, r + dr]} \tag{2.8}$$

---

[6]on average 2.6 hits per photon pulse for Ar-CO_2 (93:7) and a discriminator threshold of 20 primary electrons

[7]taken into account the maximum rate $1.5\,kHz/cm$ from section 2.2 for a BIS tube length of $170\,cm$.

[8]The nominal value was specified to $600\,ns$ at the time of writing, but can be reduced in 6 steps. However it should be close to the maximal drift time ($700\,ns$ for Ar-CO_2 93:7) to avoid frequent double deadtime releases of long signals

[9]normally higher than 99.8 %
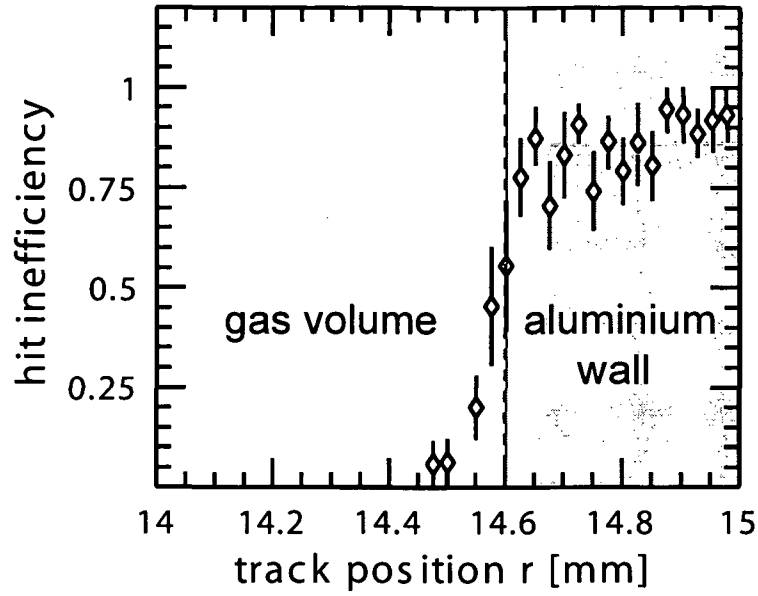
Figure 2.7: Local hit inefficiency $1 - \varepsilon_{hit}(r)$ near the tube wall [25]

To obtain the true crossing radius r either an external tracker is needed, as e.g. a silicon telescope, or the drift time data from the calibrated MDT chamber itself can be used to reconstruct the track. Such studies [25] show significant inefficiencies $1 - \varepsilon_{hit}(r)$ only within $\approx 200\mu m$ of the tube wall, where the track length within the gas becomes too short to produce sufficient primary electrons for generating a signal large enough to achieve a threshold crossing (see figure 2.7). On the other hand hit inefficiencies $1 - \varepsilon_{hit}(r) < 1$ can be observed for muons passing only the $400\,\mu m$ thick aluminum tube without traversing the gas volume at all, which can be understood as delta electrons knocked out of the aluminum into the gas volume, where they in turn induce ionisation as well.

2.5.2 3σ-Efficiency

In contrast to pattern recognition tasks, where the algorithms just need to know if a tube had a hit or not, a good position information of the hits is of major importance for a reliable track reconstruction. This property is quantified by the so called 3σ-efficiency, which is defined as the probability that the trajectory of a muon traversing the tube is measured with an accuracy better than three times the spatial tube resolution $\sigma(r)$:

$$\varepsilon_{3\sigma}(r) = \frac{number \; of \; hits \; reconstructed \; with \; : \; |\rho(t_{meas}) - r| < 3\sigma(r)}{number \; of \; tracks \; through \; the \; tube \; at \; radius \; r} \tag{2.9}$$

where r is again the true drift radius obtained from a reference system and $\rho(t_{meas})$ the radius determined from the drift time measurement via the rt-relation $\rho(t)$. Therefore the MDT's had to be already calibrated before studying the 3σ-efficiency, as well as the tube resolution has to be known.
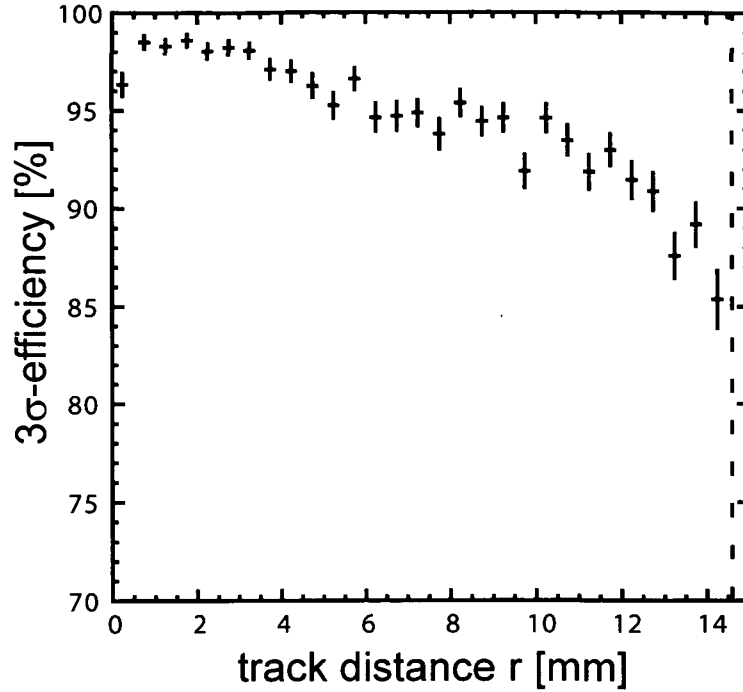
Figure 2.8: 3σ-efficiency for a MDT tube [25]

As visible in figure 2.8 the 3σ-efficiency for MDT tubes is decreasing with the drift distance r already without any background radiation. This can be explained by the increasing probability that a muon hit gets hidden by an earlier δ-electron signal for increasing drift distances.

2.6   Ageing Requirements

The aim for good momentum resolution and high reconstruction efficiency at the given background rates are the driving issues for the MDT operation requirements. One of the biggest concerns is the possible degradation of the drift chamber performance due to the large amounts of charge deposit on the anode wire. During the planned 10 years of high luminosity LHC operation with the worst-case background rate[10] being $f_b = 1500\,Hz/cm$, a maximum charge deposit of

$$Q_{max} = f_b\, T_{LHC}\, I_{prim}\, G \approx 0.6\, C/cm \qquad (2.10)$$

is accumulated per centimeter anode wire, for an average primary ionisation I_{prim} of 1235 electrons per γ-hit [16], when running with the nominal gas gain[11] G of 2×10^4 and assuming an effective operation time T_{LHC} of $10^8\,s$. Such high amount of charge in the

---

[10]already including a safety factor 5 (section 2.2)

[11]was for ageing reasons chosen to be preferable low, but still high enough to meet the resolution requirements

electric field of the tube can produce ageing effects resulting e.g. in chemical deposits on the wire surface as well as on the cathode. These disposals can either reduce the MDT performance, e.g. deteriorate the gas gain, or even kill a tube.

A long-term ageing study of a fully equipped BIS chamber under LHC-like background conditions, in combination with a recirculated gas prototype, was one main subject of this thesis (chapter 5).

2.7   Chamber Construction and Alignment Requirements

The requirements for building MDT chambers have been derived from the performance requirements, as discussed in the previous sections, and are described in detail in [16]. In order to reach the desired measurement accuracy the following main construction requirements have to be fulfilled:

- The gas leak rate for a single tube must be $< 10^{-5}\,mbar\,l/s$.

- The wire tension must be $350 \pm 7\,g$

- The anode wire in a tube has to be positioned to $10\,\mu m$ r.m.s. (in projection) with respect to the outer tube wall.

- The tubes must follow the wires within $100\,\mu m$ to limit the deviations from the ideal rt-relation. Therefore the cross plates of the support structure (see figure 1.8) have to guide the MDT multilayers along the wire trajectories.

- The sag of the wires must be controllable within $10\,\mu m$ up to a wire length of $5\,m$.

- The on-chamber optical alignment system mounted on the support structure must monitor the displacement of the middle cross-plate due to temperature gradients and gravitational sagging at the few micron level.

- The wires of the chamber must be placed with respect to the alignment system with an accuracy of $20\,\mu m$.

- The optical alignment system must measure the relative position of the inner, middle and outer muon station with an accuracy such that the maximum alignment contribution to the sagitta measurement is smaller than $30\,\mu m$.

Chapter 3

The Recirculating Gas Prototype

With an active gas volume of roughly 800 cubic meters (at $3\,bar$) the Precision Chambers of the ATLAS Muon Spectrometer imply the hugest detector gas systems[1] ever built. This large gas volume has to be replaced continuously, otherwise the chamber performance would degrade due to the accumulation of undesirable gas constituents. These contaminations come from chemical reactions following the ionisation processes, from backdiffusion through unavoidable leaks, from outgassing surfaces which are in contact with the gas or from diffusion through the plastic material of the end-plugs and O-rings[2]. Financial constraints forbid to use the gas only once. They require the circulation of the detector gas through the ATLAS MDT system with only a small percentage being replaced each cycle, although the chosen MDT operating gas, Argon:CO_2 in ratio 93:7, consists of relatively inexpensive, inert standard gases. The fresh gas exchange rate has to be chosen as low as possible but large enough to suppress such contamination effects. Furthermore the option of purifying the back-circulated gas must be considered as long as it is economical.

This chapter deals with the design and technical realisation of the first MDT system using gas recirculation. It gives an overview of the experiences gained in operating this prototype continuously for over one year as the gas system for the BIS aging test at CERN discussed in chapter 4 and 5.

A lot of studies have been undertaken in the last decade to find and optimise a drift gas and the working parameters of the MDT's to be compatible with the detector requirements. Before treating the prototype, the first section summarises the considerations which influenced this complex search, leading to the finally chosen gas Ar:CO_2 (93:7) operated at $3\,bar$ and a gas gain of 2×10^4.

---

[1]The gas volume of the Time Projection Chamber (TPC) of the ALEPH experiment was for example $43\,m^3$.

[2]The measured water amount in the order of $100\,ppm$ appearing in MDT chambers, used in tests at GIF and H8, have been understood as mainly due to such a diffusion. With a water permeability of $P_w = 1.9\,\frac{mg.cm}{day.cm^2.bar}$ of the endplug material Noryl, a contribution to the water equilibrium of $\sim 50\,ppm$ can be estimated [26] (for a $2\,m$ long tube supplied with one volume gas exchange per day and an ambient air at $20^o C$ and 60 % humidity)

3.1   Choice of the Drift Gas and Working Point

In this section a brief summary concerning the choice of the gas and the definition of the working point is given. Detailed gas studies based on simulations, test beam results and ageing tests guided the long decision process and can be found in [25] [22] [23] [27] and [28].

The principle object of the ATLAS Muon Spectrometer is to ensure the desired momentum resolution even under the expected background radiation (see section 2.2). To maintain this during the whole LHC era the following criteria are essential for the gas and working point selection:

- **Spatial resolution** better than $80\,\mu m$ for a single tube

- Chamber operated solely in **proportional mode**: streamer rate lower than 1%

- **A low occupancy** to ensure a good pattern-recognition efficiency of the whole Muon Spectrometer even under high background conditions ($\rightarrow$ fast drift gas and low afterpulse rate)

- **No performance degradation** after a collected charge of $0.6\,C$ per cm tube length

- Usage of **non-flammable and non-toxic gas mixtures** due to safety requirements

Taking into account this requirements directly demand considerations on the drift properties, like drift velocity, diffusion and lorentz angle as a function of the reduced field. These functions can be computed with simulations for a selected gas mixture operated at a certain pressure and gas gain. It turns out that some requirements are contradictory, as some considerations will show in the following.

Henceforth the geometry and material of the MDT tubes is assumed to be already fixed according to table 3.1 . Studies which influenced the design of these Parameters can be found in [29], [28] and [30].

tube material	aluminium (ISO AlMn1 4/4 hard temper H18)
tube outer diameter	$29.97\,mm \pm 15\,\mu m$
tube wall thickness	$0.4\,mm \pm 30\,\mu m$
anode wire material	tungsten-rhenium alloy 97 : 3
anode coating	gold-plated 3 % by weight ($\simeq 0.75\,\mu m$ thickness)
anode diameter	$50\,\mu m \pm 0.5\,\mu m$

Table 3.1: geometry and material specifications for the MDT's [31]

3.1.1 Choice of the Carrier Gas

As described in section 2.1 the functionality of a drift chamber is based on a noble gas, responsible for the ionisation process without the danger of building chemical radicals, mixed with quencher gases reducing the afterpulsing behaviour and furthermore giving the chance to have an purposeful impact on the drift properties of the whole mixture.

For a low occupancy of the drift tubes one aims for a fast drift gas with a preferable maximum drift time smaller than $500\,ns$. From the five non-radioactive noble gases only mixtures with neon, argon and krypton reach reasonable fast drift velocities, also in areas away from the anode wire where the reduced electric field E/ρ is rather low. Moreover a high primary ionisation is desired. A higher number of released primary electrons increases the pulseheight of the induced signal of a gas detector when running in proportional mode and reduces the charge fluctuations in the ionisation track. Both improves the spatial resolution. The number of ionisation pairs increase with the atomic number[3], therefore Krypton would be the most convenient choice. Since krypton is out of the question for financial reasons[4], argon is used as carrier gas.

3.1.2 Considerations for the Quencher Gas

Many different compositions of quencher gases added to the carrier gas argon have been proposed and studied as baseline for the MDT chambers [33] [28] [34] [30]. Organic quenchers like methane and ethane have been combined with the non-organic quenchers nitrogen and carbondioxid. Organic gases have better quenching properties as their more complex molecule structure allows more vibration and rotation modes for catching the excitation photons, which otherwise would produce photoelectrons in the cathode wall and therefore afterpulsing. In order to certify gas mixtures with such organic gases as inflammable, they can be used only within a few volume percent. However already a few percent of these gases increase the drift velocity significantly for low E/p [5]. This results in small maximal drift times (around $500\,ns$) since most of the MDT volume is dominated by this low electric field region. With the systematic addition of nitrogen it is moreover possible to get a saturated almost constant drift velocity in this field region of interest. Thus the saturation leads to a rather linear rt-relation, wherefore such gases are called linear (see figure 3.1.2).

Linear gases which have been taken into account as MDT drift gas are for example Ar-C_2H_6-N_2 (90:5:5), Ar-CH_4-N_2-CO_2 (94:3:2:1) and the so called DATCHA-gas[6] Ar-CH_4-N_2 (91:5:4). The enormous advantage of linear gases is that their drift velocity is almost unaffected by small changes in E and the gas density ρ. This makes the rt-relation of such gases rather stable against variations of environment parameters which influences

---

[3]The in average produced ion pairs per cm and bar increase in first approximation with the atomic number like $N_{pair} \simeq 4.5\,Z$ [32]

[4]Krypton is above 100 times more expensive than argon

[5]E/p in the range of ~ 0.1 to $\sim 0.8 \frac{V}{cm\,mbar}$, which is corresponding for $3\,bar$ to the field region ranging from the cathode wall down to a distance of $0.2\,cm$ to the anode wire

[6]Cosmic test setup with a complete barrel station which was installed in the UA1 pit at CERN in 1996/97. DATCHA stands for Demonstration of ATlas CHamber Alignment
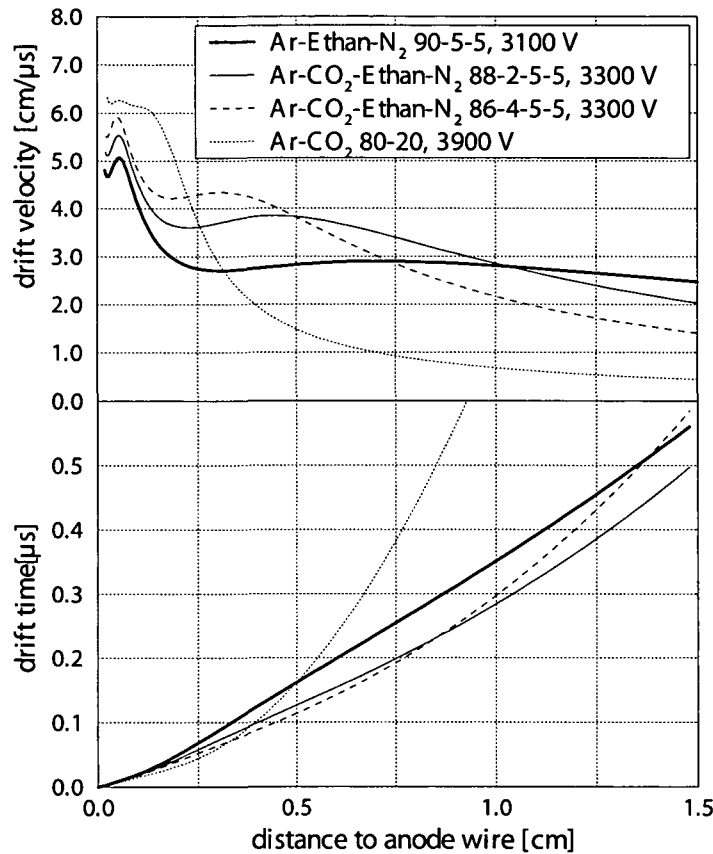
Figure 3.1: The impact of the drift velocity on the rt-relation of a MDT, illustrated on the example of the linear gas Ar-C_2H_6-N_2 (90:5:5), the non-linear gas Ar-CO_2 (80:20) and two semi-linear gases [33]. The shown drift velocity of the linear gas is almost constant over 90 % of the drift distance, although the reduced electric field varies over one order of magnitude in this region.

E and ρ, like temperature, pressure, high voltage, background rate or non-concentricity of the anode wire. A small drawback of such fast gases is a larger Lorentz angle which scales with the drift velocity (see section 2.1.2) leading to longer spiral drift paths and therefore to a higher dependence of the rt-relation from the magnetic field.

Several long-term irradiation tests with MDT tubes, flushed with the above mentioned organic gas mixtures and some derivates, had been undertaken [29] [34] [35] [36]. Some of them showed clear ageing effects already after a fraction of the expected radiation dose during LHC operation. But also for gases where no or small ageing was observed, their usage would have been risky, due to rate-dependent ageing[7] or ageing behaviour which was unpredictable sensitive to the operating conditions, like gas flow, gas mixture

---

[7]Ageing tests can normally not carried out in real time (here 10 years). Therefore they are scaled down in time by increasing the irradiation. Some tests [30] indicated a much smaller impact on ageing under such high-rate test conditions, i.e. predictions to the long-term ATLAS operation would have been difficult

and gas additions.

The ageing problematic with mixtures containing hydrocarbons has been understood as polymerisation processes leading to deposits on the anode wire. Excited molecules may break up, whose fragments are chemical radicals with an electrical dipole moment. In the inhomogeneous field of the drift tube they are attracted from the anode. If such a radical comes up against another radical or ion, they may react, building up long-chain molecules on the anode with time. Insulating deposits are shielding the electrical field and conductive substances are extending the anode wire diameter. Both mechanisms reduce the electrical field and therefore the gas gain of the drift tube.

3.1.3 The Non-Linear Gas Ar-CO_2

To avoid this polymerisation problem suitable gas mixtures without any hydrocarbons were studied. Mixtures with CF_4 replacing the methane showed similar drift properties as their organic equivalent. As the availability of CF_4 due to environment protection restraints has been uncertain and hydrofluoric acid production in the presence of CF_4 and water was observed in other experiments[37], this alternative was rejected. Finally the simple 2-component mixture Ar-CO_2 was a promising candidate. This relatively slow[8] and rather non-linear drift gas has on the other hand a smaller longitudinal diffusion and provides a small Lorentz angle.

The new baseline gas Ar-CO_2 (93:7) has been established in [23]. It has been shown that the resolution averaged over the drift radius, also under background radiation, is even slightly better[9] as for the DATCHA-gas Ar-CH_4-N_2 (91:5:4). Even though field variations due to space charge fluctuations contribute strongly to the high-rate resolution in this non-linear gas, whereas this contribution is negligible in linear gas mixtures. Variations of the r-t-relation due to environmental parameters like the background rate can be huge (more than $0.3\,mm$) in such a non-linear drift gas. However this systematic errors have been understood and quantified, so that corrections to the r-t-relation can be provided once it was found by autocalibration. Therefore the r-t-relation is not constant with time and is in principle different from tube to tube[10]. The mixing ratio 93:7 is the optimisation result of reducing the CO_2 content to increase the drift velocity but only as far as enough quenching gas remains for an acceptable afterpulsing behaviour[11].

As a necessary gas additive water was specified on the level of some $100\,ppm$ to increase the electrical conductivity of the endplugs, which essentially reduces the occurrence of Hv sparks, since charge polarisation on the endplugs is lowered. Therefore the regulation of the water concentration is considered for the ATLAS gas system (see ??).

The agreement to use a quite slow and non-linear drift gas had moreover a big influence on the characteristic and design of the front end electronic [24].

---

[8]$T_{max} \simeq 700\,ns$ for Ar-CO_2 (93:7) at 3 bar and a gas gain of 2×10^4

[9]a inverse quadratic averaged resolution $\bar{\sigma}$ of $87\,\mu m$ compared to $91\,\mu m$ at a background rate of $1400\,Hz/cm$ [23]

[10]for the autocalibration method the r-t-relation has to be assumed as constant within a pattern recognition unit, that means in the smallest case within one MDT-multilayer

[11]less than 3 % at standard conditions

3.1.4   Choice of the Working point

The number of primary electrons increases linear with the pressure. Therefore a certain product of pressure times gas gain, leads to the same amount of charge deposit. In such a way at 1 bar and a gas gain of 6×10^4 the charge deposit for the most radiated chambers reaches the specified $0.6\,C$ (see section 2.6) after 10 years including a safety factor 5. Increasing the pressure by keeping the amount of total charge deposit fixed improves the spatial resolution because the longitudinal diffusion as well as the primary ionisation fluctuations decrease. While an increase from 1 bar to 3 bar is necessary to ensure an average resolution smaller than $80\,\mu m$, going to 5 bar does not improve the resolution much [22] but would complicate the whole design (dimensioning of the components, leak tightness, safety measures).

The gas gain in turn should be high enough to provide an acceptable time resolution of the signal threshold crossing but on the other hand is limited to avoid ageing and to keep the streamer rate low. Moreover is the resolution deteriorating with higher gas gain in a high background environment. The increasing drift field fluctuations due to space charge effects dominate the spatial resolution in this case [23].

3.1.5   Influence of Gas Additives and Gas Mixture on the Drift Properties

Systematic studies of the MDT drift properties with respect to variations of gas temperature, gas mixture (percentage of Ar and CO_2) and water content have been carried out in the 2002 testbeam [38] with data collected from a setup with six MDT chambers. The gas mixture ratio of Ar-CO_2 was varied from 91:9 to 95:5, the amount of water vapour was kept on three different levels $(0, 520\,ppm$ and $2700\,ppm)$ and the temperature ranged from 17° to 23°. Applying these variations, the maximum drift time t_{tot} was followed up by performing fits to the drift time spectra similar to the method described in section 6.2. The results of this studies is summarised in table 3.2. The sensitivity to the variations expressed in the change of drift time per unit of variation is indicated as well as the maximal allowed variation corresponding to a change of $2\,ns$ of t_{tot}, that in turn corresponds to a systematic of about $20\,\mu m$ on the position determination.

varied parameter	slope	maximal variation
temperature	$-2.67 \pm 0.10\,ns/K$	$0.7\,K$
Ar percentage	$-69.6 \pm 0.7\,ns/\%$	3×10^{-4}
H_2O content	$5.50 \pm 0.05\,ns/100ppm$	$40\,ppm$

Table 3.2: Influence of temperature, argon percentage and water amount to the maximum drift time t_{tot} [38]

3.2 Design of the Recirculating Gas Prototype

In the past only gas systems running in a simple single pass mode had been introduced to supply any kind of MDT test setups with the drift gas. As mentioned above using the gas only once is impossible for financial reasons. A gas volume of $\sim 800\,m^3$ has to be recirculated once a day, leading to a total gas flow of about $100\,Nm^3/h$.

To study the required gas circulation the prototype described here was developed and build. Although the whole setup acted as one system the motivation for constructing the MDT circulation prototype can be divided into two major parts:

- **System Test:** The behaviour of this rather complex gas system with the gas circulator as core component had to be tested and understood. Experiences in operating the gas circulation had to be gained to prove the feasibility of the recirculating MDT gas system concept and to get a more detailed overview of what is needed for the final system. The prototype system test is the topic of this chapter.

- **Ageing Test:** The influence of gas circulation to the ageing behaviour of the drift chambers had to be observed. Therefore a MDT chamber was connected to the gas prototype, with one multilayer connected to gas circulation and the other one to a standard flushed gas system, and operated in a long-term test under high gamma radiation. The ageing test is documented in the next two chapters.

The design of the prototype was guided by the aim to simulate the final ATLAS gas system. The general requirements are summarised in table 3.3. One significant difference between prototype and final system is the amount of gas volume to handle. Whereas the ATLAS Muon detector consists of almost 1200 chambers, for the ageing test only a single multilayer of the MDT chamber was used as active detector volume which corresponds to a $\frac{1}{5000}$ of the total ATLAS volume.

The mode of operation is explained in the following by means of the gas flow diagram shown in figure 3.2. Type and model specifications of the corresponding gas components can be found in table 3.4.

The overall circulation flow of $100\,Nm^3/h$ [13] had to be driven also in the prototype because the final Atlas gas circulator was implemented which needs a minimum gas flow to maintain the gas bearings (see section 3.3). As a consequence the circulation system consists of two different closed loops, both driven by the same pressure difference created by the turbine:

- The so called **"Big loop"** takes over the part of the "missing" 1193 chambers as seen by the turbine. The resistance to the gas flow is emulated by a single manual valve.

---

[12]sustainable water concentrations are limited to a maximum of $1000\,ppm$ in order to exclude corrosion of the compressor blades

[13]Nm^3 stands for normal cubic meter, which is the gas volume a certain amount of gas under pressure would expand to at standard conditions ($1013.25\,mbar$, $0\,^{\circ}C$) and is therefore a temperature and pressure independent unit for gas quantities.

total volume:	$754\,m^3$ (at $3\,bar$)
number of chambers	682 (barrel) + 512 (end cap)
number of gas channels	112 (barrel) + 162 (end cap)
operating pressure	$3.0\,bar\,abs.$
gas composition	Ar (93 ± 0.25 %)
	CO_2 (7 ± 0.25 %)
gas circulation	1 $volume/day$
→ circulating flow	$\sim 100\,Nm^3/h$
refreshing rate	10 % $of\,total\,volume/day$
→ fresh flow	$\sim 10\,Nm^3/h$
leakrate	< 10 % of overall MDT leakrate (10 % of $27Nm^3/h$)
base line impurities	$\leq 100\,ppm\,O_2$
water content[12]	$\sim 500\,ppm$
cleanliness of components	oil- and lubricant free, no silicon
	(for detailed material specifications see [39])

Table 3.3: Atlas MDT gas system specification [39]

- The "**Small loop**" maintains the daily volume exchange of the circulated MDT multilayer. Therefore just a tiny part of the total flow from the "big loop" has to be extracted.

The gas system consists of two independent subsystems. One supplies the circulated multilayer of the chamber and contains the two loops quoted above and the other one runs the second multilayer in classical flushing mode. The reason for applying different modes to the two halves of the chamber is to be able to distinguish if possibly emerging ageing effects are related to gas circulation or result from other phenomenons.

The gas supply of both subsystems is provided in common as premixed Ar-CO_2 (93:7) mixture in batteries[14] of 90 Nm^3, which are large enough to last for a typical operation period of three months[15].

3.2.1 Flushed Multilayer

To sustain the flushing mode for the second multilayer only two active regulation components are needed. Whereas the mass flow controller (1)[16] controls the gas flow through the multilayer, the back pressure regulator (3) keeps the drift tubes at the required absolute pressure of 3 bar. For a volume exchange rate of once per day the mass flow controller is adjusted to $\sim 20\,Nl/h$, an additional rotameter (2) can be used in parallel to increase the gas flow, especially during filling and purging. The pressure regulation

---

[14]Carbagas, class I gas mixture with Ar in purity 46 (means Ar > 99.996 %, O_2 content < $5\,ppm$ and H_2O < $10\,ppm$) and CO_2 in purity 40 (CO_2 > 99.990 %, O_2 content < $20\,ppm$ and H_2O < $30\,ppm$)

[15]for an exchange rate of 2 volumes per day like the system was operated in the ageing period 2 (see section 4.2

[16]the labels correspond to the gas flow diagram in figure 3.2
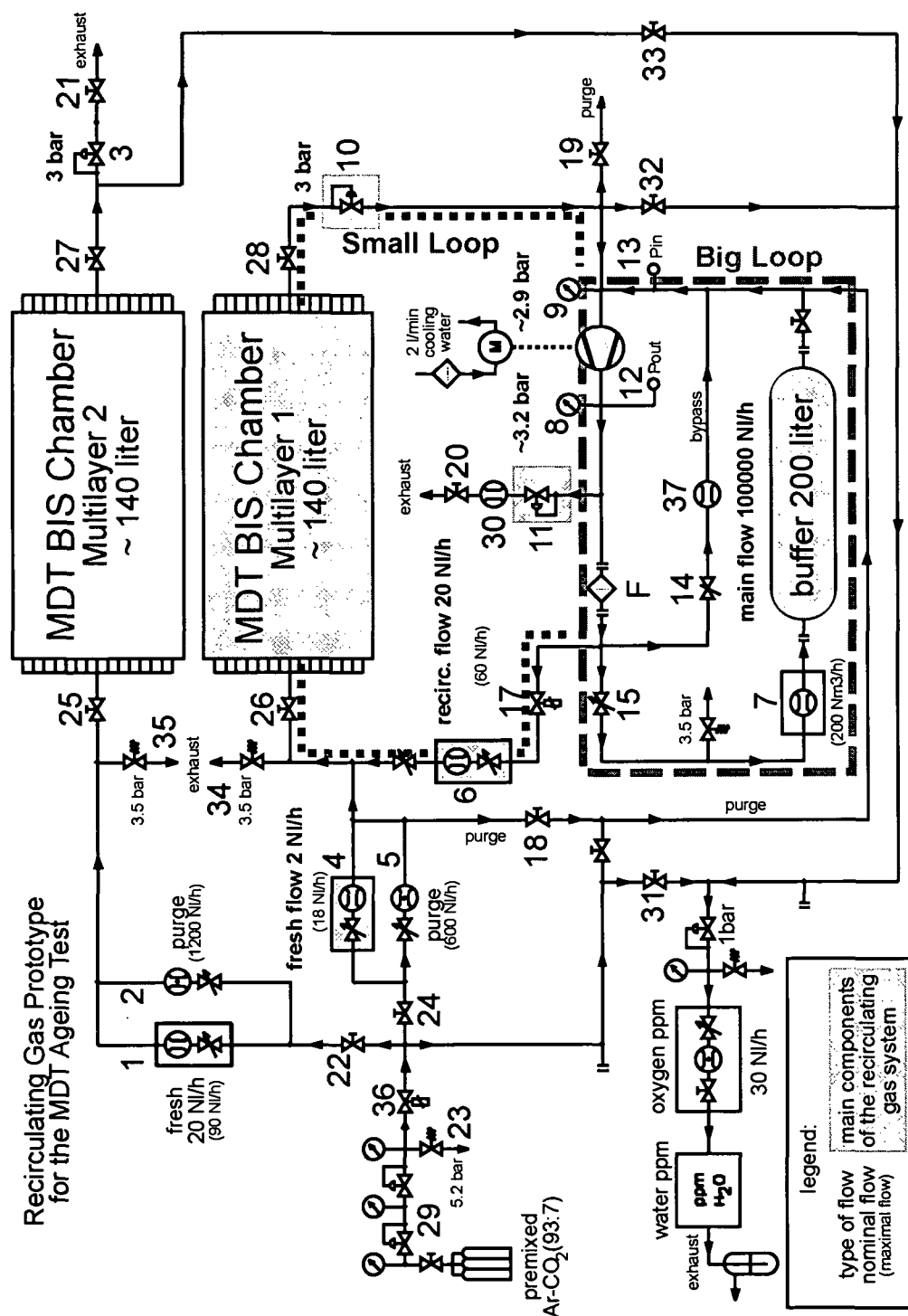
Figure 3.2: Gas flow schematic of the MDT gas prototype used for the BIS ageing test at the Gamma Irradiation Facility. The "Big Loop" is marked with a dashed and the "Small Loop" with a dotted line. Crucial components of the circulating part of the system are highlighted.

pos.	component	manufacturer	type
1	mass flow controller	Bronkhorst, Ruurlo, NL	F-201C-RA-33-E
2	rotameter	Voegtlin Instruments, Aesch, CH	V100-140.14, lubricant free
3	pressure controller	Bronkhorst, Ruurlo, NL	P-702C-RA-33V
4	mass flow controller	Bronkhorst, Ruurlo, NL	F-201C-FA-22V
5	mass flow controller	Bronkhorst, Ruurlo, NL	F-201C-FA-22V
6	low Δp-mass flow controller	Bronkhorst, Ruurlo, NL	F-111C-FAC-33-V
7	low Δp-flow meter	Systec Controls, Puchheim , D	Deltaflow DF10MG-F-DW-ME-PN16
8,9	pressure gauge		
10,11	pressure controller	MKS Instruments, Andover, US	Baratron 690 A + 0248A-02000RV
12,13	absolute pressure sensor	Bourdon-Haenni, Jegenstorf, CH	ZE 0525
14	ball valve	recuperated from ALEPH TPC	
15	ball valve	recuperated from ALEPH TPC	
17	pneumatic shut-off valve	Parker	
18	manual shut-off valve	Parker	Nova B 441T
19-21	manual shut-off valve	from CERN-store	stainless steel
22	manual shut-off valve	Parker	Nova B 441T
23	pressure relief valve	Parker	M6A-RL4A-VT-SS
24-28	manual shut-off valve	Parker	Nova B 441T
29	pressure reducer		
30	mass flow meter	Bronkhorst, Ruurlo, NL	F-201C-FA-22V
31-33	manual shut-off valve	Parker	Nova B 441T
34,35	pressure relief valve	Parker	M6A-RL4A-VT-SS
36	pneumatic shut-off valve	Parker	
37	flow meter	Brooks Instrument, Hatfield, US	5813
F	dust filter	Ultrafilter International, Haan, D	SM 15/3, 5 micron, Viton

Table 3.4: component list of the prototype gas system. Position numbers correspond to figure 3.2

has been found stable to $1\,mbar$ with the absolute pressure calibration being accurate to about $\pm 10\,mbar$.

The analysis branch connection for the second multilayer had to be installed upstream of the pressure controller (3), because if connected downstream, all the gas would flow to the exhaust due to lower resistance. However this circumstance affects the pressure regulation for a few seconds after opening the valve (33).

To protect the chamber from overpressure[17] the self-releasing overpressure valves (35) as well as (34) open to ambient air when in any event of fault the pressure reaches $3.5\,bar$. Anyhow this should be avoided since a once opened safety valve may not be tight anymore.

3.2.2 Circulated Multilayer

"Big Loop"

As mentioned above, the circulating part consists of two gas loops. At the beginning only the so called "big loop" was set up to gain experiences with operating the ATEKO turbine. In this circuit the flow regime is highly turbulent (see section 3.5.2) although pipes with an inner diameter of $49\,mm$ are used, not surprisingly since $100\,Nm^3/h$ at $3\,bar$ means here an average flow velocity of $5\,m/s$.

The turbine generates a pressure difference from typically $300\,mbar$ dependent on the rotation speed and certainly on the overall flow resistance of the "big loop". Inlet and outlet pressure are measured by the sensors (13) and (12). The gas leaving the turbine first passes a particle filter (F) made up of fine steel mesh to retain dust larger than $5\,\mu m$. This feature was recommended by the turbine manufacturer since the creation of small quantities of graphite dust rubbing off from the gas bearings during starting and stopping the machine can not be excluded. The pressure loss due to the filter is about $50\,mbar$. The next component on the high pressure side, normally operated at $\sim 3.2\,bar$, is the large manual ball valve (15). Here the main pressure drop occurs and therefore this valve simulates effectively the flow resistance of the whole ATLAS gas system and allows to adjust the main flow of the "big loop" to the turbine working range.

The following flowmeter (7) monitors the main flow and creates a relatively small pressure loss of about $5\,mbar$ thanks to the applied measuring principle: The differential pressure in the flow direction and counter the flow direction of an obstacle (round profile probe) is measured, which is in first approximation proportional to the square of the flow. The device was calibrated with air and programmed with the conversion parameters for Ar-CO_2 (93:7) at $60\,^{\circ}C$ and $3\,bar$ from the manufacturer. Using the ideal gas equation, the measured value is corrected from the slow control for temperature and pressure. Taking into account the precision of the temperature (PT-100 sensor) and pressure measurement (13) the accuracy of the flow measurement is better than $4\,\%$ for flows larger than $70\,Nm^3/h$.

Since the 200 liters cylindrical container dominates the volume on the low pressure side

---

[17]MDT chambers are individually tested for $4.5\,bar$ [40]

of the "big loop" the pressure decreases to around $2.9\,bar$ in the case of a circulation shutdown. The size of this certified pressure vessel was chosen large enough to provide a gas reservoir for a vibration-free operation of the turbine's gas bearings and on the other hand small enough to avoid a too strong dilution of any radiation-related ageing effects as this gas volume is not exposed to irradiation.

To assist the compressor with lower resistance during running up a bypass loop consisting of a manual valve (14) and a thermal mass flowmeter (37) was foreseen. During the turbine tests it was discovered that a fixed bypass flow of $\sim 6\,Nm^3/h$ is sufficient as protection in this concern.

Finally it should be noted that the pressure drop in the ~ 10 meters of pipes[18] of the "big loop" can be neglected, as pressure losses smaller than $0.3\,mbar$ per meter can be assumed.

"Small Loop"

The flow needed for the "small loop" supplying the multilayer 1 branches off the high-pressure side right behind the particle filter. A pneumatic shut off valve (17) opens whenever the turbine is running and thus prevents the chamber from loosing pressure to the "big loop" in case of a circulation failure. For the mass flow controller (6), responsible for regulating the circulating flow[19], a special low-pressure version had to be purchased since standard mass flow controllers need far larger pressure drops in the order of $100\,mbar$. Adjusting of the fresh gas[20] intake is done with a standard mass flow controller (4), whereas a second branch in parallel allows again faster filling or purging of the system.

Similar to the flushed multilayer also the circulated one is pressure driven, meaning that the exiting gas flow is regulated in such a way that the pressure in front of the pressure regulator (10) is kept at a constant value. But the main difficulty here lies in the fact that the gas flow passing the back pressure regulator (10) at the exit of the chamber has to be split. One fraction corresponding to the fresh gas intake rate minus any possible leak rate must be extracted from the system to exhaust while the rest is re-compressed and recycled. The somewhat naive concept to control the flow sent to exhaust also by a flow controller is difficult to implement since it requires that the relation

$$\dot{Q}_{out} = \dot{Q}_{in} - \dot{Q}_{leak} \qquad (3.1)$$

is exactly met. This can not be realised by fixed setpoints on the flow rates but would necessitate some kind of feed back loop. For the prototype system a different approach was chosen, were the gas flow released from the system to exhaust is also pressure driven. The technical implementation is via the back pressure controller (11), set to approximately $3.2\,bar$, which was moved to the shown position on the high pressure side of the compressor after first experimenting with a location directly in the return line from

---

[18] 6.8 meters of flexible stainless steel bellow pipes with NW 50 flanges according to Iso and $\sim 3.2\,m$ rigid stainless steel pipes with Iso-K-flanges plus eleven 90° bends

[19] set to $18\,Nl/h$ for a desired exchange of 1 volume/day

[20] with a baseline flow of $2\,Nl/h$ for a refreshing rate of 1 volume in 10 days
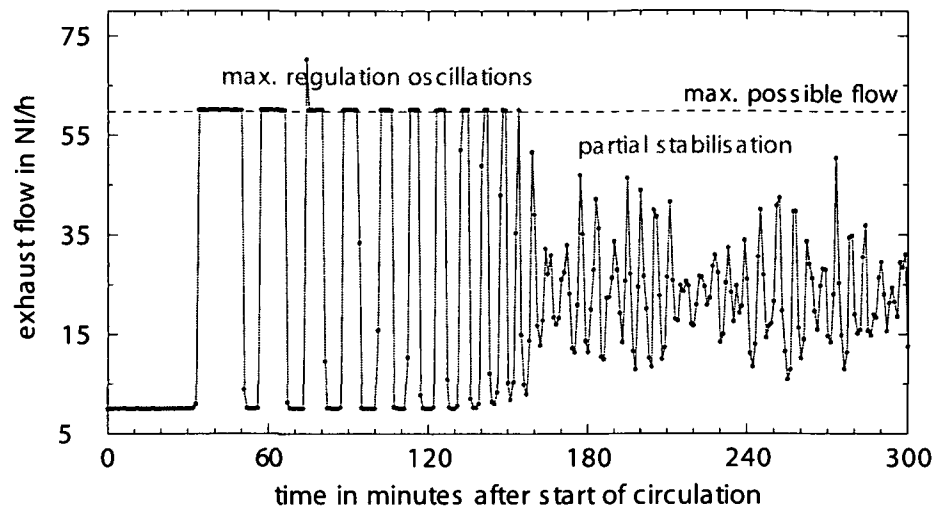
Figure 3.3: Monitored exhaust gas flow during 5 hours after the circulation was stopped for several hours and restarted. The fresh gas intake rate is $2\,Nl/h$.

the chamber which caused the pressure controller (10) to oscillate. Figure 3.3 shows the measured exhaust flow, monitored by the mass flow controller (30), with time. One clearly sees that the flow rate is too small for the used pressure regulator which causes alternating closed and open states of the control valve. The system can nevertheless be operated since the resulting small pressure fluctuations in the big loop proved to be varying slowly enough to be irrelevant.

In a similar problematic to the operation of the mass flow controller (6) also the pressure controller (10), regulating the chamber pressure has to work with a quite low pressure drop of a few $100\,mbar$ maximum across the device.

Circulated Mulitlayer in Flushing Mode

The normally circulated multilayer can also be operated in single pass mode without any need of hardware change on the setup. After stopping the circulation one just has to lower the setpoint of the pressure controller located at the exhaust line (11) from typically $3.2\,bar$ to around $2.8\,bar$ to get enough pressure drop for operating the pressure regulator (10) properly. In this condition the fresh gas intake has to be increased typically by a factor 10 to compensate for the missing circulating flow.

The multilayer 1 was running in this mode for example during the whole testbeam operation in June 2002, in which high rate studies have been of major interest. To get cleaner electrical noise conditions, the circulation was stopped to avoid known problems with induced noise created by the ATEKO turbine (For steps to fight this noise see section 3.5.6).

3.2.3 Gas Analysis Devices

The main impurities in drift gases are oxygen together with nitrogen emerging in the composition of air as well as water vapour. They originate mainly from the ambient air diffusing via small leaks into the gas system or via diffusion through tube plugs and seals. To monitor and analyze these constituents, a special analysis line was installed, which allows to measure the oxygen and water content for gas coming from either one of the two chamber multilayers or directly from the premix supply (valves 31, 32, 33).

For obtaining the water concentration, two different devices based on two different measuring techniques have been employed in the course of the whole test. One instrument[21] is directly measuring the dew point temperature[22] by cooling down a mirror in the gas flow until water condensates on its surface. This consequently is detected by the change in reflectivity of a light ray. Since the water amount R_{water}, normally given in ppm_v[23], is for ideal gases equal to the ratio between the partial pressure of the water vapour p_{vap} and the total pressure p_{tot} at a given temperature T, the situation at the measured dew-point T_{dew}, where p_{vap} by definition pass into the saturated vapour pressure $p_{sat.vap}$ can be used to get the water amount, as the relation between $p_{sat.vap}$ and T_{dew} is well-known and quantified in literature:

$$R_{water} = \frac{p_{vap}(T)}{p_{tot}(T)} = \frac{p_{sat.vap}(T_{dew})}{p_{tot}(T_{dew})} \tag{3.2}$$

The measurement principle of the so called moisture meter[24] on the other hand relies on an impedance measurement of a capacitor. Humidity deposited in this sensor changes the dielectric constant of the capacitor and therefore increases the measured capacity.

Oxygen is monitored using an instrument called Teledyne[25] equipped with an electrolytic cell[26] which induces a current according to electro-chemical processes.

It turned out that a minimum flow around $30\,Nl/h$ was required for a sensitive water measurement. Therefore the analysis flow was increased manually during a measurement. This measurement had to be kept short to keep the chamber pressure unaffected especially for the circulated multilayer. As a continuous drift time increase in the circulated multilayer was observed during the first 2 months of the ageing test (section 5.7) and this phenomena was suspected to be water content related, a online water measurement was required. Therefore the DewPrime dewpoint-meter was installed directly into the circulated flow coming from the chamber, in front of the pressure controller (10) to run the dewpoint measurement at a defined pressure. Consequently the water concentration was obtained from equation 3.2 with a pressure p_{tot} of $3\,bar$.

---

[21]DewPrime 2000 Series, EdgeTech, Milford, US
[22]Temperature at which water can exist in equilibrium in both vaporised and liquid phase.
[23]parts per million by volume
[24]model SDA, Show Moisture Meters, Westgate, UK
[25]Teledyne Analytical Instruments, model 316A-2X, Los Angeles, US
[26]Teledyne Micro-Fuel-Cell A-2C, this type is suitable for gas mixtures with CO_2

3.3 The ATC Gas Turbine

3.3.1 Choice of the Gas Circulator

The gas system for the ATLAS Muon Spectrometer is the hugest system ever developed for a particle physics detector. As a consequence the specifications for the gas compressor, derived from the overall MDT gas system specifications (table 3.3), are quite unusual:

- The compressor has to deal with a **gas mixture density**[27] of 4.95 kg/m^3.

- One volume exchange per day corresponds to a **nominal flow rate** of 100 Nm^3/h.

- This should be increasable to a **maximum flow rate** of 200 Nm^3/h,

- but also **adaptable to lower flow rates** whenever sub-distribution systems have to be stopped.

- To sustain the required flow through the total given gas resistance, built up by the components in the circuit, like the piping, the flow adjustment valves, the flowmeters, the chambers itself, the pressure controllers and the optional purification system a **minimum pressure difference** of 0.3 bar must be ensured by the compressor.

- **High reliability** of the machine is needed as the gas system has to operate during 8 months a year with nearly no interruption. Therefore concepts with **almost no maintenance** are favoured.

- **Strict purity requirements** have to be fulfilled to keep the performance of the MDT chambers under LHC conditions over years. Thus no grease, oil, neither organic solvents nor organic cleaning agents and no kind of silicone compounds should ever be in contact with the gas. Only materials proved to cause no ageing to drift chambers like Noryl, Neoprene, Viton, Nitril must be used for parts such as O-ring seals, membranes or joints. To prevent graphite caused by attrition from proliferation into the gas circuit a filter should be considered after the compressor, as discussed below.

A lot of effort has been undertaken to find a compressor within these and financial constraints [41]. Pumps of different operating principles have been taken into account:

- **piston pumps**: can be rejected as lubrication of the piston seals is unavoidable, leading to contamination of the compressed gas. Another disadvantage are possible pressure fluctuations correlated to each pump stroke.

- **diaphragm compressors**: are a highly clean solution as the engine is well separated from the gas volume, but on the other hand are very limited in their capability at high intake pressure. Moreover they require fast safety measures against pollution whenever the diaphragm (i.e. neoporene) ruptures. This type also generates pressure pulsing.

---

[27] at 3 bar and 20°C

- **bellow compressors**: allow a bigger displaced volume as the diaphragm type, but nevertheless have similar problems. In addition metallic or teflon bellows are rather expensive and have limited lifetime.

- **rotary sliding-vane compressors**: Their big drawback is that the vanes usually made of carbon composites wear out by friction against the stator, which produces clouds of fine carbon dust.

- **turbine compressors**: have a high speed rotor which drives a relatively small blade wheel, providing a continuous gas flow. Even turbines used in car turbos have been considered, but abandoned as alternative as modifications turned out to be to extensive. The challenge concerning the required purity is here to implement lubricant-free bearings for turbines. This can be realised either by active magnetic bearings or with so-called gas bearings. Following an extensive evaluation of the various specifications a turbine compressor with gas bearings was selected as described in the next section.

3.3.2 Design of the ATC

After contacts with several manufacturers we selected the ATC (Argon Turbo Circulator), a costume-made turbine developed and produced according to the specifications above by the Czech company ATEKO[28]. Pictures of the ATC can be found in appendix A. The circulator was designed as an all-metal construction with no need of any lubrication. The materials of the parts which are in contact with the gas are listed in table 3.5.

part	material
ATC-body	stainless steel
rotor shaft	steel
blade wheel	Al-Si$_5$-Cu alloy
spiral case	Al-Si$_5$-Cu alloy
dynamic gas bearings	Electrografit GU 118 with 5% antimony[29]
separation sleeve	epoxy glass-fiber[30], inner surface coated by a 5 μm titanium layer
O-ring seals	Viton

Table 3.5: material specifications of the ATC

During operation the rotor shaft with the wheel blade attached to one end is held in position by three dynamic gas bearings. Two radial gas bearings on each side compress the gas in their wedged notches due to the tilted shape of the three segments of each radial bearing. At a rotation speed of about 4000 rpm the density of this argon cushion is high enough to lift off the rotor shaft. At this stage the shaft hovers with a clearance of

---

[28]Aparáty Technologie Konstrukce, Hradec Králové, Czech Republic
[28]produced by Kompozitum Topolcany, Slovakia
[30]Epoxy DIN 7735 - HGW 2375

nominal operating gas flow	$100\,Nm^3/h$
maximal flow rate	$200\,Nm^3/h$
gas pressure at inlet	$\approx 2.9\,bar$
gas pressure at outlet	$\approx 3.2\,bar$
maximal power at full speed	$2.5\,kW$
maximal speed	$65000\,rpm$
electrical supply	$3 \times 380\,V$ 3 phase, up to $4.54\,A$ each

Table 3.6: Operation parameters of the gas circulator ATC [42]

approximately $60\,\mu m$ above the bearings. Therefore no attrition occurs and the machine can run without any maintenance for years. Nevertheless until reaching the lift-off-speed abrasion of the bearings is unavoidable. The working principle of the radial bearings limits the area of operation regarding flow and pressure. Measures to prevent damages of the bearings are mentioned in section 3.4.

The relative light and small wheel blade[31] is driven by the shaft with rotation speeds up to $65000\,rpm$ and the shape of its blades is responsible for the Δpressure-flow characteristic of the ATC (see section 3.5.2). The gas entering axial to the wheel is accelerated tangentially to be collected by the enclosing spiral case towards the outlet on the high pressure side. Similar to a ship's propeller a axial thrust force towards the shaft appears. To compensate this force a so called thrust bearing is mounted on the opposite end of the rotor shaft. A disc with spiral grooves compresses again gas during rotation, leading to a clearance of a few μm against the end cap. The ATC is only allowed to be operated in horizontal position.

As this high frequency motor acts as a so called squirrel cage motor, no collector rings are needed to feed the rotor windings. In fact the rotating stator field itself induces a current into the rotor windings which in turn let them follow the revolving field with a certain slip. To keep the gas clean even in the situation of burned stator windings, they have been separated gas-tight from the rotor with a thin tube made out of epoxy glass-fiber coated with a $5\,\mu m$ titanium layer. The use of insulating material is essential in this region to prevent heat-producing eddy currents. The sealing of the separation sleeve is as well as the sealing of the two end caps to the ATC-body done with Viton O-rings.

The heat[32] produced in gas bearings and stator windings is dissipated with cooling water channels around the stator as well as in the rear cap next to the thrust bearing. Two thermistors are installed near to the stator windings to detect overheating.

In table 3.6 the most important operation parameters of the ATC are summarised.

---

[31]diameter of $\approx 50\,mm$
[32]about $150\,W$

3.4   Control System and Interlock Measures

Since the planned operation of the prototype system at the Gamma Irradiation Facility (GIF, see section 4.1) was from the beginning foreseen as a longterm ageing study, precautions had to be taken to allow the system to run without continuous presence of personnel. A dedicated monitoring and control system has thus been developed, which is described in the following section. The monitoring system has the double function of

- **Monitoring and recording** all slowly varying parameters of the system needed for a later analysis of the (ageing) data. The interval between measurements for this purpose is usually chosen on the level of one minute.

- **Continuously checking** for any anomalous and potentially dangerous conditions in the system, i.e. in the described setup mainly in the turbine circuit. Such a fault might cause damage very quickly (imagine e.g. a serious gas leak in the big loop, such that the minimum necessary pressure at the input of the ATC would no longer be sustained with the consequence of a damage to the gas bearings of the compressor) and thus has to be detected very quickly, certainly on a time scale far smaller than the standard parameter recording for later analysis.

3.4.1   Turbine control

For all of the slow control tasks, LABVIEW 6i [43] has been used as development environment. This platform was preferred to the PVSS package [44], which will be used for slow control of the LHC detectors, as it provides a faster, more straightforward approach for implementing the needs of a prototype like the one described here.

The purpose of the turbine control program (MDT_pump.vi[33], figure 3.4) is to allow a secure and stable operation of the ATC under different rotation speeds according to the safety measures stated by the manufacturer [45]. Some of these precautions are already covered by the frequency controller[34], driving the pump, itself. In this regard the following parameters, stored in the flash memory of this general purpose motor control device, have been configured to the corresponding limits:

- **minimal rotation speed:** $40\,000\,rpm$

- **maximal rotation speed:** $52\,500\,rpm$

- **acceleration ramp:** increase of the rotation speed of $3000\,rpm$ per second

- **deceleration ramp:** decrease of the rotation speed of $6000\,rpm$ per second

- **electric current limit:** $1.5 \times$ nominal current $= 6.8\,A$

---

[33]a single program or subprogram is called VI (Virtual Instrument) in the concept of LABVIEW
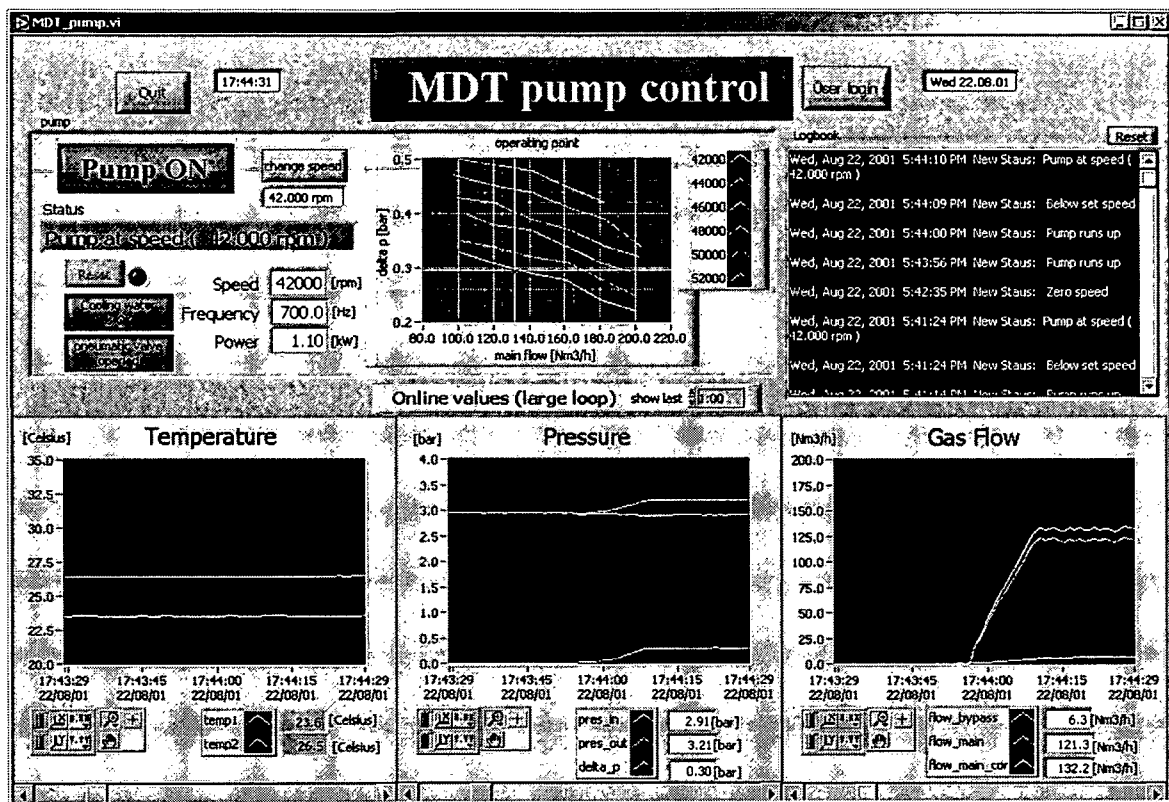[34]UNIDRIVE 1404, Control Techniques Drive Ltd., UK

Figure 3.4: Screenshot of the MDT_pump panel after launching the turbine

- **overheating of the motor coils:** There are two PTC-thermistors installed in the stator windings, which let the frequency controller trip whenever the temperature exceeds a threshold around 140 °C.

- **sense of rotation:** As the gas bearings would be destroyed quickly whenever the motor shaft is driven in the wrong direction, the frequency controller was forced by an internal flag to permit only the design sense of rotation (clockwise seen from the wheel blade side). Nevertheless attention has to be paid not to swap the electric phases whenever recabling of the electricity supply becomes necessary.

All the other critical quantities for running the ATC without risking any serious damage are continuously checked by the turbine control software. Since Profi Bus modules, like the frequency controller, keep their state also in the case of stuck communication, a hardware watchdog was implemented into the SCADA[35] system, to prevent the compressor from keeping on running although the control PC had already crashed. Therefore the control program has to toggle a digital output within a certain time period (set to ∼ 3 seconds) to retrigger a monostable circuit, otherwise a relay opens, resulting in an external hardware trip of the frequency controller, which immediately shuts down the ATC. A further safety advantage of the watchdog is that without starting the control program sending its watchdog signal, the frequency controller is locked. Therefore the

---

[35]Supervisory Control and Data Acquisition

ATC can not be launched unintentionally. In this context another safety mechanism was implemented into the control software. Whenever a missing acknowledge for a shutting-down command is observed, the program simply quits so that the hardware watchdog consequently will turn off the ATC in any case.

So all remaining safety issues concerning the compressor can be monitored by the control software without any undesired effects in case of a software crash. The Program MDT_pump.vi is responsible for monitoring the

- **inlet and outlet pressure** within the turbine circuit: Both, a too low and a too high pressure will cause harm to the ATC. A low pressure leads to vibrations which quickly will damage the gas bearings and the blade wheel beyond repair, whereas a too high pressure overloads the bearings. For this reason the in- and outlet pressure is restricted with a software interlock to values between 2.7 and 3.4 bar during operation and has to stay between 2.8 and 3.1 bar before launching the ATC.

- **minimum gas flow:** under a certain gas flow, dependent on pressure and rotation speed, instabilities in the domain of the gas bearings occur, leading again to vibrations and damages. To be safely away from this so called surge region (see also figure 3.7) a software interlock to a minimal flow of 90 Nm^3/h was implemented which is activated time-delayed after the ATC was started and reached its final speed. In principle it could help within a limited range to react on a critical low flow situation by increasing the rotation speed or via opening a motor-actuated bypass valve. For this prototype it was preferred to immediately switch off the ATC in such a case.

- **cooling water flow rate:** The chassis around the stator of the circulator is surrounded with cooling pipes. The ATC manufacturer claims that for a permanent operation a minimum cooling water flow of 1.5 l/min of 20 °C warm water is mandatory. Therefore the threshold of the used water flow monitor[36] was set to about 2 l/min. Moreover it should be mentioned that this flow monitor is situated at the cooling water outlet side to avoid a misinterpretation of the cooling status whenever a cooling water loss takes place on the way from the flow monitor to the compressor.

- **frequency controller status:** For further security the control program will stop the ATC when an abnormal status word is read from the frequency controller, even when the corresponding status bit would already lead to a trip of the drive on itself (like the status bits: load reached, in current limit).

Besides supervising the parameters above, the turbine control program logs all its error messages and also every change of the UNIDRIVE status to the screen and to a log file. Furthermore the operator gets informed via email and SMS whenever the ATC is shut down (not possible in the case of a power cut).
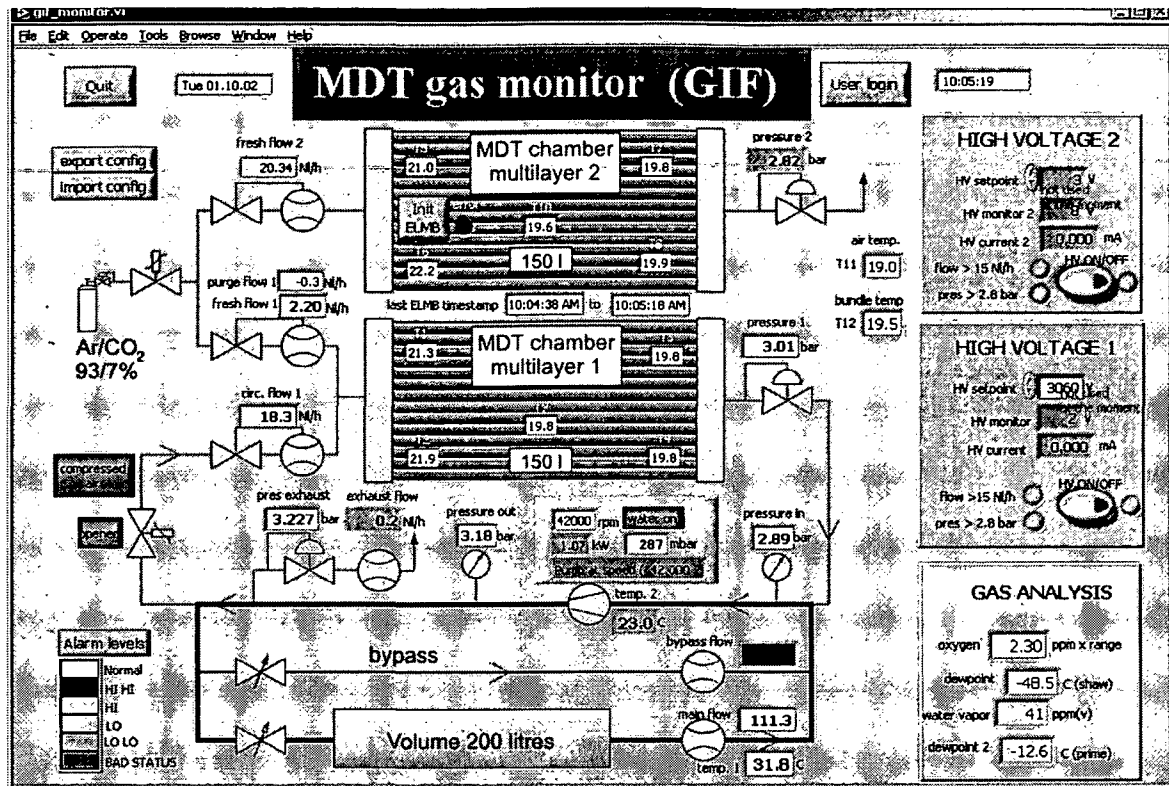
---

[36]Eletta V1-GL15

Figure 3.5: Screenshot of the MDT_monitor panel showing the momentary status of the full gas system

3.4.2 Control Monitor

The standalone program MDT_monitor.vi (figure 3.5) gives a clear overview of the current state of the whole gas system with all the measured flows, pressures and temperatures and moreover shows other slow control measurements like high voltage, temperatures measured on the chamber and readings from gas analysis instruments (oxygen and water meter). The content of each of this 38 control channels is stored every minute into an ASCII-spreadsheet file, which is transferred every midnight to another DAQ PC.

3.4.3 Control DAQ

The architecture of the control DAQ (figure 3.6) is based on the I/O field bus system 750 from the company WAGO. Different kinds of interface modules[37] are plugged in rail-mounted terminal blocks. This modularity, the flexibility to interface to any of the common field busses (CAN, Ethernet, Interbus, Modbus, Profibus) by just changing the fieldbus controller, plus the economical price have been the main criteria why the CERN

---

[37]for this setup 4 analog input modules 750-468 (0...10 V), 1 analog output module 750-550 (0...10 V), 1 analog input module 750-454 (4...20 mA), 1 digital input module 750-402 and 1 digital output module 750-504 (24 V) and 1 module 750-461 for reading 2 PT-100 temperature sensors have been installed, www.wago.com
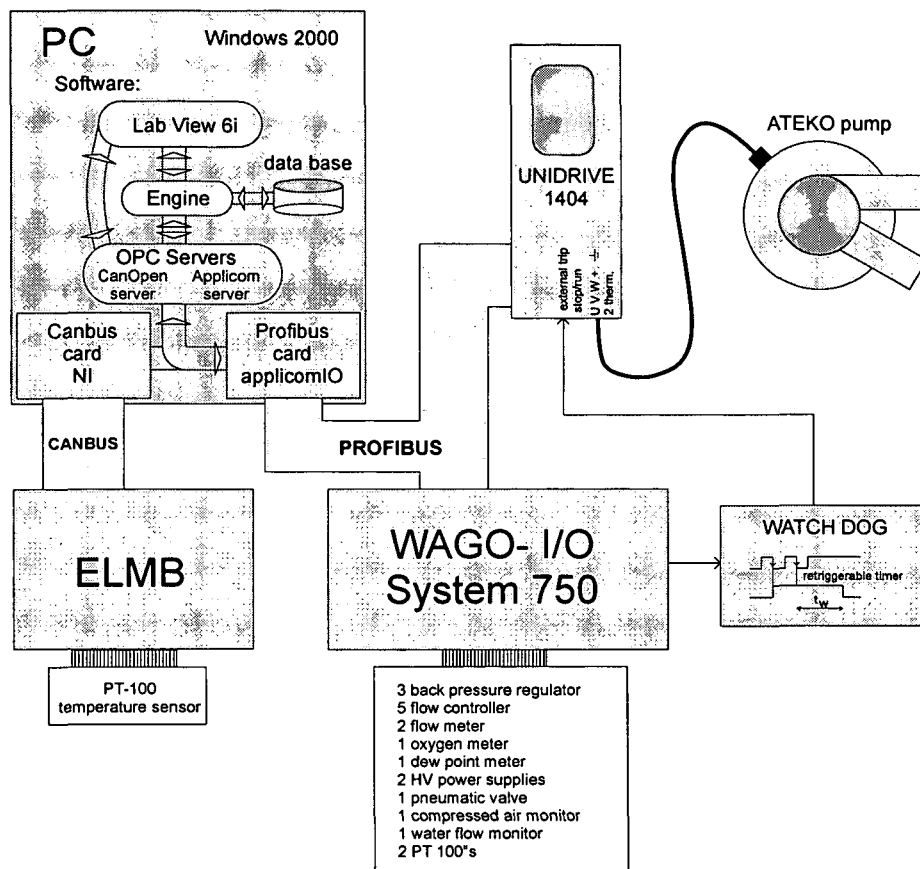
Figure 3.6: Block diagram of the slowcontrol DAQ

EP/TA1/Gas Section recommended this system. The resolution of the analog in- and output channels is 12 Bit and a measuring error of 0.2 % with respect to full scale is acceptable for the measurements of this application.

The Profibus, the fieldbus specified for the ATLAS gas system, was used to interface the slow control PC with the WAGO system, where also the frequency controller (Unidrive 1404) as further station was connected to. One digital output of the WAGO system was used to retrigger the self-made watchdog in regular intervals to avoid an external trip to the Unidrive. The Profibus is controlled by an applicomIO card sitting as PCI card in the slowcontrol PC. Since for the readout of the chamber temperature with PT-100 sensors an ELMB[38] was selected, additionally a CAN bus had to be integrated into the DAQ, managed by a CANbus card. Both field bus controllers are communicating via their OPC[39] servers (Applicom server and CanOpen server) with the so called ENGINE. The ENGINE is the server of LABVIEW 6i which keeps the handling of the I/O-items, like updating their values, converting them from raw to physical relevant values, generating

---

[38]Embedded Local Monitor Board [46], a plug-on module to be used in LHC detectors for a range of different frontend control and monitoring tasks.

[39]OLE for Process Control, whereas OLE in turn stands for Object Linked Embedded

name of volume	leak rate	size of volume
BIS chamber on its own	$2.5 \cdot 10^{-2}\, mbar\, l/s$	$\sim 300\, l$
	$1 \cdot 10^{-4}\, mbar\, l/s\, per\, tube$	$\sim 1.2\, l$
flushed system inclusive ML 2	$2.6 \cdot 10^{-2}\, mbar\, l/s$	$\sim 150\, l$
circulated system inclusive ML 1	$6.8 \cdot 10^{-2}\, mbar\, l/s$	$\sim 350\, l$

Table 3.7: leak rates at $3\, bar$, measured with temperature-compensated pressure drop method

alarms, recognising access levels of users and so on by autonomous processes in the background. In this way the items of many different hardware drivers are available in a uniform and manageable manner within the slow control application.

3.5 Experiences with the Prototype Gas System

3.5.1 Leak Rate

The size of a leak can be expressed by the number of gas molecules leaving this leak per time-unit. For an ideal gas with the gas equation $pV = NkT$ at a given temperature T the particle flow $\dot{N}$ therefore is given by

$$\dot{N} = \frac{1}{kT} \frac{d(pV)}{dt} = \frac{1}{kT} Q_l \tag{3.3}$$

As Q_l is proportional to the molecules leaking from the system's volume and even more practical, this term is normally used to quantify the leak rate. For a given system's volume V this leakrate can directly be gained from a pressure drop measurement:

$$Q_l = V \frac{dp}{dt} \tag{3.4}$$

For the MDT's the specification for the upper limit of the gas leak rate is $10^{-5}\, mbar\, l/s$ for an individual drift tube and $2 \cdot 10^{-5}\, mbar\, l/s$ per tube for a fully mounted chamber, which is checked during chamber production [40]. However for the used BIS module zero chamber this tight leak rate specification was not met and was higher by a factor 5. The measured leak rates for the chamber and for the two parts of the gas system including the respective multilayer are listed in table 3.7. A lot of care was taken to find leaks in the system[40], which consists of around 120 Swagelok gas connections plus about 50 NW-50 clamping rings used to build up the "big loop".

3.5.2 Gas flow versus pressure difference created by the ATC

When discussing the relation between a given flow rate through a system and the pressure drop Δp necessary to sustain it, the two limiting cases of laminar and turbulent flow behaviour have to be distinguished. This stems from the fact that the resistive forces

---

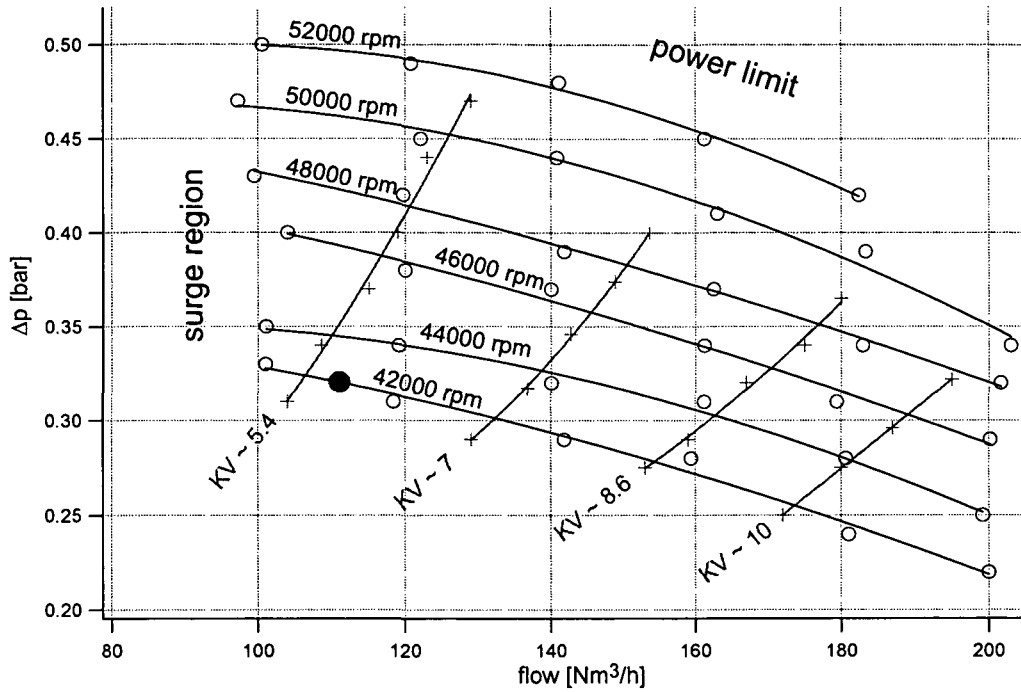[40]with bubble spray and leak detector

Figure 3.7: Flow-Δpressure characteristic of the ATEKO Turbo Circulator. For the graphs with fixed turbine rotation speed the restriction in the system was varied with valve (15); for the curves with fixed K_v value the valve settings was left unchanged but the pump speed was varied instead. The standard working point used for the ageing test is marked (*red circle*).

(friction) affecting the free flow of viscous fluids are highly dependent on the flow regime. For laminar behaviour the fluid can be thought of as a set of different layers which move against each other without intermixing, while turbulent behaviour is characterised by the random displacement of finite mass elements of the fluid which mix strongly with each other. To quantify the level of turbulence the dimensionless Reynold number Re can be used:

$$Re = \frac{\rho w D_h}{\eta}, \tag{3.5}$$

where ρ is the density, w the stream velocity, D_h the equivalent diameter and η the dynamic viscosity[41]. For a given setup there is a range of critical Reynold numbers in which the transition from laminar to turbulent flow behaviour takes place.

For circular pipes the lower limit of this transition region is at a Reynold number of approximately 2300 [47]. In our case[42] the Reynold number of the flow in the "big loop" is around 50 000, thus in the highly turbulent regime, whereas a Reynold number of

---

[41]η is the ratio of the shear stress τ to the velocity gradient normal to the direction of fluid motion, i.e. $\eta = \frac{\tau}{dw/dy}$

[42]Ar:CO_2 (93:7) at 3 bar and 30 ^{0}C $\Rightarrow \bar{\rho} = 4.79\,kg/m^3$ and $\bar{\eta} = 22.2\,10^{-6}$ Pa s, $D = 50\,mm$, volume flow $Q = 100\,Nm^3/h$, $w = \frac{4Q}{p/p_0 D^2 \pi} = 4.7\,m/s$
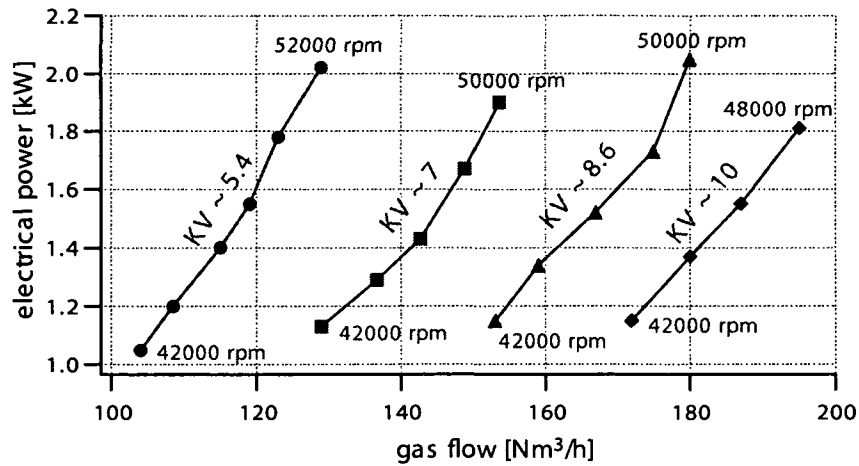
Figure 3.8: Consumed turbine power over the delivered flow for different system restrictions. The rotation speed of the turbine was incrementally increased by $2000\,rpm$ until the current interlock threshold was reached during acceleration.

about 150 in the pipes supplying the chamber indicates a quite laminar behaviour.

The pressure drop needed to achieve a certain flow rate can in the general case be expressed as the sum of two terms which are proportional to the first and second powers of the velocity of flow w [47]:

$$\Delta p = k_1 w + k_2 w^2. \tag{3.6}$$

At very low Reynold numbers ($Re < 25$) the second term can be neglected, leading to the well known law of Hagen-Pouiseuille, while at very large Reynold numbers ($Re > 10^5$) only the quadratic term contributes.

A set of such Q_{flow} versus Δp curves, defining the characteristic of the ATC, were measured for the "big circulation loop" of the prototype system and can bee seen in figure 3.7. The six graphs with rather small negative slope where taken at a fixed rotational speed of the compressor, with different flow rates achieved by adjusting the manual valve (15). The four curves with steep rising slope were on the other hand taken with a constant flow resistance (manual valve setting fixed). This is the situation described by equation 3.6. One sees that for a fixed resistance in the system, i.e. fixed so called K_V value, the pressure difference needed to be built up by the compressor increases strongly with the delivered flow. Reachable flow rates are restricted by the limit on the power of the turbine motor. A careful look at figure 3.7 also shows the major contribution of turbulent flow behaviour, since an extrapolation to the measured points using only the linear part of equation 3.6, $\Delta p \sim w \sim Q_{flow}$, would intersect the horizontal (flow) axis at values far to the right of zero flow, as one expects when approximating a parabola by a tangent to one of its point.

The importance of the compressor characteristic lies in the fact that for the later Atlas gas system one specifies the overall flow rate, ranging from a nominal exchange rate of 1 volume per day up to 2 volume exchanges per day. Given the resistance of the system, figure 3.7 yields the needed pressure difference, which can be generated by adjusting the

rotational speed of the compressor. Without changes in the system resistance (K_V-value) the band of accessible flow rates is severely limited by the power and surge limits (see also figure 3.8). Therefore adjustable throttle valves will be installed into the final gas system (see section ??). Under nominal flow conditions they take a significant part of the overall pressure drop, which is adapted to lower values whenever running with higher flow.

3.5.3   Pressure and Flow Stability

Seen from the MDT gas system the most essential stability criteria the ATC turbine has to fulfil are the created pressure difference and the main flow in the "big loop". A typical trend of both quantities are shown in figure 3.9 over a period of 24 hours. One can see that they stay constant within 3 % (Δp) and 1 % (flow) correspondingly, which is adequate for the later ATLAS operation.
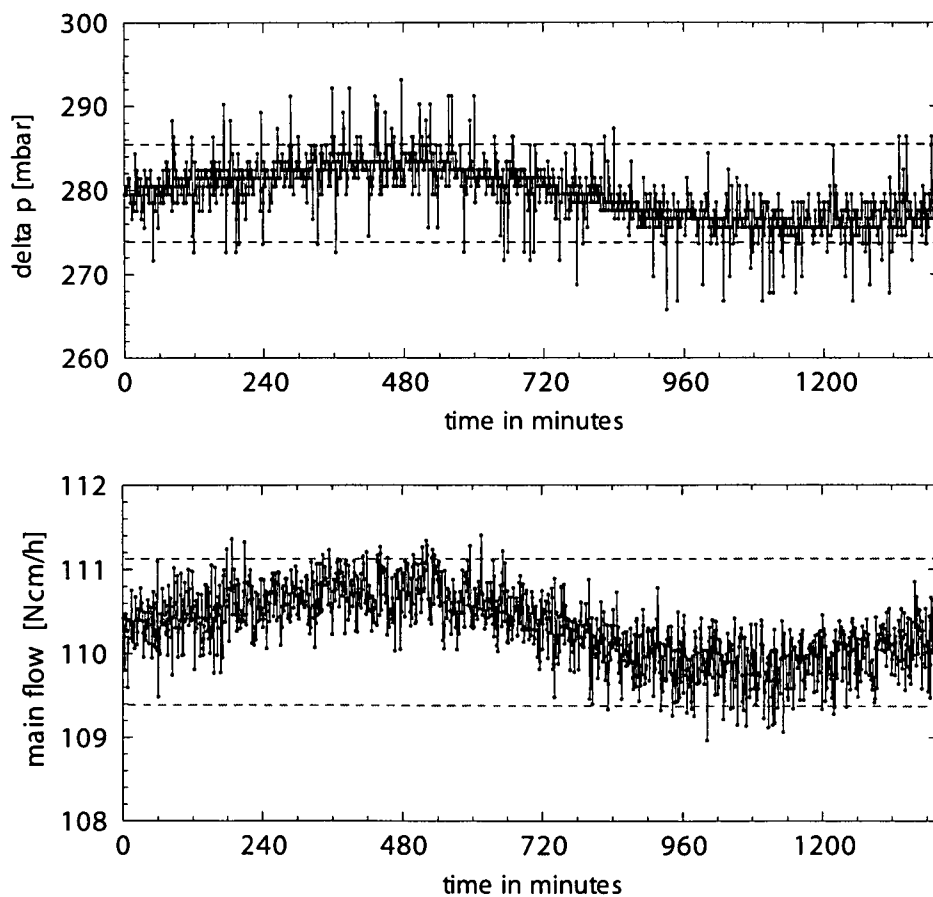

Figure 3.9: Measured pressure difference between in- and output of the ATC (*top*) and gas flow rate (*bottom*) in the "big loop" over 24 hours. The stability is, except for isolated points due to noise spikes on the analogue slowcontrol readings, better than $\approx 3\%$ for Δp and better than 1 % for the flow rate. The turbine was operated at $42\,000\,rpm$.

3.5.4   Influence of Water Vapour on the Drift Properties

During the long-term ageing test (see chapter 4 for details) drift time spectra with cosmic muons have been measured in weekly intervals to monitor the stability of the drift properties of the gas. The maximum drift time t_{max} was determined from the drift time spectra with the fit method described in section 6.2 as chosen parameter for the gas behaviour. In the initial period of the ageing test (see also sec. 4.2) between March and May 2002 a clear increase of the maximum drift time was observed in the multilayer connected to gas circulation. As a change in the water content in the recirculated gas system was suspected to be the cause of the increased drift velocity, a dewpoint meter for measuring the water content was installed directly into the circulated gas flow coming from multilayer 1 in the second period of the test.
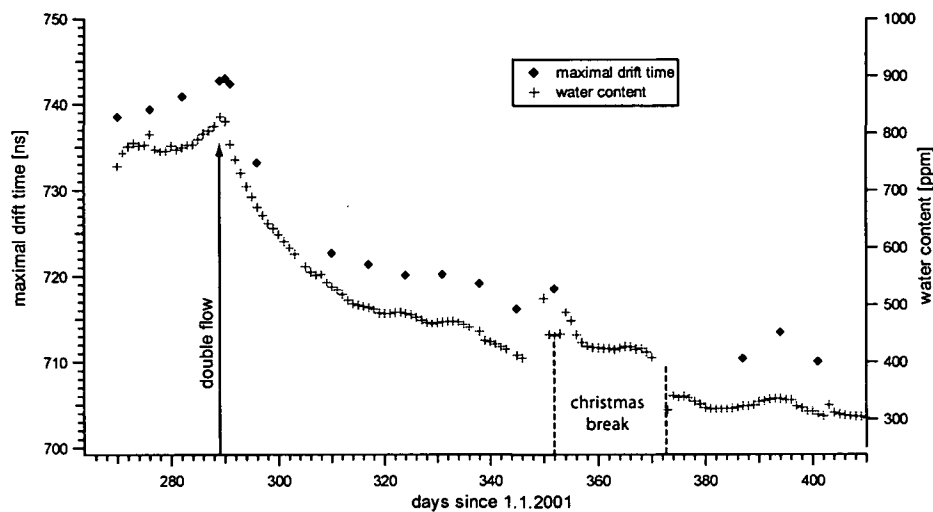

Figure 3.10: Evolution of the maximum drift time (temperature corrected) of the drift tubes of multilayer 1 due to the change of water amount in the recirculated gas system

Figure 3.10 shows the result of these measurements. After increasing the recirculated flow from one to two volume exchanges and due to the environmental temperature and humidity drop the water vapour amount in the recirculated gas system decayed from $\sim 800\,ppm$ to $\sim 300\,ppm$ within four months. The maximum drift time, indicated in the same figure, emerged to be highly correlated to the variations of the water content. When plotting the two figures against each other (figure 3.11), a dependency of about $6.5\,ns/100\,ppm$ water is obtained for the maximum drift time which is compatible with the measurement obtained in the 2002 testbeam studies [38] (see also sec. 3.1.5).

3.5.5   System Behaviour in Case of Circulation Failure

Since the gas system was supposed to run for several days without any supervision a number of safety measures had to be taken into account to protect the chamber and
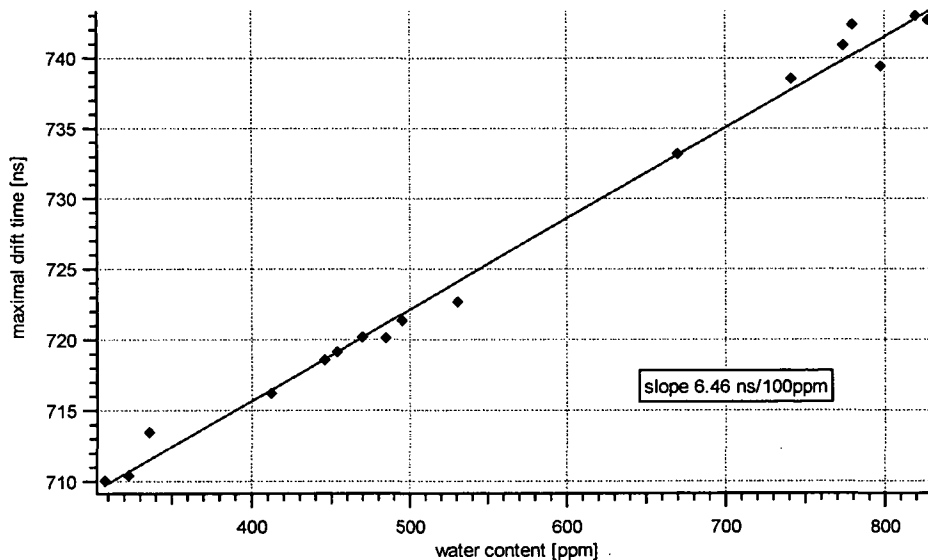
Figure 3.11: Correlation of the maximum drift time with the water content

the turbine. All software and hardware interlocks which lead to a safety shut-down of the turbine have been described in section 3.4. These scenarios plus the case of a power cut will therefore stop the gas circulation and equalise the pressure in the "big loop" to $\sim 2.9\,bar$ since the low-pressure buffer volume dominates. Nevertheless the fresh flow via flow controller (4) keeps on flushing the chamber which still is regulated to 3 bar as long the minimum required pressure drop of $\sim 100\,mbar$ over the controller (10) is ensured. In addition the flow out of the chamber fills the "big loop" as well. Therefore the pressure difference over (10) slowly decreases forcing it to open it's control valve. In this way the pressure in the chamber increases in common with the "big loop" until the set point of the exhaust pressure regulator (11) is reached, so that the "big loop" gets vented again and stabilises to this set point (around $3.2\,bar$). According to the quality control specifications this pressure is uncritical for the MDT's as they are tested for $4.5\,bar$.

The described process takes about 24 hours. After such a long circulation interruption gas has to be released (with valve 19) to bring the "big loop" back into the operation regime of the ATC. Since non-observance to this will damage the turbine, the pressure ranges are checked by the computerised control before allowing a restarting of the circulation.

It should be mentioned that a interlock to the high voltage of each multilayer was also implemented. To avoid undesired additional ageing effects caused by small gas flow combined with the electrical field, the high voltage for the concerned multilayer is switched off by a HV-Relay whenever the slow control program detects low flow conditions[43]. Therefore the high voltage of multilayer 1 has to be restarted as well after a circulation failure. Also low pressure situations[44] initiate a HV-trip to prevent spark formation.

---

[43]threshold 15 Nl/h

[44]under 2.5 bar

3.5.6 Electromagnetic Compatibility and Induced Noise

The stator windings of the ATEKO turbine, which are generating the electric field to drive the rotor, are supplied as alternating 3-phase current by a general purpose motor control device[45]. This motor drive converts the standard $3 \times 220\,V$ industrial electrical supply with pulse width modulation into the required alternating 3-phase voltage. The amplitude is ramped up together with the angular frequency during accelerating the machine until the desired rotation speed is reached (up to $65000\,rpm's$).

The combination of high power (up to $2.5\,kW$), alternating currents in the kHz domain together with the highly sensitive MDT front end electronics, where un-amplified signals are in the μV range, turned out to be problematic. When the chamber was operated the first time together with the gas circulation running (November 2001) the situation was indeed so bad that basically all 240 drift tubes were oscillating with amplitudes well above the threshold of $60\,mV$ at the output of the front end electronics amplifier. Reading out the chamber at all proved impossible.

Various approaches to reduce the amount of induced electrical disturbance were tested and an effort was made to actually understand the way noise was induced onto the chamber. The second point seemed especially important since discussions with the manufacturer of the UNIDRIVE frequency controller showed that all such devices were prone to high electromagnetic emission, thus implying a non-negligible risk for the later ATLAS operation.

Table 3.8 summarises the actions taken to eliminate or at least reduce the induced noise problem to an acceptable level. The list should serve as a starting point for later installation and operation.

Figure 3.12 shows measured noise rates on the drift tubes at nominal threshold with the circulatory gas system switched on and off and already after applying the described actions to reduce the electromagnetic emission. There is still a significant difference, especially in the outer tube layers which act as shielding for the inner layers.

Noise propagation onto the MDT chamber

One is tempted to think that the problem with electromagnetic emission by the ATC controller will not be a concern for the later ATLAS setup due to the large spatial distance[47] between gas system (surface building) and detector (cavern). This is certainly true if noise is induced on the chamber by direct electromagnetic radiation through the air, but is less obvious if electric disturbances travel via conducting materials and/or the earth connections. During a gas zone refurbishment at GIF in February 2002 the situation was used to understand the mechanism of noise propagation. The following

---

[45]UNIDRIVE UNI 1404, Control Techniques Drive Ltd., UK.

[46]The RF passive filter works by dissipating spike currents up to $7\,mA$ directly to GND. This puts some strain on the otherwise balanced 3-phase supply. It was further observed that the current was enough to regularly trip the standard FI protection device in the 220V/380V line, which had to be taken out.

[47]about $120\,m$

action	mechanism	importance
Connect the motor cable shield solidly to Earth (back plane) within $10\,cm$ of the controller [48]	Shielding	*****
Connect controller and pump motor using a cable with a metallic shield. [48]	Shielding	***
Mount Controller on sturdy metallic back plane , Earth separately	Grounding	***
Decouple the metallic gas pipes from the chamber by insulating pieces both at the chamber input and between gas rack and piping	Limit noise propagation	***
Avoid any coiling up of spare cable length between controller and motor	Limit e.m. emission	**
Install the foreseen Atlas MDT RC-filter circuit in the chamber HV supply line close to the chamber	Filtering	**
Use a special RF filter, type 4200-0010, Control Techniques Drive Ltd, in the AC supply to suppress propagation of noise spikes over AC network and power GND [46]	Filtering	*

Table 3.8: Actions taken to reduce the problem of induced electric noise on MDT front end electronic caused by the ATC

was found:

- Connecting the gas system to a different electrical supply from the chamber electronics did not improve the situation. A propagation via the 220V/380V ground is therefore unlikely.

- With the metal pipes between gas zone and GIF area ($\approx 20\,m$ distance) removed no difference in measured noise rates could be observed when switching the ATC on and off.

This behaviour shows that the dominant mechanism of noise propagation is via the conducting gas piping. From there it is transmitted via electromagnetic radiation (antenna effect) to the chamber, because direct contact between chamber and gas lines was excluded by insulated decoupling pieces at the chamber input as well as at the gas rack side. Since disturbances distributed via conducting materials do not necessarily scale down with distance, the question of electromagnetic compatibility should be taken seriously also for the final Atlas installation.
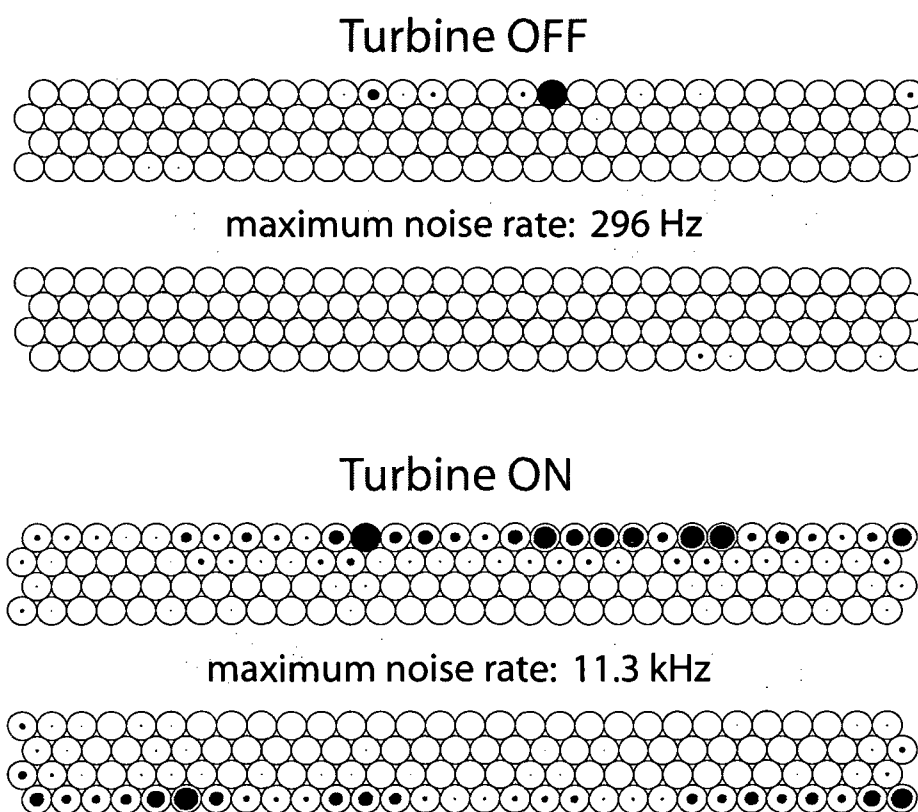
Turbine OFF

maximum noise rate: 296 Hz

Turbine ON

maximum noise rate: 11.3 kHz

Figure 3.12: Measured single tube noise rates at nominal threshold $(60\,mV)$ with the ATC switched off (*top*) and running (*bottom*) after the electromagnetic emission had been reduced by the methods described. The area of the filled circles is proportional to the measured count rate.

Chapter 4

The Ageing and High Rate Test Setup

This chapter gives a description of the experimental setup used to perform the ageing and high rate studies documented in the next two chapters. An inner station MDT chamber (sec. 4.3) was exposed to intensive gamma radiation at the CERN Gamma Irradiation Facility (sec. 4.1) during a period of over one year (sec. 4.2) to test the detector performance in ATLAS-like irradiation conditions. The recirculated gas prototype was supplying the chamber as described in the last chapter. An almost final front end electronic and a prototype DAQ was in use to collect drift time data (sec. 4.4). In addition pulseheight spectra of cosmic muons have been collected weekly with external ADC's (sec. 4.6) to follow up long-term pulseheight variations. Triggering the cosmic muons was done with the implementation of a scintillator hodoscope (sec. 4.5), which also recorded timing data to allow the reconstruction of the muon tracks. For the testbeam period a modified setup, with three scintillators in coincidence as beam trigger, was in use (sec. 4.7).

4.1   The Gamma Irradiation Facility

The studies described in this work were made in a test area called the Gamma Irradiation Facility (GIF), situated in the SPS West Area at the downstream end of the X5 test beam. The facility is meant for testing large area detectors exposed to this test beam under the presence of a high background photon flux, which creates working conditions similar to the future LHC-environment.

4.1.1   Photon Source and Filters

A radioactive ^{137}Cs source, barrel-shaped and $8\,mm \times 8\,mm$ in size, is emitting $662\,keV$ photons with an activity of $655\,GBq$ [1] into a pyramid-shaped volume with an fixed aperture angle of $74^o \times 74^o$ (see figure 4.1). A set of moveable lead filters allow to attenuate remotely-controlled the gamma flux over several orders of magnitude. The filters are shaped like convex lenses to offer a constant gamma flux for detectors aligned in planes

---

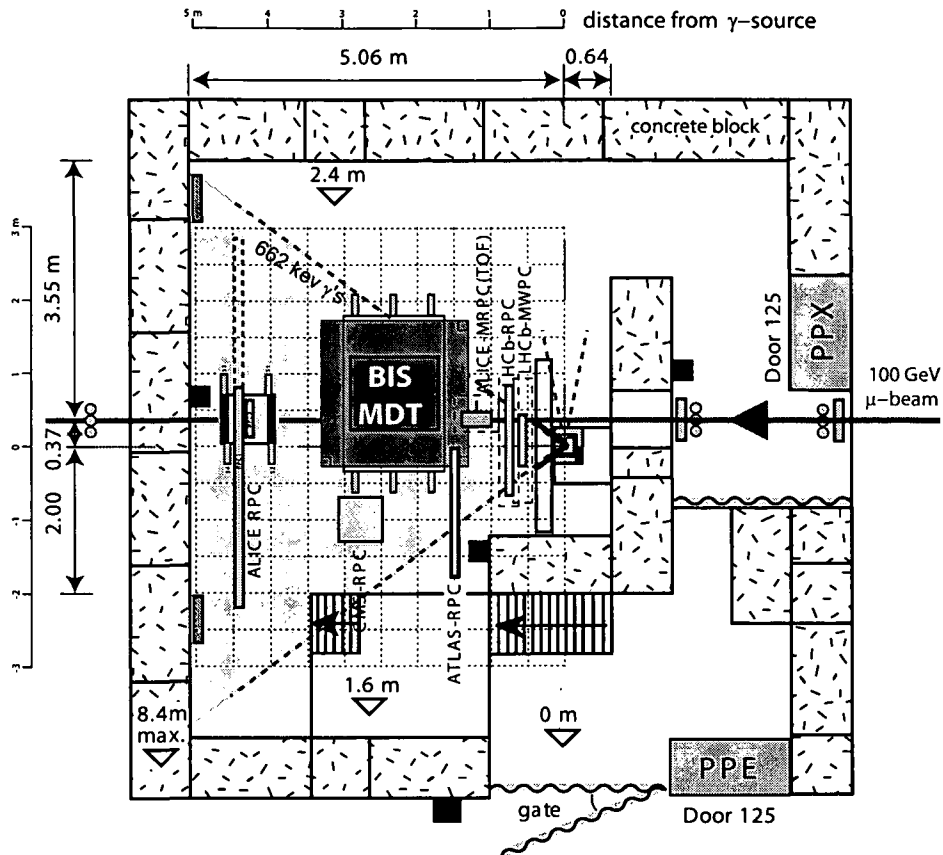[1]valid in June 2002, decayed from $740\,GBq$ measured in March 1997

Figure 4.1: Plan view of the Gamma Irradiation Facility at CERN. Highlighted are the container housing the ^{137}Cs source (*orange*), the irradiated area (*yellow*) as well as the X5 muon beam (*blue*). The drawing shows the position of the hodoscope structure (*green*) with the MDT-BIS chamber (*red*) during the ageing period 1 (see next section).

perpendicular to the symmetry axis of the irradiated pyramidal area. Measurements carried out when commissioning the GIF area [49] affirmed this uniformity, whereas for the MDT setup described here, especially during the testbeam period, the lateral gamma counting rate along the chamber was observed to be not uniform (see section 6.1). This behaviour was understood to be caused by irregular shielding effects of several small size setups located between the ^{137}Cs source and the MDT setup.

Beside the sharp and dominating primary gamma peak at 662 keV a broad lower energetic photon spectrum arise from scattered compton photons, produced in the filters, as well as from compton photons backscattered from the concrete walls and the floor. Downwards the continuous spectra is overlaid by a fluorescent X-ray peak at 72.1 keV from the lead filters.

4.1.2   X5 Testbeam

The testbeam reaching the GIF zone, called X5, stems from protons with an energy of about $450\,GeV$ extracted from the SPS ring. During this extraction cycle of about $4.8\,s$ (with a repetition period of $16.8\,s$) the protons smash into a beryllium target, creating the hadrons and electrons which are momentum selected and transported by the so-called H3 beam line to the X5 secondary target. From there electrons and muons, decaying from pions and kaons, are guided along the $\sim 200\,m$ long X5 beamline to the GIF area. A iron dump with a thickness of $5.4\,m$ in front of the zone stops all particles except muons. The muons in the presented studies had an energy around $100\,GeV$ with a flux of between 2000 and 6000 particles per spill concentrated in a beam spot of a diameter varying between 10 and $20\,cm$.

4.2   Data Taking Periods

The design and assembly of the gas system including development of the control software as well as debugging the BIS cosmic setup was accomplished in 2001. In November 2001 the whole setup was installed at GIF for the first time. Since then three different ageing campaigns and one test beam campaign took place (pictures of the setup in the different periods can be found in appendix A):

- **Preparation Period** (end of 2001): In this phase the setup was debugged and commissioned on site. A lot of effort was spent to improve the noise situation induced by the turbine control device (see section 3.5.6). Therefore no gas circulation was used in this period to avoid electromagnetic interferences with the front end electronic. Only a few mC charge per tube and cm were collected.

- **Gas Zone Rebuilding** (January - 15.03.02): The whole piping between GIF and the gas zone had to be refurbished, therefore no radiation was available. Cosmic data was taken and an auxiliary temporary gas system flushed the chamber.

- **Ageing Period 1** (15.03.02 - 10.05.02): Around $20\,mC/cm$ per tube have been collected with normal and double[2] gas gain and multilayer 1 under gas circulation. To follow up the ageing behaviour weekly reference measurements with cosmic muons and gamma irradiation "switched off" have been taken. The setup geometry of this period is shown in figure 4.2.

- **Testbeam Period** (27.05.02 - 07.06.02): This period was availed for high rate studies. A setup with the BIS chamber mounted vertically was installed (see also figure 4.8), to be capable of rotating the chamber, for data runs with different angles of incidence needed for autocalibration. No gas circulation was applied to suppress effects due to increased noise induced by the turbine controller.

- **Ageing Period 2** (27.09.02 - 05.03.02): In this phase the main part of charge accumulation ($\sim 180\,mC/cm$ per tube) took place with the help of an increased

---

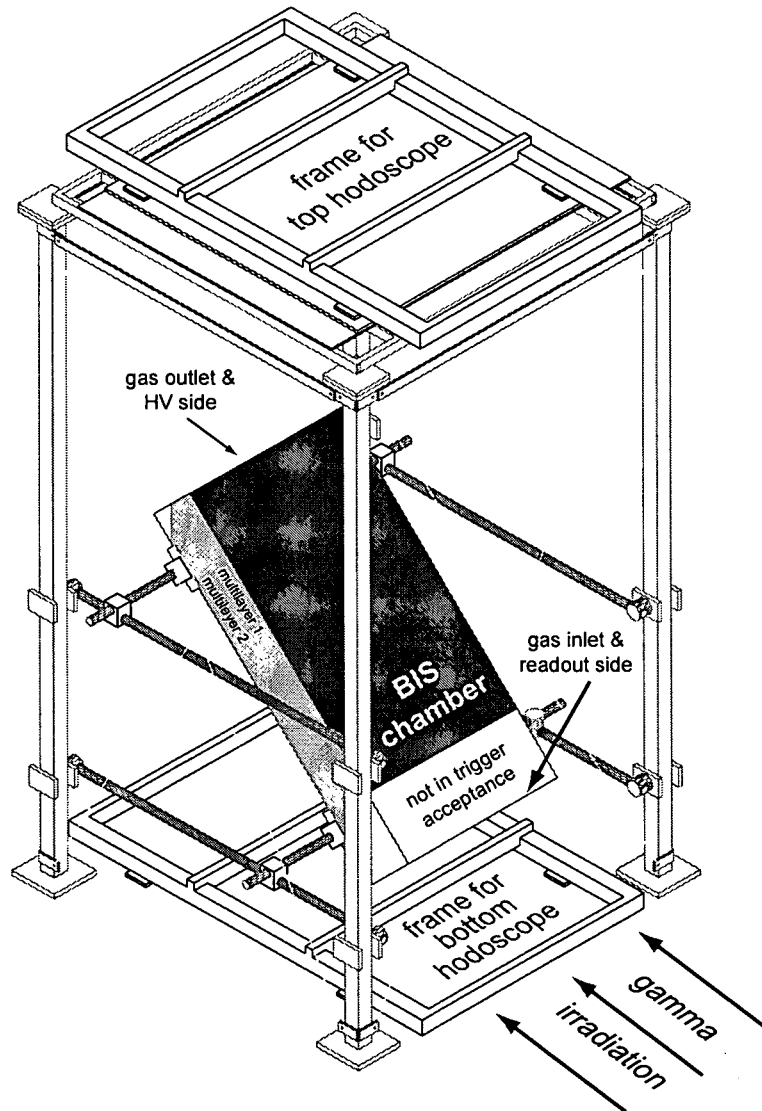[2]$G = 4 \times 10^4$ which corresponds to a high voltage of $3180\,V$

Figure 4.2: The over $4\,m$ high MDT-BIS ageing setup during period 1. Due to the inclined mounting, the chamber is exposed to the γ-irradiation as well as to cosmic muons. The hodoscope scintillator strips (not drawn here) are perpendicular to the BIS drift tubes, which allows to determine the cosmic muon track position in tube direction relatively accurately from the pattern of the scintillator hits. The chamber volume covered by the cosmic trigger is marked (*filled area*), showing that the first 20 to $30\,cm$ from the gas inlet side are outside the trigger acceptance.
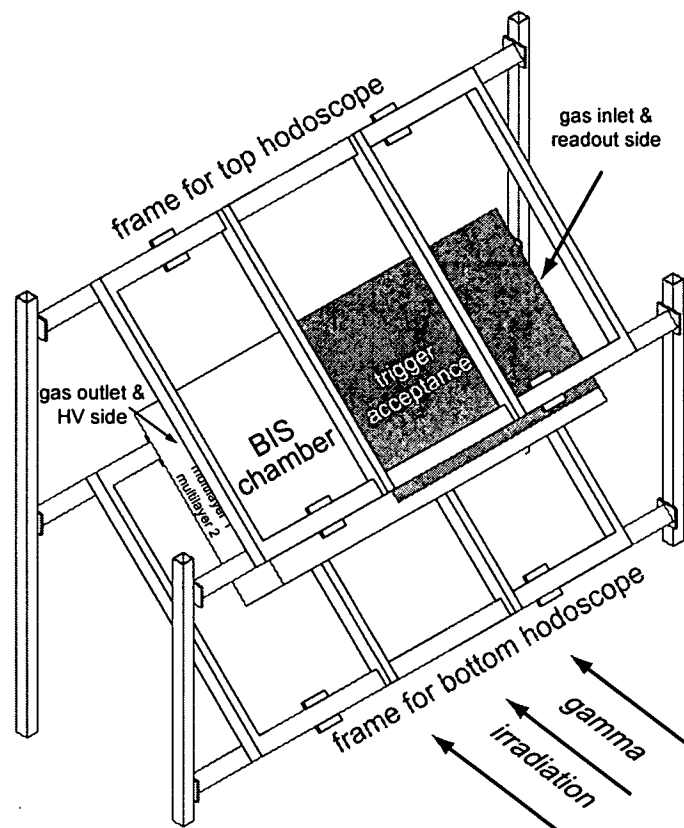
Figure 4.3: Hodoscope and MDT chamber layout during ageing period 2. To reduce space requirements the hodoscope scintillator strips have been mounted parallel to the Bis drift tubes. Therefore it was necessary to reconstruct the muon track position in tube position from the less precise scintillator timing information. The hodoscope covers the first meter starting of the Bis chamber from the gas inlet side (*filled area*).

high voltage of $3400\,V$. To partly compensate for the accelerated charge deposit, the gas flow through both multilayers was doubled. Multilayer 1 was further on operated under circulation and again weekly reference runs have been collected. For chamber and hodoscope configuration during this ageing period see figure 4.3.

- **Ageing Period 3** (05.03.03 - 08.05.03): The last period, before dismantling the whole setup, was utilised to study the ageing behaviour of both multilayers in series and connected to the gas circulation. This was done to verify, if the ageing effect observed at the gas inlet of multilayer 1 would appear also at the inlet side of a multilayer 2, following the aged one (see section 5.7).

4.3   The MDT-BIS Chamber "Beatrice"

Given the very limited space available at the GIF area, a BIS type chamber [50], called "Beatrice", one of the smallest Atlas MDT chambers was chosen for the presented studies. This chamber, from the module zero production run, was one of the first MDT chambers with final production design and final components made available. Module zero chambers are only foreseen as spare, making this detector suitable for a potentially risky ageing test at very high intensity.
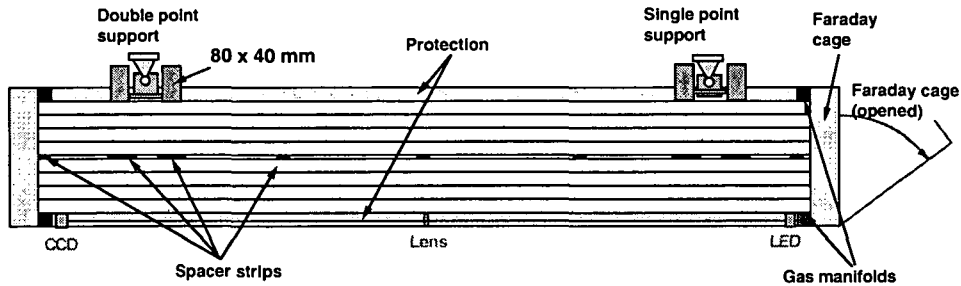

Figure 4.4: Side view of a BIS type MDT chamber.

The BIS Beatrice chamber consists of two multilayers, separated by seven $6\,mm$ thick aluminium strips [51]. Both multilayers are composed of 4 layers each with 30 aluminum tubes of $170\,cm$ length. Each individual drift tube had to pass quality controls like measurements on gas tightness, correct anode wire tension and high voltage leak current [52]. The chamber was produced at the University of Thessaloniki, Greece [53] and checked for the geometrical specifications at the CERN X-ray tomograph [54].

The on-chamber gas system is fully parallel. That means all tubes are supplied directly with small brass[3] tubelets distributed from four gas manifolds $(3 \times 2\,cm^2$ square-shaped aluminum profiles) located at each end of both multilayers. The faraday cage of the BIS Beatrice chamber had to be provisionally modified due to dimension conflicts and limited surface conductivity, since anodised aluminium was used.

4.4   Front End Electronic and DAQ

In this section the data acquisition chain from the induced muon signals up to the binary datafiles, containing the muon traversing time information, is briefly introduced and illustrated in figure 4.5. The type of the electronic equipment used in the present setup on the different levels is specified. Differences to the final ATLAS MDT electronic are pointed out.

---

[3]for the final system it was decided to use stainless steel tubelets due to problems with capillary cracks in the brass material

4.4.1   MDT signal propagation

The induced signal, generated mainly by the ions drifting to the cathode (see section 2.1) at the position where the avalanche process took place, is splitted into two portions which are travelling as electromagnetic waves along the anode wire to the opposite ends of the drift tube. The MDT tube acts thus as coaxial transmission line with a characteristic wave impedance. The part of the signal wave arriving the so called high voltage side of the tube, is absorbed almost completely, as this end is terminated with a $383\,\Omega$ resistor, which corresponds to the wave impedance of the tube.

This termination resistor as well as a RC-low pass filter (see figure 4.5), which suppresses cross-talk among adjacent channels, are mounted on a PCB called HV hedgehog board [55]. For the BIS Beatrice chamber 10 of these boards, each supplying 4×6 tubes with high voltage, have been attached to the HV-pins of the tube endplugs. The HV supply lines are connected for the 30 tubes of each layer and are guided separately through the faraday cage with HV cables and connectors. To reduce noise at this level introduced from the high voltage side, the HV as well as the HV ground lines have been decoupled with an external circuit.

The second part of the signal wave is propagating towards the other tube end, called the signal side of the chamber. There an intermediate PCB, the signal hedgehog PCB [56], is decoupling the unamplified MDT signal from the HV, to pass it on to the preamplifier. The preamplifier in turn is sitting on a PCB called mezzanine card, which is housing all the front end electronic and is plugged on to the hedgehog board. For the present setup a unshielded[4] hedgehog prototype version was used.

4.4.2   Signal Amplification, Shaping and Discriminating with the ASD

The mezzanine card[5] consists of ASD chips (Amplifier-Shaper-Discriminator) [57] and one AMT chip (ATLAS Muon TDC) [58], both fabricated in CMOS technology. The ASD is amplifying and shaping the signal in four successive differential amplifier stages. In the final design bipolar shaping[6] with a peaking time of $15\,ns$ was chosen, as unipolar shaping would have required active baseline restoration and programmable filter time constants for different gases [24]. The sensitivity of the shaper output is about $3\,mV/primary\,e^-$.

Whenever the shaper output signal exceeds a programmable threshold, the discriminator creates a LVDS[7] output pulse. The nominal threshold is specified to be $60\,mV$, which corresponds to about 20 primary electrons or six times the typical noise level [57]. Another difference between the ASD-lite chip and the final type is that no artificial dead time can be programmed. That means multiple threshold crossings, produced by a signal from just one particle, result also in multiple pulse hits at the ASD output. A feature also missing in the prototype version is the built in Wilkinson charge ADC for measuring

---

[4]for better electromagnetic compliant the ATLAS Muon Collaboration decided to employ shielded signal hedgehog boards.

[5]here a prototype called, mezzanine lite card, has been in use, which contains 8 ASD-lite chips each handling 3 MDT channels, whereas on the final mezzanine card 3 Octal ASD are mounted.

[6]the prototype mezzanine card used within this work still used unipolar shaping

[7]Low Voltage Differential Signaling

Figure 4.5: Block diagram of the front end electronic and DAQ used during the BIS ageing and high rate test. The ADC readout chain described in section ?? is shown as well.

the charge in the rising edge of the MDT signal, which can be used to correct time slewing effects [59]. The ASD lite also provides for test purposes an analogue output signal tapped after the third amplifier stage. This analogue output is available for every third channel and was used extensively in the ageing test to gain pulseheight information with the help of an external ADC (see section ??).

4.4.3 Drift Time Measurement with the AMT

The MDT signal pulses of 24 ASD channels, each belonging to one drift tube, are processed in the AMT chip to digitise their arrival times. The 40 Mhz LHC clock[8], which is distributed via the CSM (Chamber Service Module) [?] to the AMT's, gets multiplied internally by a factor 32 due to a circuit combining a DLL with a delay chain. Therefore an AMT counter time value has a time resolution of $0.78\,ns$. Whenever a hit pulse is registered in the AMT the actual counter time value is carried forward to the FIFO level 1 buffer together with the channel number. In this manner up to 256 hits can be held in the level 1 buffer.

When the CSM is sending a trigger request[9], the according trigger time is saved in the trigger FIFO of the AMT's. Every trigger request stored in this list selects all those hits of

---

[8]all LHC experiments are synchronised according to the $25\,ns$ bunch crossing time

[9]for the described setup a trigger is released either by the cosmic or testbeam hodoscope

the level 1 buffer, which have a timestamp falling within a programmable time window, called matching window[10], starting at the trigger time. Optionally a mask window can be set. Then all channels which registered a hit in this mask time window before the trigger are marked with a mask flag[11].

The time and channel information of the matching MDT hits plus header and trailer patterns are subsequently transmitted from the AMT serially in 32-bit word packages to the CSM. Such datastreams coming from up to 18 mezzanine cards are received by the CSM, which, after identifying all the AMT trailers, builds up an event with all the hits carrying to the same event ID[12]. Moreover the CSM-0 prototype handles the initialisation and programming of the ASD's and the the AMT, like e.g. the threshold setting and match window setting, of each mezzanine card via daisy chain JTAG protocol.

For the ageing test, eleven mezzanine cards have been used: ten to equip the BIS chamber fully and an additional one recording the trigger injection time. This was necessary as the hardware triggers are not passed immediately to the AMT's, but only with the next rising edge of its internal 25 ns clock. By subtracting the measured trigger time of the additional mezzanine card from the drift time measurement, one gets rid of this 25 ns uncertainty.

A device called CSM adapter was required for the prototype DAQ in between CSM and mezzanine cards, to supply the latter with power and to distribute the JTAG initialisation signals. As the DAQ rack had to be located outside the GIF area the cable lengths between front end electronics (CSM adapter) and CSM-0 amounted to 25 m. Therefore a specially self-designed LVDS repeater had to be used to ensure proper communication (see picture in appendix A).

4.4.4 Setup Specific DAQ Software

The CSM-0 prototype is build as VME modul with a VME readable output FIFO. With the help of a VXI-MXI-2 bus from National Instruments the CSM-0 was interfaced to a PC running Windows 95.

For data acquisition a modified version of the software "MiniDAQ" developed at the University of Michigan [60] was used for our purposes. Extensions to the original MiniDAQ code included an event display and an immediate data transfer via TCP/IP to a second PC running LINUX for first quick analysis. Central Data Recording (CDR) services running on this LINUX PC copied the data files automatically to the CERN tape storage system CASTOR.

---

[10]was 1 μs by default for the presented work

[11]for the used mezzanine lite, without the artificial deadtime, this feature offered a method to reject faked first hits, arising from a multiple threshold crossing of a MDT signal which started already shortly before the trigger time

[12]The data transfer described here and in the following is specific to the prototype called CSM-0 and to the setup described here. The final CSM version will be mounted on the chamber itself and will have less functionality and acts just as time-division multiplexer for the mezzanine cards of a MDT chamber. It sends the data from up to 18 AMT's via an optical G-Link with up to to a device called MROD, which on its part handles datastreams coming from 6 CSM's

A further important and setup specific extension of the standard MiniDAQ code was the integration of the ADC pulseheight and TDC hodoscope data (see section 4.5) based on the existing event-organised and binary filestructure. For the ADC as well as for the TDC measurement CAMAC modules have been utilised, which were read out also over the VME with the help of the VME module CBD 8210 (Camac Branch Driver). To assure a possibility for synchronising the DAQ data with the slowcontrol data a timestamp was included into every data block.

The DAQ was configured in single event acquisition mode. In this mode the chain AMT-1 – CSM-0 was known to suffer from hang ups because sometimes one or more AMT's do not recognise the trigger signal from the CSM. Consequently no data are transmitted from these AMT's to the CSM, which in turn is waiting for finishing the event building, with the result of a completely stuck readout. This problem was handled in the following way: besides checking the CSM for an event-ready flag the DAQ verifies in a second independent way if a trigger occurred. Whenever such a trigger is detected by the DAQ, it waits the maximum time needed for event processing[13] for the event-ready flag. An absent flag is then considered as stuck CSM status, hence a reset of the CSM is performed by the modified version of MiniDAQ. The independent trigger detection is done by checking the Flip-Flop of a Status-A Camac module, which is set by the hardware trigger signal and cleared by software.

4.5   Cosmic Setup for the Ageing Test at GIF

The longterm requirement of the described setup was to follow up the performance of the studied MDT chamber over a period in which the chamber has to sustain a radiation dose comparable to an operation of 10 years LHC. An evidence of a drift tube's performance degradation due to ageing, is the observation of a signal height decay over time, as an indication of reduced gas amplification. To be sensitive to gas amplification changes, a reproducible distributed amount of primary ion-electron pairs have to be excited in the drift gas. The high-energetic photons from the ^{137}Cs source itself cause Compton electrons in the tube wall, which leads to a continuous energy loss spectrum within the drift gas volume and therefore is not suitable for a study of pulseheight changes. Radioactive sources, like ^{109}Cd, ^{241}Am or ^{55}Fe, with low-energy gamma decays[14] are more convenient, as the produced photo electrons cause a characteristic response spectrum. As regular reference measurements, for collecting such spectra with moveable radioactive sources over major parts of the chamber, would be too time-consuming, the spectra of cosmic muons have been used to monitor the ageing behaviour.

To expose the MDT's efficiently to cosmic muons as well as to the gamma photons, the chamber was installed inclined during the ageing periods (see figure 4.2). The tight space situation at GIF after the 2002 summer period made it necessary to install a new setup with the scintillator hodoscope tilted as well (see figure 4.3).

---

[13]typically about $50\,\mu s$

[14]a $22\,keV$ peak for ^{109}Cd, $17.4\,keV$ for a molybdenum sheet excited by ^{241}Am and $5.9\,keV$ for ^{55}Fe

4.5.1 The Cosmic Hodoscope

The cosmic hodoscope provides the trigger signal for cosmic muons traversing the MDT chamber and allows a rough track reconstruction, which is especially important to determine the coordinate not measured by the MDT chamber. It consists of two double layers of plastic scintillators. Every double layer contains 2×6 scintillators, each implying a scintillation volume of $105 \times 20 \times 2 \ cm^3$. Within each double layer the 2-dimensional position of an incident muon can be determined in an active trigger area of $110 \times 105 \ cm^2$, thanks to the special arrangement of the scintillators (see figure 4.6):

- Each pair of overlapping scintillators of a double layer are oriented with its photomultipliers oppositely. The time difference of the signals from such a pair of photomultipliers is therefore proportional to the position of the muon track along the scintillators.

- The 6 scintillators of one layer are shifted by half of their strip width to the 6 scintillators of the second layer with the opposite arrangement. In this way 11 instead of 6 overlaps are created in each double layer. The explicit identification of the overlap a muon was traversing is therefore the same as knowing the crossing position perpendicular to the scintillator length in steps of $10 \, cm$ with a standard deviation of $\frac{10 \, cm}{\sqrt{12}} \approx 2.9 \, cm$.

The Cosmic Trigger Logic

A block diagram illustrating the functional principle of the cosmic hodoscope is shown in figure 4.6. Every signal coming from one of the 24 photomultipliers of the 24 scintillators is actively splitted into two branches. With one branch time information for track reconstruction is collected and with the other branch the hardware trigger is formed. For the second purpose the signals from the 6 scintillators of a layer are merged with a logic OR. The arriving times of two such signals, which are belonging to opposite orientated and normally overlapping scintillators, is averaged by a mean timer[15]. Therefore the leading edge of the mean timer output signal corresponds to the time, which a "reference" muon, traversing always the middle of this scintillator pair's overlap, would introduce. Subsequently the coincidence of the two time averaged signals from the top and bottom double layers is build and used as hardware trigger.

The timing was adjusted with delays, in such a way that the signal from the bottom double layer came last, such that the trigger time was defined by the bottom hodoscope double layer. The hardware trigger was used in 5 different locations:

- to generate the ADC gate for the pulseheight measurement (see next section)

- as trigger input for the CSM-0 to record drift time data

- as injection signal for the additional mezzanine card to compensate for the $25 \, ns$ uncertainty (see section 4.4.3)
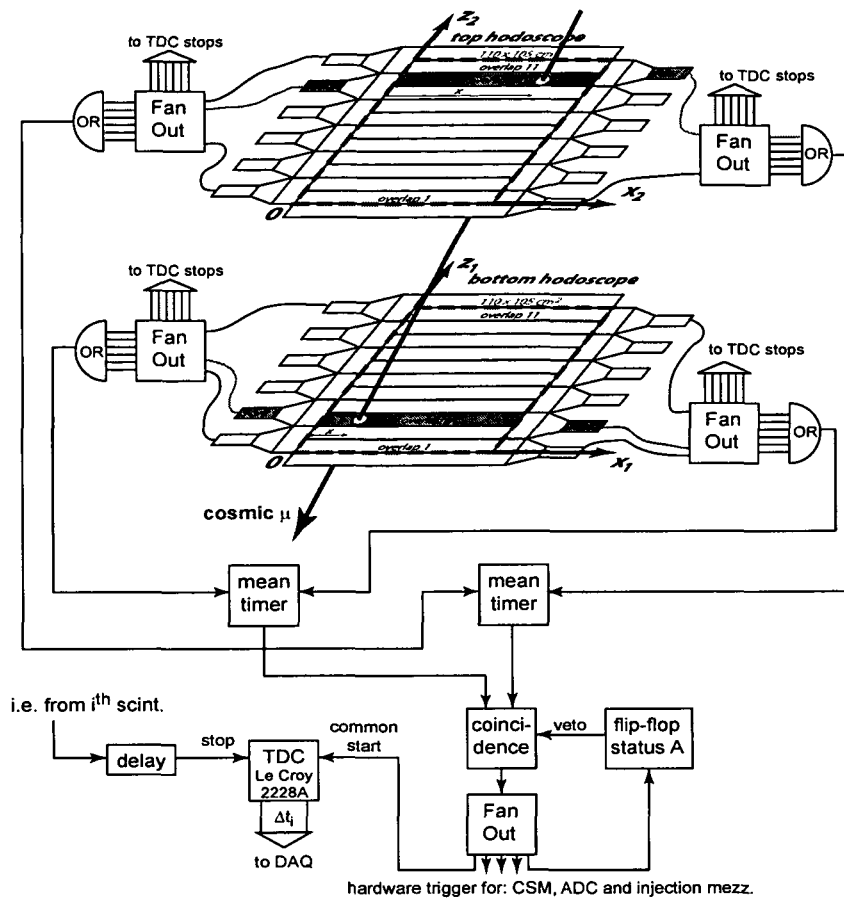
---

[15]Le Croy 6243

Figure 4.6: Block diagram of the cosmic trigger logic. The principle of the muon track reconstruction is illustrated by means of the 4 scintillators i, j, k, l generating photomultiplier signals, which are leading to the time measurements $\Delta t_i, \Delta t_j, \Delta t_k, \Delta t_l$ (see section 4.5.1).

- to set a flip-flop[16] which blocks further hardware triggers until the DAQ is ready and resets again this flip flop.

- as the common start signal for the TDC's[17] connected to the scintillator channels.

Hodoscope Multilayer Calibration

The counters of the 24 CAMAC TDC channels, which were started in common by the hardware trigger, were stopped individually by the delayed signals of the scintillators which have been branched off as mentioned before. The resulting digitised TDC values of the different arriving times of the scintillator hits in turn, allowed to determine the interaction coordinate x of the muon along the corresponding scintillator pair. The

---

[16]Status A Camac module

[17]3 TDC CAMAC modules: Le Croy 2228A, 50 ps time resolution

absolute point of time $t_{stop,i}$, at which the TDC counter of the ith scintiallator gets stopped, occurs after the reference time t_0 where the muon traversed a certain plane[18] due to the following delays:

$$t_{stop,i} = t_0 + \Delta t_{tof,i}(s) + \frac{\Delta x_i}{c^*} + \Delta t_{delay,i} \tag{4.1}$$

where $\Delta t_{tof,i}(s) = \frac{s}{c}$ is the time of flight the muon needs from the reference plain to the ith scintillator, Δx_i the light path the photons travel within the scintillator material with an effective light propagation speed c^* and $\Delta t_{delay,i}$ is the accumulated electronic and cable delay for this channel.

The measured TDC values Δt_i are the time differences between the arrival times of the stop signals and the common trigger t_{start}

$$\Delta t_i = t_{stop,i} - t_{start} \tag{4.2}$$

Since the time of flight delay is the same for two overlapping[19] scintillators i and j, building the difference of their TDC values

$$\Delta t_i - \Delta t_j = t_{stop,i} - t_{stop,j} = \frac{1}{c^*}(\underbrace{\Delta x_i}_{x} - \underbrace{\Delta x_j}_{l-x}) + (\Delta t_{delay,1} - \Delta t_{delay,2}) \tag{4.3}$$

allows to calculate the muon penetration position[20] x

$$x = [\Delta t_i - \Delta t_j - \underbrace{(\Delta t_{delay,i} - \Delta t_{delay,j})}_{A_{ij}}] \underbrace{\frac{c^*}{2}}_{\frac{l}{B_{ij}}} + \frac{l}{2} \tag{4.4}$$

if the overlap specific constants A_{ij} and B_{ij} are known. To determine these 22 constants two calibrations runs, each with only the hodoscope double layer to calibrate giving the coincidence, are taken. This procedure is done to remove any influence of the geometrical acceptance to the distributions. The constants are then obtained directly from histograms filled with the measured time differences $\Delta t_i - \Delta t_j$, where A_{ij} is nothing else as the center of this distribution and B_{ij} its width (see figure 4.7). Due to the intrinsic time resolution of the two scintillators forming the overlap[21], the edges of the ideal rectangular distribution are smeared out. Accordingly fits with Fermi-Functions of the form

$$f_\pm(t) = \frac{a}{1 + e^{\pm(b_\pm - t)/c}} + d \tag{4.5}$$

have been applied to determine the inflection points of the rising b_+ and falling edge b_- necessary to calculate the needed calibration constants

$$A_{ij} = \frac{b_+ + b_-}{2} \quad \text{and} \quad B_{ij} = b_- - b_+ \tag{4.6}$$

---

[18]for the following the bottom hodoscope layer is considered as reference plane
[19]with a overlapping length $l = 105\,cm$
[20]here measured from the readout side of the scintillator i
[21]the spatial resolution along the scintillator length was measured to be about $10\,cm$
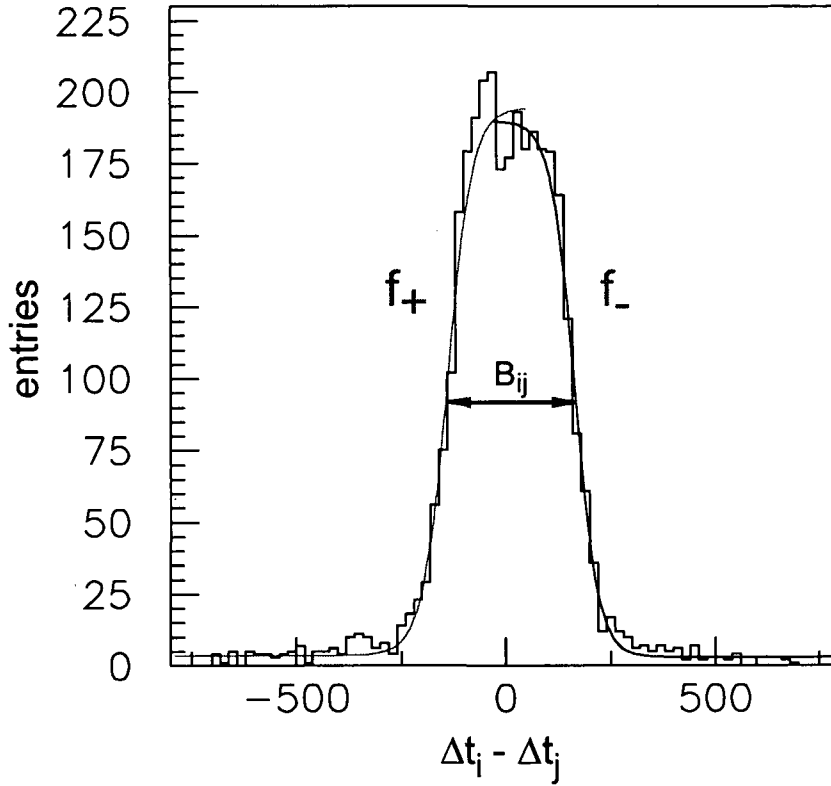
Figure 4.7: Typical distribution of time differences between the muon signals coming from overlapping scintillators

The half width $B_{ij}/2$ is equal to the photon propagation time needed for the full overlapping scintillator length, which was measured to be on average $7.3 \pm 0.2\,ns$. The difference with the naive value $t = \frac{l}{c^*} = \frac{nl}{c} = 5.25\,ns$, where $n = 1.5$ is the refraction index of the scintillator material, can be understood as discriminator effect: For triggering the discriminator also a significant amount of internally reflected and therefore delayed photons is required.

4.6   The ADC Readout Chain

The analog pulses of every third MDT is extracted with the help of the corresponding test output driver of the ASD-lite chip. As these LVDS driver outputs have to be terminated with an wave resistance of $100\,\Omega$ the impedance is converted with small transformers[22] to $50\,\Omega$ to be compatible to the CAMAC inputs. After the impedance conversion the analog signals are delayed with $80\,m$ coaxial cables to compensate for the time needed for the trigger signal generation. The trigger opens the gates of the CAMAC ADC's [23]

---

[22]the winding counts of the secondary and primary coil are in the ratio $\frac{N_2}{N_1} = \sqrt{\frac{Z_2}{Z_1}} = \frac{1}{\sqrt{2}}$

[23]eight LeCroy 2249W CAMAC modules, each 12 channels, range: 11 bit, gain: $0.25\,pC/count$

for $1\,\mu s$ in which the current of the muon signals are integrated and digitised.

4.7   Testbeam Setup for the High Rate Test at GIF

As already mentioned, a light, moveable structure with the BIS chamber mounted vertically, was in use during the testbeam period to facilitate rotation around the vertical chamber axis, needed for autocalibration (see figure 4.8). Almost 33 million events, corresponding to $14\,GByte$ of binary data, have been collected with testbeam muons. Drift time and pulseheight data with a set of incident angles under different background rates [24] have been taken as well as data runs with varying high voltage[25].
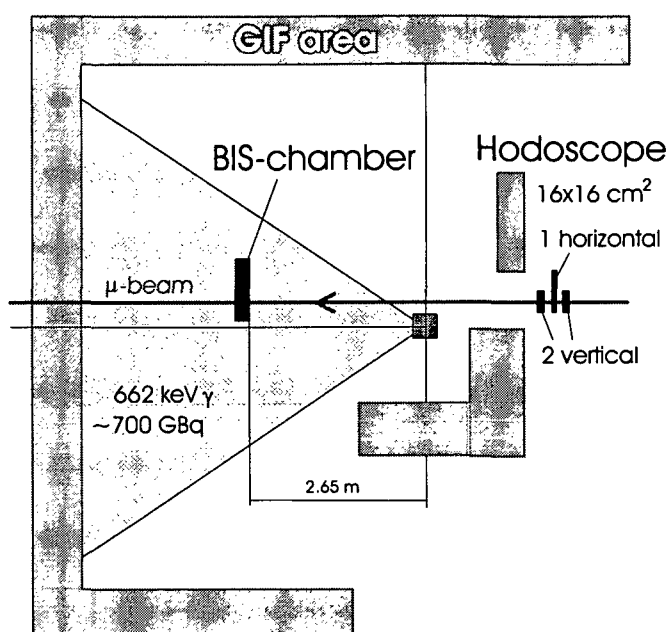
Figure 4.8: Vertical installation of the BIS MDT chamber during the testbeam period

The trigger for the muon beam was implemented as a coincidence of three plastic scintillators with a common overlap of $16 \times 16\,cm^2$ centered on the beam line (see figure 4.8). To gain a better time resolution[26] of the hardware trigger, the analogue scintillator photomultiplier signals were used with external constant fraction discriminators (CAEN CFD V812B) to minimise the time jitter of the discriminator threshold crossing[27]. The trigger setup was located upstream from the GIF radiation zone, separated by a concrete wall to avoid accidental coincidences, triggered by the high rate photon

---

[24] no γ source, $\sim 40\,kHz$, $\sim 70\,kHz$, $\sim 200\,kHz$ and $\sim 250\,kHz$ per tube

[25] $2880\,V$, $2980\,V$, $3080\,V$, $3180\,V$ and $3280\,V$,

[26] the time resolution of the testbeam trigger was around $2\,ns$

[27] An ideal constant fraction discriminator releases the trigger whenever the input signal exceeds a constant fraction of the signal peak height. This technique therefore compensates for the time jitter contribution resulting from different signal pulse heights

background coming from the gamma source. The recording of events triggered by cosmic muons penetrating the scintillators, have been suppressed at least in periods of no SPS spill extraction by vetoing arriving triggers between the two SPS control signals "End of Extraction" and "Warning Extraction".

The achieved DAQ rate during a SPS spill was ranging from $150\,Hz$ up to $450\,Hz$. The latter was reached in case of no gamma background, collecting no pulseheight data and applying only local data recording. Hang-ups of the DAQ due to a stuck CSM-0, as described in section 4.4.4, occurred for 0.4 % of the events.

Chapter 5

Ageing Studies

A crucial question for the ATLAS MUON collaboration is whether the MDT chambers will perform as requested over the whole operation period of 10 years. It is well-known that drift chambers exposed to a high radiation dose can suffer with time from deposits on the electrodes, resulting in a reduced drift field and therefore smaller gas gain, which in turn deteriorates the efficiency and spatial resolution of the detector. Because of the huge number of MDT's in the muon spectrometer and the high demand for positioning the anode wire accurately within a tube it is not foreseen to replace a single wire during the whole ATLAS era. Several tests have been undertaken in the past to find operation conditions and particulary a gas composition which meets the ageing requirements (sec. 3.1). The nonlinear baseline gas Ar-CO_2 (93:7) was found to show no ageing effects as well as being compatible with the performance criteria in a high rate environment (see chapter 2).

In the work presented in this chapter, for the first time a long term study with a standard MDT chamber, fully equipped with almost final front-end electronics, was performed. Moreover a circulated gas system (see chapter 3), similar to the one supposed to supply the MDT's in ATLAS, was operated for the first time and connected to one halve of the chamber to study possible influences of gas circulation on the ageing behaviour.

By running the ageing setup described in the previous chapter with interruptions and modifications (chapter 4.2) for over one year at the GIF area, an average charge of around $250\,mC/cm$ was collected by the drift tubes (sec. 5.1). This corresponds to 4 years of ATLAS in the conservative worst-case assumption or respectively to 10 years ATLAS applying a safety factor 2.

The pulseheight spectra from signals of cosmic muons detected by the individual tubes have been recorded in regular intervals and analyzed. For the MDT's of the multilayer supplied by the open gas system no ageing was observed (sec. 5.5), whereas the drift tubes connected to the prototype of the circulated gas system showed a local ageing effect (sec. 5.6). After analyzing the spectra with respect to the position along the tubes, the ageing effect was interpreted as a local pulseheight loss in the first $\approx 30\,cm$ from the gas-inlet side of the MDTs (sec. 5.7), which was cross-checked by further pulseheight measurements with a moveable gamma source (sec. 5.7.3). To understand

the source and cause of this local ageing phenomenon gas and surface analysis have been investigated (sec. 5.7.4). The surface analysis showed deposits in the form of a needle structure sticking out of the anode surface. As this structure was identified as silicon oxide polymerisation, which can not be produced in the pure detector gas, the setup was dismantled into its components to find the origin of the contamination. After systematic analysis of the cleanliness of different parts of the circulated gas system the source of the gas contamination could be located. Although a lot of effort was made to stay clear of any risk of contamination by unclean components, like standard rotameters, greased valves etc., a sealing compound made of silicone rubber has been found in the circulation loop (sec. 5.7.5) - a clear indication of how much attention must be paid in cleaning and mounting the parts of the MDT gas system to avoid ageing.

5.1 Accumulated Charge

Figure 5.1 shows the overall accumulated charge and its development during the different data taking periods as specified in chapter 4.2. The charge is calculated from the HV current measured continuously for each MDT multilayer. A slightly higher charge was collected from the tubes in multilayer one as it was in both setups closer to the γ-source and moreover shielding the second one.
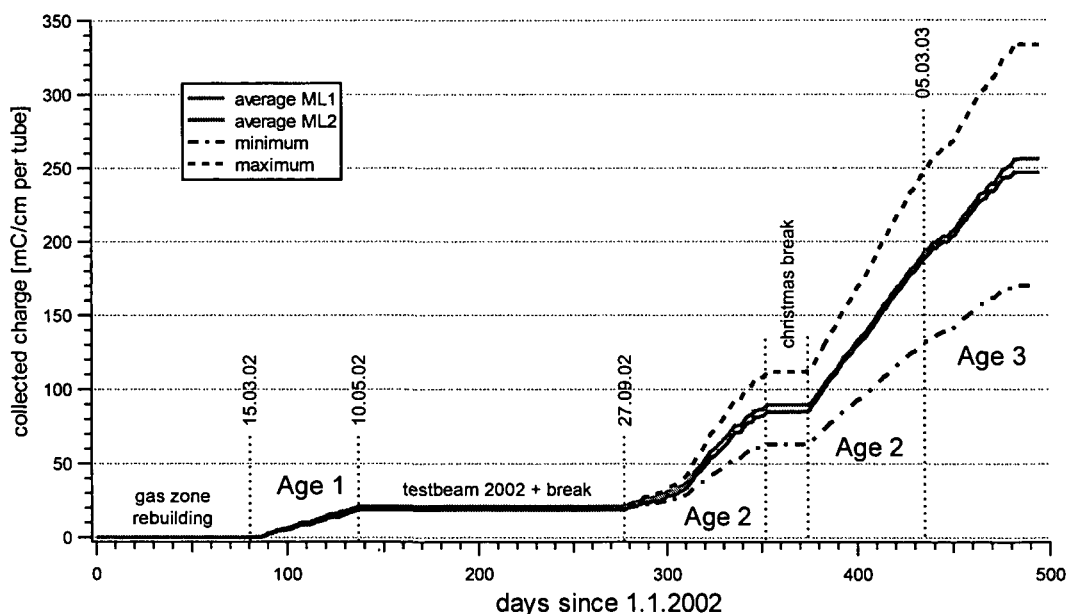
Figure 5.1: Accumulated charge per tube and centimeter tube length since 1.1.2002

A much larger geometry influence on the non-uniformity of irradiation originates from the orientation of the inclined mounting during "Age 2" (see figure 4.3). From measured γ-count rates[1] it is estimated that the tubes furthest from the caesium source, i.e. tubes

---

[1]measured gamma rates for tubes with ADC readout are indicated in figure 5.16 and 5.17.

on the right hand side of figure 5.2, see a factor 2 less irradiation than the tubes closest to the source. Taking this into account the development of estimated maximum and minimum accumulated charge is indicated by dashed lines in the same figure.

5.2 Reference Measurements with Cosmic Muons

Quantities which can be used to follow up and classify the ageing behaviour of drift tubes are count rates due to irradiation, the electrical current drawn per tube and the analysis of pulseheight spectra. The first two numbers could not be availed, because there was no possibility of measuring the individual currents and the gamma count rates of the tubes appeared not long-term stable enough, as changes in the arrangement of the setups in front of the MDT test stand influenced the γ-shielding behaviour. Besides pulseheight spectra measurements imply more meaningful information.
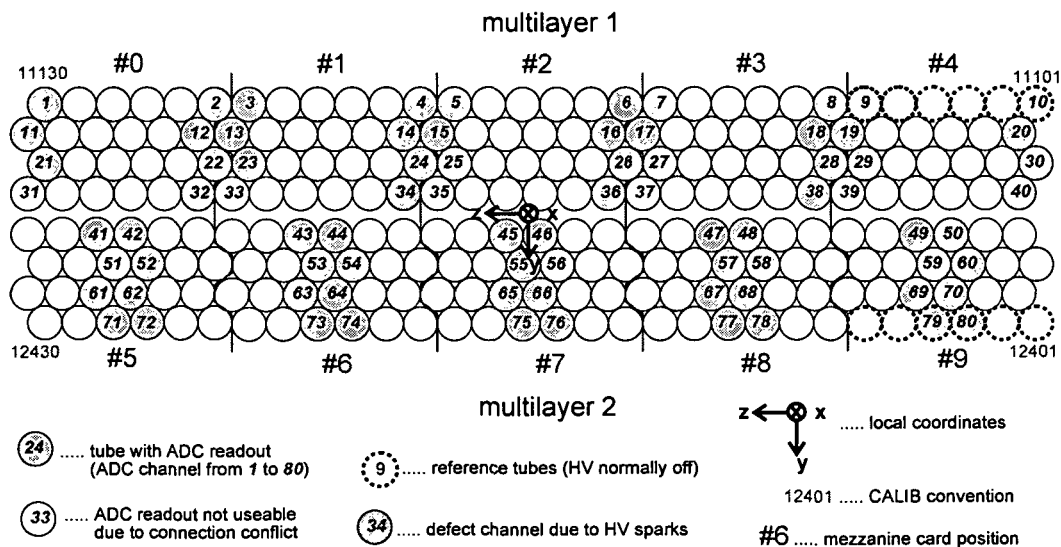
Figure 5.2: Cross section of the BIS MDT chamber with the numbering for the ADC channels as seen from the read-out side.

As already outlined in the description of the cosmic setup in section 4.5 events triggered by cosmic muons have been utilised to gain such pulseheight spectra. Weekly reference measurements with the GIF irradiation source switched off have been undertaken, also for the 12 tubes which have been switched off from HV during irradiation and are referred to as "reference tubes" (highlighted with a dashed outline in figure 5.2). These reference tubes allow to separate any acquired ageing effect from changes to the pulseheight effecting the chamber globally, as e.g. induced by changes in temperature. On average 500 000 events have been collected during 260 minutes per reference run, which leads to a mean trigger rate of about $32\,Hz$.

Figure 5.2 shows the cross section of the 240 drift tubes of the BIS chamber with the tubes usable for pulseheight readout numbered from 1 to 80 (see also sec. 4.4.2). Due to plug

conflicts on the mezzanine cards from multilayer 1 and one defect channel the number of ADC readout channels was further reduced to 74. For this chapter the numbering of figure 5.2 is used, whereas in the next chapter the so called CALIB[2] numbering convention for the whole chamber is used, where a tube ID is calculated as[3]:

$$tubeID = 10\,000 + multilayer * 1000 + layer * 100 + tube$$

$$(5.1)$$

with the tube numbers starting from 1. Besides of the ADC reading, i.e. integrated charge over a gate of $1\,\mu s$ for the 74 tubes with ADC readout, the data of an event in a reference run consists of the drift time information from the AMT's for all the tubes and the scintillator timing info needed for track reconstruction (see also section 4.5). The local chamber coordinate system used for track reconstruction is also shown in figure 5.2, with the origin located in the center of the chamber.

5.3   Analysis of Pulseheight Spectra

For a fixed gas gain the integrated charge of a muon signal is proportional to the number of primary electrons and thus proportional to the energy the muon looses during traversing the detector gas. The mean energy loss per path length due to gas ionisation is described by the Bethe-Bloch formula (see section 2.1.1). Statistical fluctuations in the number of collisions an individual muon suffers and fluctuations in the energy it transfers in each collision results in fluctuations in dE/dx. For the case of thin absorbers and gases, where only a small number of collisions take place, the distribution of dE/dx was theoretically derived by Landau [62]. His energy loss distribution is expressed as

$$\Phi(\Delta E; \xi) = \frac{1}{\xi\,\pi} \int_0^\infty e^{-u\,lnu - u\lambda(\Delta E;\xi)}\, sin(\pi u)\, du \qquad (5.2)$$

with

$$\lambda(\Delta E; \xi) = \frac{\Delta E - p(\xi)}{\xi} \qquad (5.3)$$

where ξ is the width of the distribution[4] and $p(\xi)$ is proportional to the most probable value. The long tail of to the high energy side of the distribution, which is describing the hard-collision losses from δ-electrons, is assumed to extend to infinity in Landau's theory. This unphysical assumption results in an undefined mean value of this distribution, depending on the applied high energy cut for building the mean. Therefore the most probable value is normally utilised as function parameter.

As the Landau distribution can not be represented in an analytic form either numerical approximations or the analytical Moyal-approximation

$$\Phi(\Delta E; \xi) \propto exp\left[-\tfrac{1}{2}(\lambda(\Delta E; \xi)) + e^{-\lambda(\Delta E;\xi)} \right] \qquad (5.4)$$

---

[2]a software package for MDT autocalibration studies [61]

[3]the tube ID's of the four corner tubes are labelled in 5.2

[4]which is depending on the absorber material (density ρ, atomic number Z, nuclear number A), on the path length Δx and on the velocity β of the muon [64]: $\xi \propto \frac{\rho Z x}{A\beta^2}$

are used to fit energy loss spectra with Landau characteristic. Pulseheight spectra taken during the test beam with muons of a defined energy of $100\,GeV$ and filled for muon hits with a certain ionisation path length $\Delta x = 2\sqrt{b^2 - r^2(t_{meas})}$, show the Landau-distribution characteristic – hence applied fits with functions like equation (5.4) converge well. Taking into account the energy distribution of cosmic muons and particulary the distribution of the different path lengths due to different angles of incidence for an overall cosmic MDT pulseheight spectrum, the Landau distribution gets smeared out (see figure 5.3). Especially the normally sharp rise on the low energy side of the Landau-distribution gets smeared out to lower ADC values as small ionising drift paths of tracks near the tube wall contribute. To keep the capability of performing Landau-fits to the overall cosmic spectra, an ionisation path length correction to the measured pulse charges can be applied on an event-by-event basis, by calculating the effective path length, which needs both: the drift time information t_{meas} and the reconstructed incident angle of the muon with respect to the drift tube gained with the hodoscope data [63]. Here another approach was chosen:
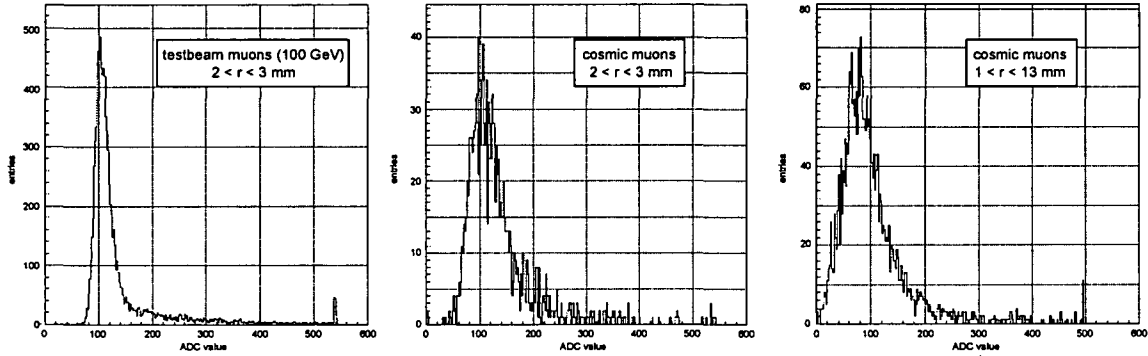
Figure 5.3: Contributions to the cosmic pulseheight spectra; *left:* Spectrum with testbeam muons crossing in a certain radius interval; *middle:* The same drift radius cut for cosmic muons, implying the contribution of the energy distribution of cosmic muons and the path length variation due to different angles of incident; *right:* Overall cosmic spectrum, the contributions of muons with small drift lengths, traversing the tube close to the cathode wall, populate the spectrum at small values

To allow for the mentioned additional contributions of the cosmic spectra, a 4-parameter fit function as convolution of a Landau distribution with a Gaussian was applied to the spectra (see figure 5.4):

$$\Phi_{conv}(\Delta E; m, \xi, \sigma, A) = A \int \Phi_{lan}(v; m, \xi)\ \Phi_{gauss}(\Delta E; v, \sigma)\, dv \qquad (5.5)$$

where $\Phi_{gauss}(x; \mu, \sigma)$ is the normalised Gaussian distribution with the mean μ and the standard deviation σ and $\Phi_{lan}(x; m, \xi)$ the normalised Landau distribution[5] according

---

[5]A numerical approximation in form of the CERNLIB routine "G110 denlan" was implemented. The convolution was done as numerical integral with the integral limits set to $\Delta E \pm 5\sigma$

to equation (5.3), but with the most probable value m as free parameter. The fourth parameter A is therefore the area of the convoluted distribution Φ_{conv} and acts as normalisation constant. For the following studies the most probable value m of the Landau distribution was the number used for analysis, but corrected with the actual electronic pedestal of the ADC channel. These ADC pedestals, resulting from baseline integration charges of the ADC's, were Gaussian distributed and therefore quantified with Gaussian fits. The mean values, used as the mentioned correction value, of this fits have been determined for every individual reference run, as they varied appreciable over time (see figure 5.5)
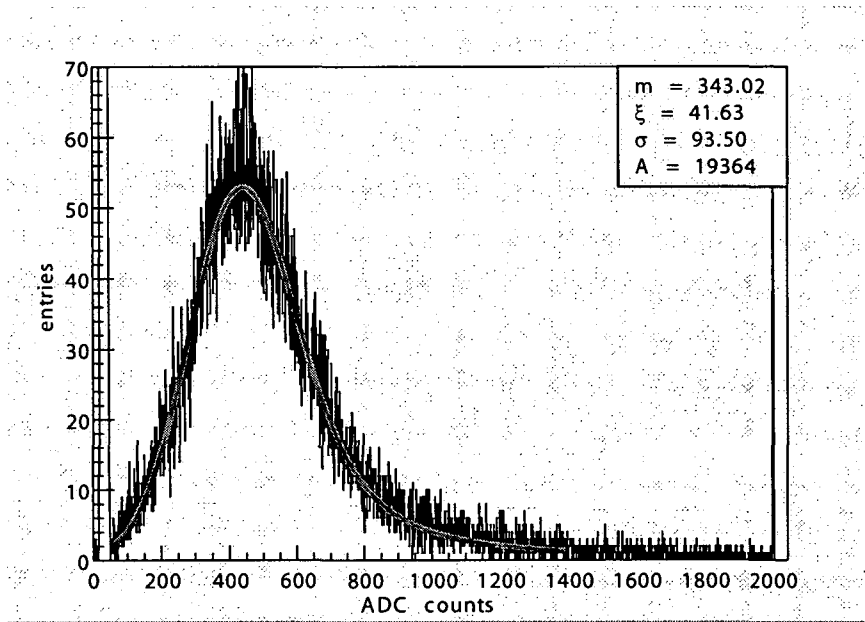
Figure 5.4: Fitting of the raw reference cosmic spectra with the Gauss-Landau convoluted 4-parameter distribution (equ. 5.5). The two almost vertical lines on the left side of the histogram are the edges of the huge pedestal.
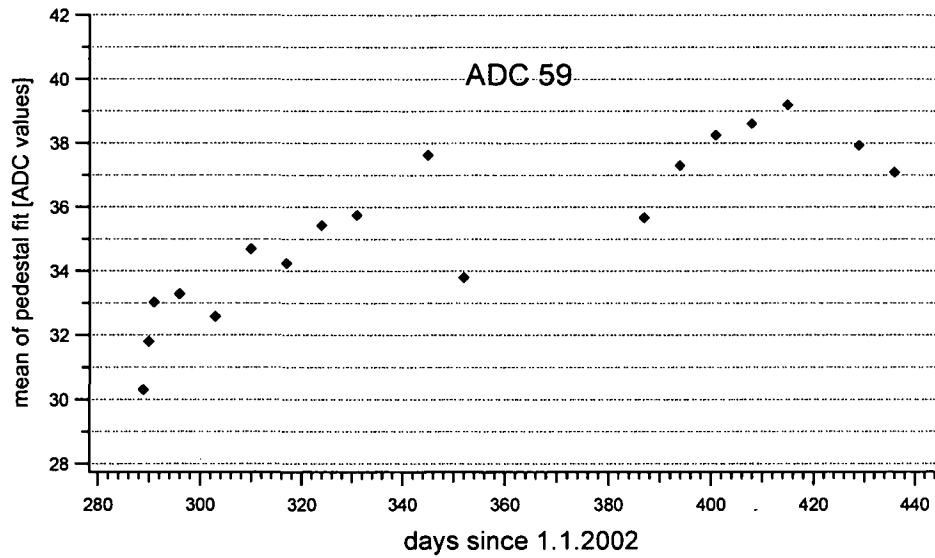
Figure 5.5: Variation of the pedestal values of an ADC channel over different reference runs.

5.4 Dependencies of the Pulseheight Spectra

5.4.1 Temperature

In the course of the ageing test the temperature of the chamber in different reference runs varied between 15 and 22 ^{o}C, monitored with ten PT-100 sensors glued to the MDT's. The temperature of the drift gas influences the pulseheight spectra (see figure 5.6) as the gas gain G increases with reduced gas density ρ according to Diethorn's formula [65]

$$G = \left[\frac{V \, \rho_0}{a \, ln\frac{b}{a} \, E_{min}(\rho_0) \, \rho} \right]^{\frac{V}{ln\, b/a} \frac{ln2}{\Delta V}} \tag{5.6}$$

where V is the high voltage, a and b the anode and inner tube radius, ρ_0 the gas density at $1\, bar$ and $20\,^{o}C$ and E_{min} and ΔV the so called Diethorn's parameters[6]. For an ideal gas[7] under isobaric conditions the gas density is inverse proportional to the temperature, hence comparing the gas gains with the help of (5.6) at two different temperatures T and $T + \Delta T$ gives

$$\frac{G(T + \Delta T)}{G(T)} = \left[1 + \frac{\Delta T}{T} \right]^{\frac{V}{ln\, b/a} \frac{ln2}{\Delta V}} \tag{5.7}$$

---

[6]The parameter E_{min} stands for the electrical field at the start of the avalanche and ΔV for the ionisation potential of the drift gas.

[7]for an ideal gas applies $pV = nRT$ (p...pressure, V...volume, T...temperature, n...amount of substance, R...ideal gas constant) which gives $p \propto \rho T$ when dividing the volume
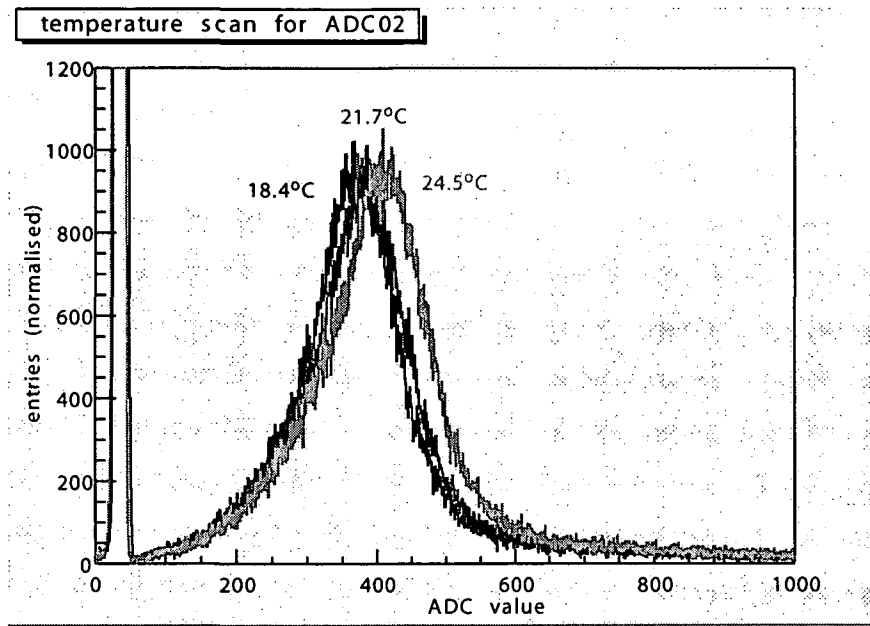
Figure 5.6: Influence of the temperature on the ADC spectra illustrated for testbeam data at nominal HV

Assuming nominal high voltage ($V = 3080\,V$) and a Diethorn's parameter[8] $\Delta V = 34\,V$, with (5.7) a relative gas gain increase of $3.4\,\%$ *per* $^\circ C$ is obtained at $20\,^\circ C$. The temperature correction value used in the presented work was gained by fitting pulseheight spectra of test beam runs with different average temperature (figure 5.6). The development of the peak position[9] of such fits over the averaged temperature is illustrated for three different ADC's in figure 5.7. Linear approximation to this data, normalised to the calculated peaks at $20\,^\circ C$, gives an average slope C_T of $\approx 2\%$ gas gain increase per $^\circ C$, which was applied as temperature correction in the form

$$P_{cor}(20^\circ C) = \frac{P_{meas}(T)}{1 + (T - T_{20^\circ C})\, C_T} \tag{5.8}$$

to the ADC spectra peaks $P_{meas}(T)$.

5.4.2   High Voltage

As seen from the spectra in figure 5.8 taken with testbeam muons, the gas gain is significantly dependent on the applied high voltage. Linear fits to the relative peak variation showed a sensitivity of $0.4\,\%/V$ (see figure 5.9). This value is estimated to be also the contribution to the peak long-term stability due to high voltage variations, as the high voltage was calibrated before each ageing reference run with a precision voltage divider and a voltmeter to a precision of about $1\,V$.

---

[8] measured for Ar-CO_2 (93:7) in [23]
[9] corrected for the pedestal value
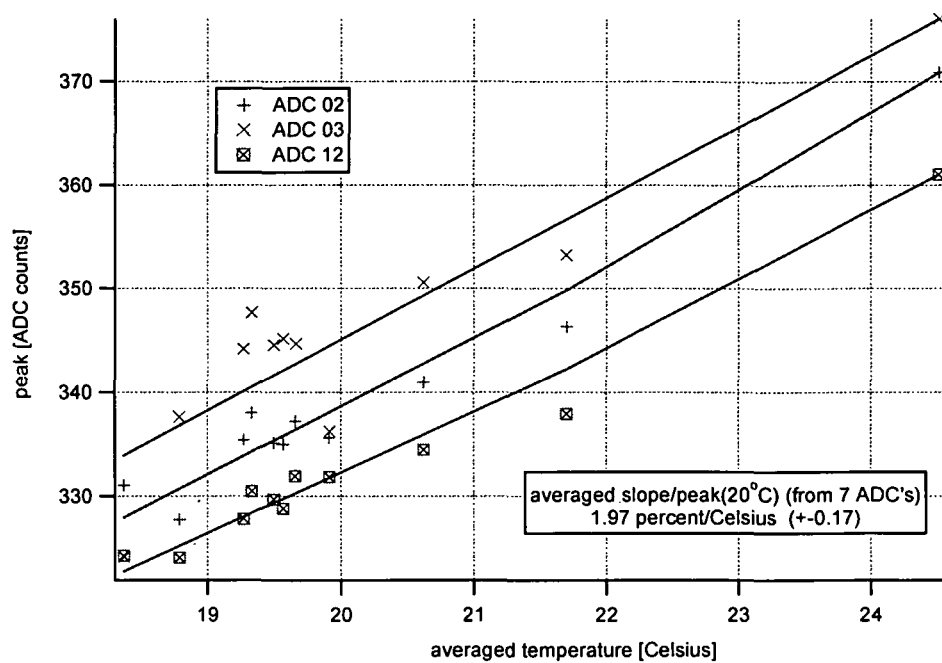
Figure 5.7: Dependence of the peak position of collected pulse height spectra from the gas temperature. The shown data originate from testbeam runs to obtain a temperature correction value for the ageing test
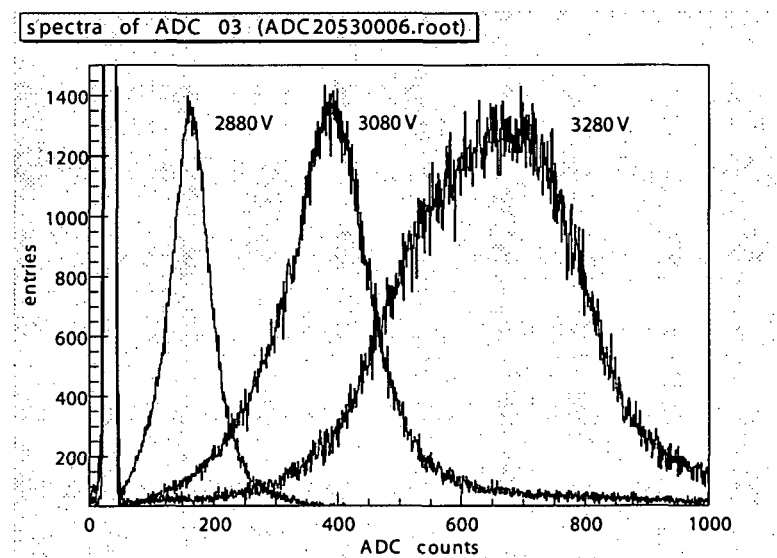
Figure 5.8: Pulseheight spectra dependence on the high voltage, shown for testbeam muons.
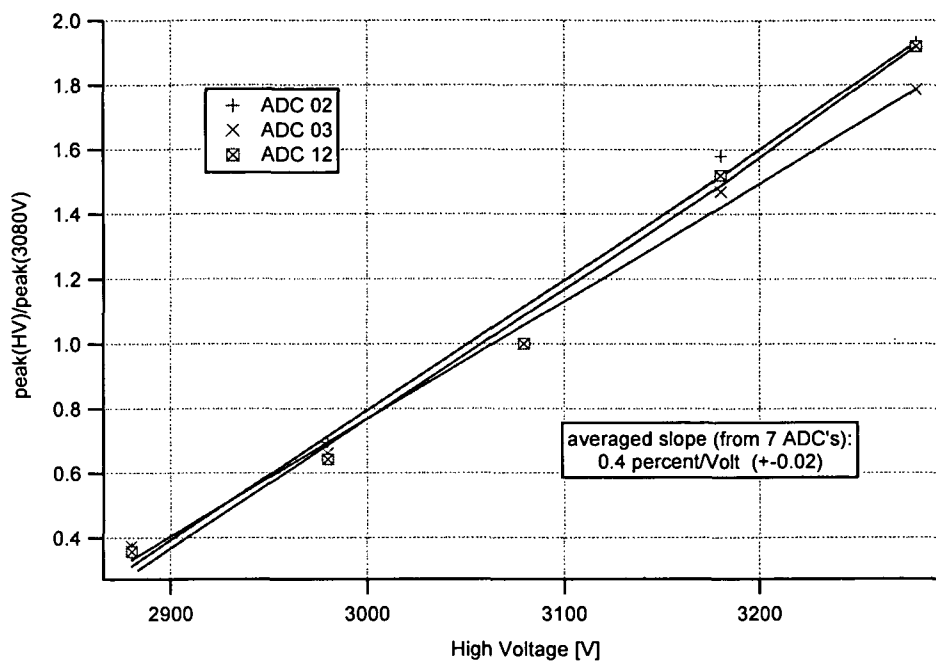
Figure 5.9: Variation of the relative peak position with the applied high voltage for ADC spectra taken with testbeam muons

5.5 Open Gas System

The peak development of Landau-Gauss convoluted fits, according to equation (5.5) and applied to the pulseheight spectra of the ADC's connected to the MDT's supplied by the open gas system (multilayer 2), showed no pulseheight degradation within the measurement accuracy for all the 38 channels. The accuracy is estimated to be around 5 %, according to the stability of data runs before starting the irradiation periods.

Figure 5.10 shows a peak development for an individual ADC channel from multilayer 2 and illustrates the influence of the temperature correction. The corrected plot shows still a small correlation to the temperature, which is an indication that the temperature effect is probably not fully compensated.

By building the ratio of the peak of the tube under study with the peak from the spectra of the reference tube no temperature correction must be applied. The development of such a ratio (figure 5.11) shows less fluctuation ($\approx$ 2 %) as the peaks gained by temperature correction ($\approx$ 4 %).
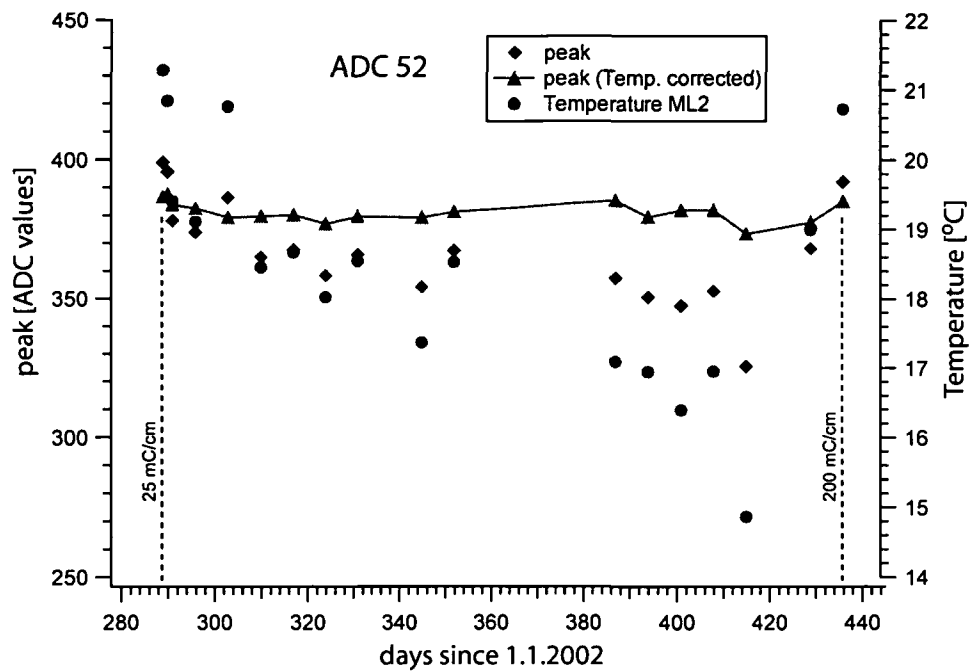
Figure 5.10: ADC peak development of a single channel of a MDT of the open gas system. The connected points belong to the temperature corrected values. The temperature is shown in the same plot with the ordinate on the right hand side
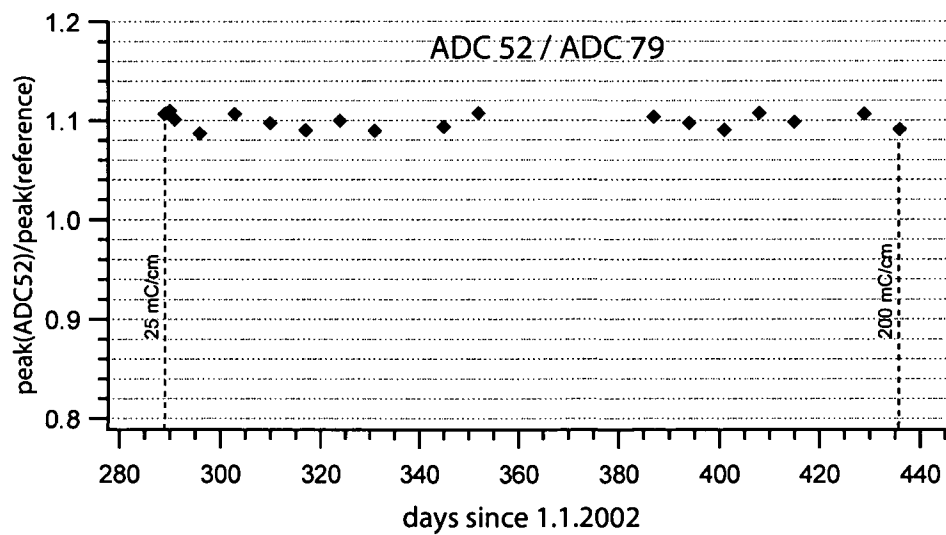
Figure 5.11: Time-dependency of the peak ratio between the tube under study and the reference tube

5.6 Circulating Gas System

The analysis method applied to the pulseheight spectra of the tubes belonging to the open gas system, as described in the last section, could not be performed to reference data of the circulated multilayer, because progressive distortions of the ADC spectra occurred in the course of the ageing test. Out of the 28 useable read out tubes[10] the cumulative spectra of six tubes (ADC channel 5, 6, 7, 26, 17 and 20) showed a clear second peak to the left of the main peak, which appeared gradually with time, whereas the remaining 23 tubes showed a more or less pronounced shoulder in their pulseheight spectra in the end of ageing period 2. The monthly development of the pulseheight spectra is illustrated in figure 5.12 for a tube showing the double peak structure. The secondary peak was understood to originate from a region along the tube where the gas gain was reduced due to a local ageing effect. The analysis and clarification of this ageing effect is presented in the next section.
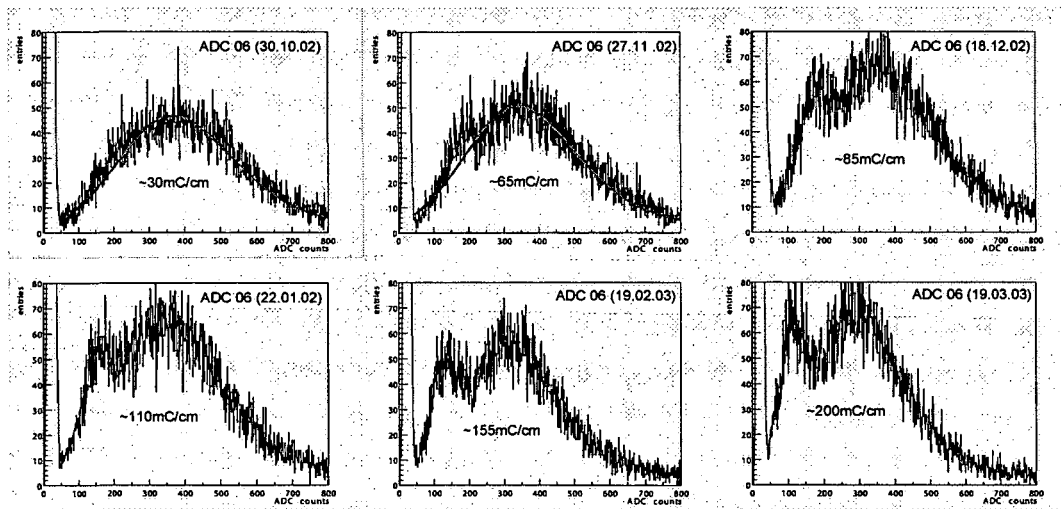
Figure 5.12: ADC spectrum development for a tube supplied by the circulated gas system. A clear second peak occurred gradually with time for this tube. Earlier spectra from ageing period 1 are not shown here since for this period the area suffering from the ageing effect was not covered by the trigger acceptance and therefore the spectrum shapes for all tubes from this period showed no sign of a second peak or shoulder phenomenon.

---

[10]ADC channel 31, 33, 35, 37 and 39 had not been connected due to a space conflict on the mezzanine card, 34 and 36 were defect, channel 1, 11 and 21 had very low statistic as the tubes were located at the edge of the hodoscope trigger acceptance and channel 9 and 10 belonged to the reference tubes

5.7   Analysis of the Local Ageing Effect

5.7.1   Reconstruction of the Second Coordinate

To be able to separate the pulseheight data for different regions along the tube, the coordinate along the tube length had to be reconstructed event-by-event with the help of the hodoscope timing information. In a first step the crossing points of the cosmic muon with the top and bottom hodoscope double layers were determined according to the method described in section 4.5.1 in their local coordinate system (see figure 5.13).
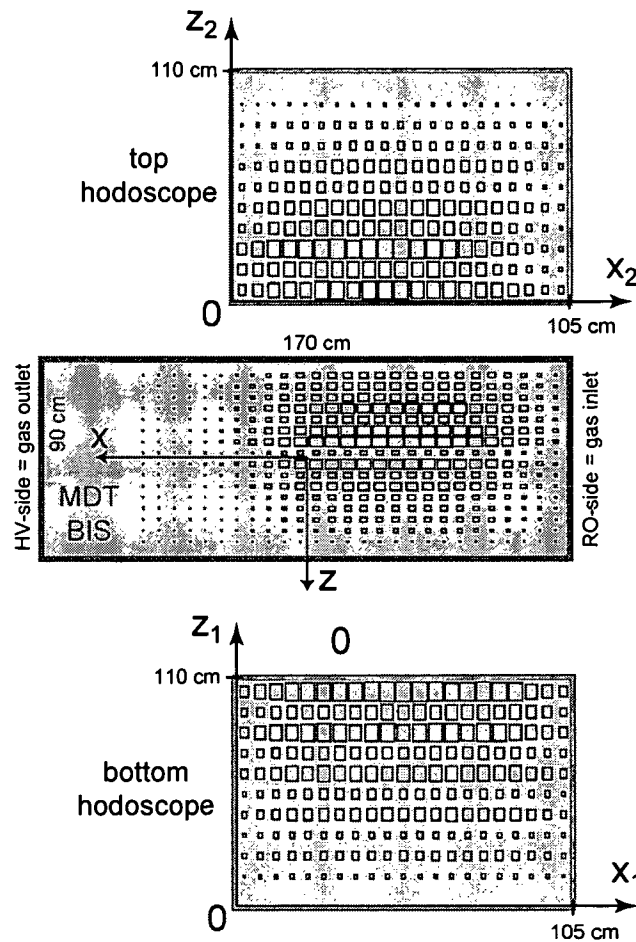
Figure 5.13: 2-dimensional distribution of the measured crossing points of cosmic muon tracks with the top and bottom hodoscope shown in their local coordinate system. The area of the drawn boxes is proportional to the number of registered hits found in the individual segments of $5\,cm \times 10\,cm$. The middle part shows the distribution of the reconstructed intersection points with the middle plane of the MDT chamber, calculated for the setup of ageing period 2.

To gain a precision of around $10\,cm$ in the coordinate along the scintillator length (referred to as x-axis, of the local coordinate system) the hodoscope was calibrated monthly

with the procedure explained also in section 4.5.1. From the two determined crossing points of the muon with the two hodoscope double layers, converted to global coordinates $\vec{a}$ and $\vec{b}$, the points of intersection of the reconstructed muon track with the middle planes of each of the 8 MDT layers were calculated with

$$\vec{x}_i = \vec{b} + \frac{\vec{n_i}^2 - \vec{b} \cdot \vec{n_i}}{(\vec{a} - \vec{b}) \cdot \vec{n_i}}(\vec{a} - \vec{b}) \tag{5.9}$$

where $\vec{n_i}$ are the normal vectors of the middle planes, pointing from the origin of the global coordinate system to the corresponding plane. The reconstructed muon tracks for a bunch of events is shown in figure 5.14 for the setup configuration during aging period 2.
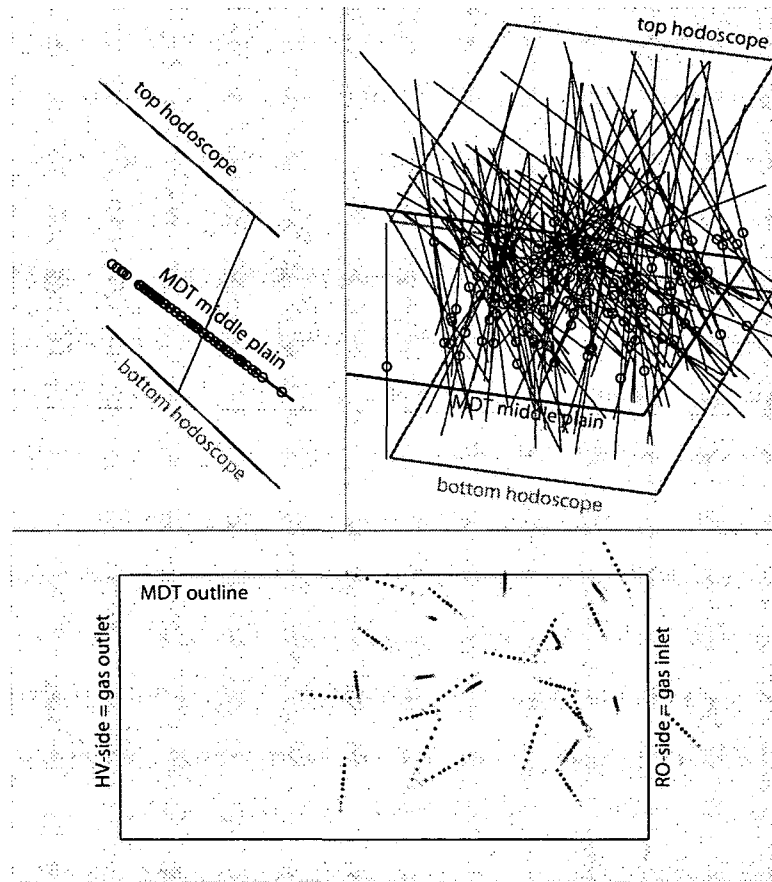
Figure 5.14: *top:* side-view (seen from Hv-side) of one reconstructed muon track (*left*) respectively a normal projection of the first 150 muon tracks (*right*) of a reference run during ageing period 2. *bottom:* Penetration points of 30 muon tracks with the middle planes of the 8 MDT layers and with the symmetry plane of the MDT, seen in the local 2-dimensional coordinate system of the MDT.

5.7.2 Local Pulse Height Loss

With the help of second coordinate information the pulseheight spectra could be separated for slices along the tube length. The top plots of figure 5.15 show such correlations between ADC values and track position along the tube for a tube which showed pronounced local ageing (*left*) and a reference tube (*right*). In this 2-dimensional representation the area of the boxes corresponds to the number of entries in the corresponding histogram bin. The abscissae of the plots coincide with the local x-axis of the chosen MDT coordinate system. The region between -85 and $-75\,cm$ corresponds therefore to the first 10 centimeters of the chamber seen from the gas inlet side (compare with figure 5.13). One can see that the most likely ADC value decreases close to the gas inlet side of the chamber. The plots beneath are profile histograms of the same data, i.e. they show the mean value of the ADC values in dependence of the position along the tube. Although the profile plots are more easily read compared to the 2-dimensional plots they are also easily biased at the few percent level by outlying measurements.
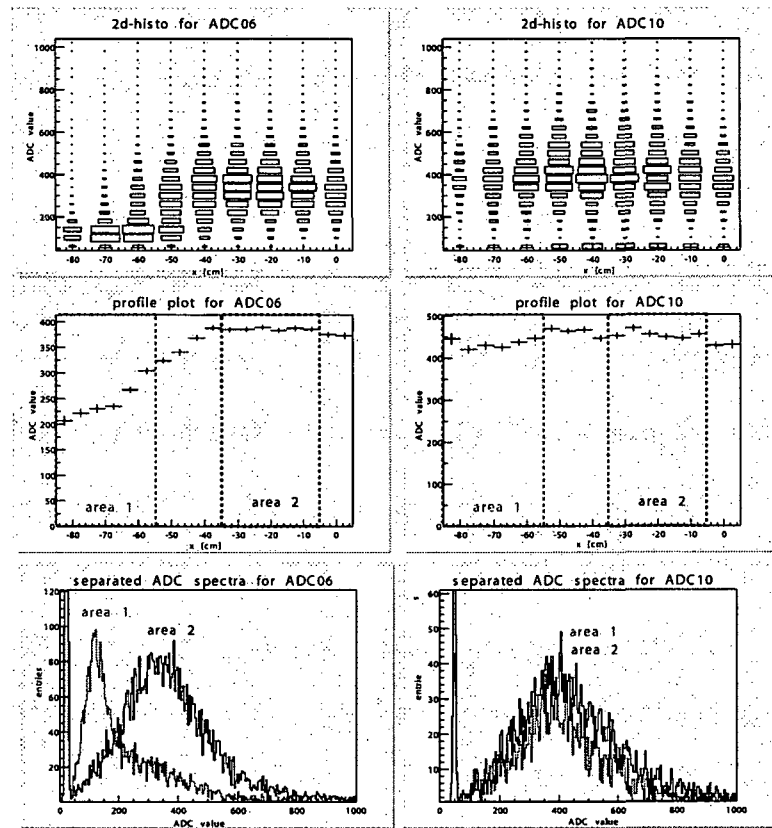
Figure 5.15: *top:* 2-dimensional histogram of the correlation between ADC values and track position along the tube; *middle:* profile plots of ADC mean values of slices along the tube length; *bottom:* pulseheight spectra separated for the two marked areas (see text for more details)

In the bottom plots of figure 5.15 the pulseheight spectra are separated for the aged area of the first 30 centimeters $(x = -85 \ldots -55\,cm)$ and a reference area $(x = -35 \ldots -5\,cm)$,

referred to as area 1 and area 2. To obtain a representative value of the local ageing effect which can be followed up for all the recorded tubes of multilayer 1 over time the following two numbers have been used:

- Landau-Gauss convoluted fits have been performed to the two separated pulse-height spectra, like the one shown in the bottom histograms of figure 5.15. The ratio

$$R_1 = \frac{mpv(area1\,spectra)}{mpv(area2\,spectra)} \tag{5.10}$$

between the most probable value of the fit of the spectra with area1-data and to the most probable value of the area 2 spectra was build and is referred to in the following as local ageing ratio 1. This ratio could be determined only for a few channels, which had enough entries for convenient fits.

- A number obtained also for the major part of the channels which had lower statistic was calculated by comparing the mean value of the profile plot (middle plots of figure 5.15) of the aged area 1 to the mean value of the reference area 2

$$R_2 = \frac{mean(area1)}{mean(area2)} \tag{5.11}$$

The comparison of the local ageing ratio R_2 at the beginning and end of ageing period 2 is illustrated for the tubes of the circulated multilayer in figure 5.16. The plot shows that all of the tubes had been already locally aged in September 2002 (accumulated charge of around $20\,mC/cm$), whereas the reference tubes (ADC channel 9 and 10) showed no degradation. Unfortunately it was not possible to study the developing during the initial phase of the ageing effect as the regarding chamber area was not in the trigger acceptance of the setup in period 1 (see figure 4.2).

No correlation of the local pulseheight degradation to the specific irradiation of the tubes could be observed, as can be seen from the individual gamma rate indicated additionally in figure 5.16. Instead differences in the strength of the local ageing phenomenon among different layers can be noticed. The effect seems to be more strongly pronounced in layer 1 and 2 as in layer 3 and 4. The only known difference in the construction and treatment of the layers is the gas supply of the tubes with so called tublets of different length and inner diameter[11]. This could lead to different gas flows between different layers and to different filtering behaviour of the tublets to the substance causing the ageing. Nothing of this was validated as the flow impedance of the 3 types of tubelets have been measured[12] to be within $10\,\%$ on the same level. Moreover no deposits of silicon-based substances, which have been found on the anode wire and identified to be responsible for the observed ageing (see section 5.7.4), have been detected on opened tublets of different layers.

---

[11]The brass tublets of the different layers had the following inner diameter and length: layer 1 + 2 $(1.1\,mm \times 53\,mm)$, layer 3 $(1.3\,mm \times 104.4\,mm)$ and layer 4 $(1.4\,mm \times 140.4\,mm)$

[12]by recording the pressure drop decay of a test volume, which lost gas through the tublet under study.
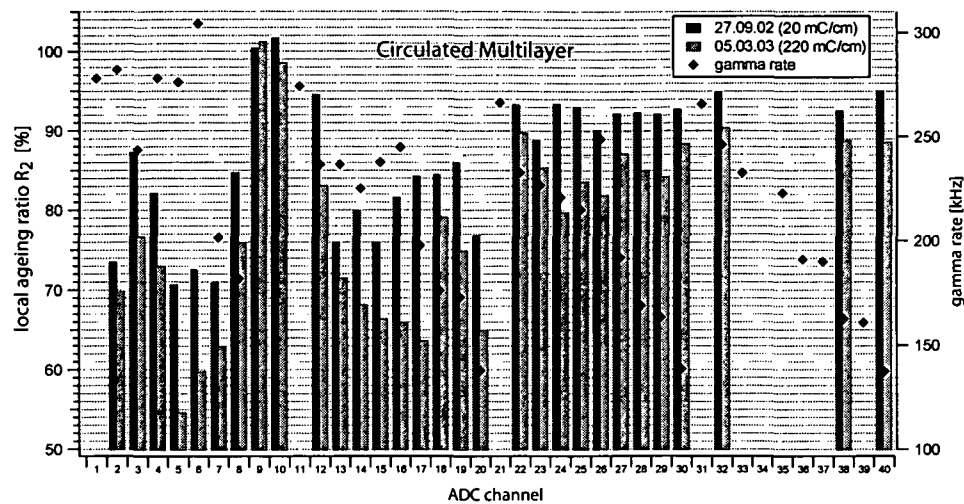
Figure 5.16: Local ageing ratio R_2 at the beginning and end of ageing period 2 for the tubes of multilayer 1. The gamma rate the corresponding tubes measured are drawn in the same plot with the ordinate on the right-hand side.

The precision of the applied method can be estimated by observing the local ageing ratio R_2 results for the multilayer 1 (figure 5.17) were no aging was observed.
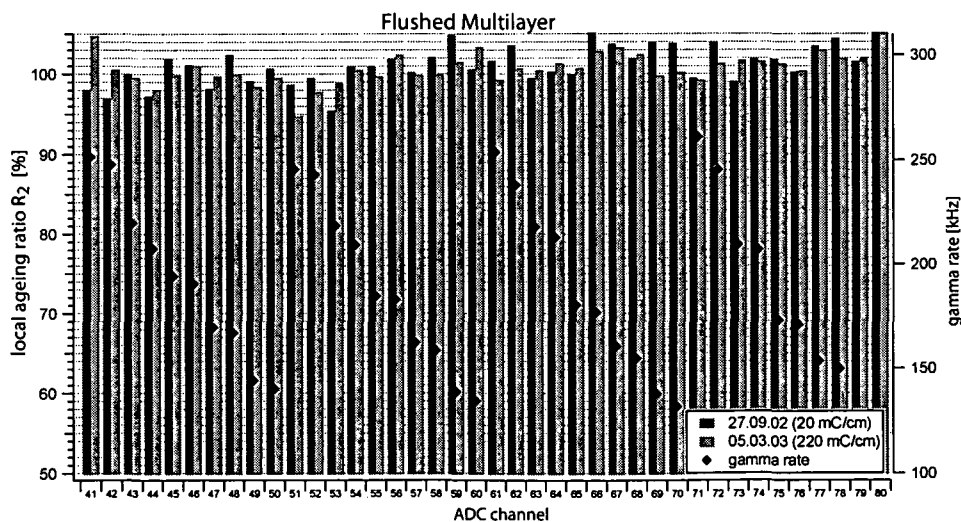

Figure 5.17: Local ageing ratio for the tubes of the multilayer connected to the open gas system at the beginning and end of ageing period 2. The gamma rates seen by the individual tubes are again indicated.

The deviation of the two different defined local ageing ratios R_1 and R_2 is illustrated in figure 5.18 by means of the time development of these values for one tube. Whereas the peak according to the applied Landau-Gauss convoluted fits is attenuated to only 40 %,

the ratio calculated by the means stays above 60 %. This is because the mean value of the ADC values within area 1 is affected crucial by the long tail of the spectra (compare to the separated spectra shown in figure 5.15). Nevertheless both numbers show similar trends. The development of the local ageing ratio R_2 for a tube of multilayer 2 and of a reference tube can be seen in figure 5.19, where no degradation was observed.
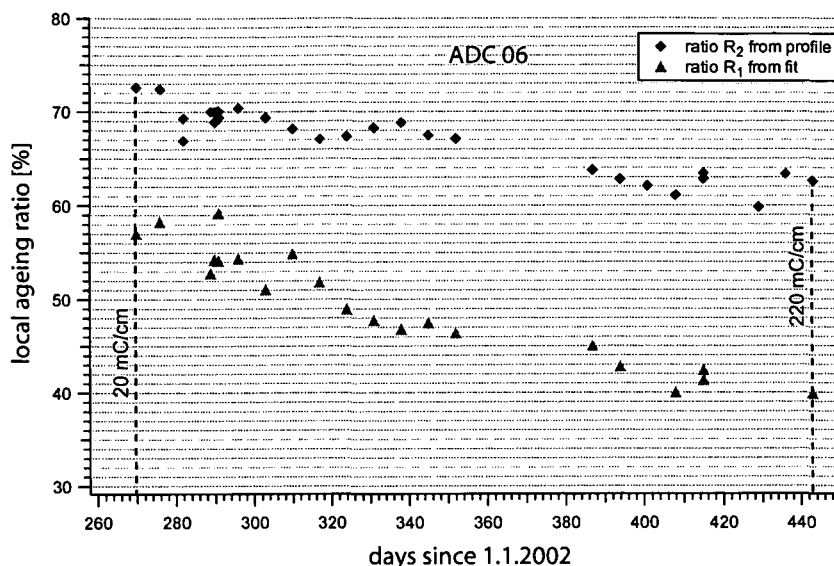

Figure 5.18: Comparison of the two determined local ageing ratios with time for an aged tube of multilayer 1
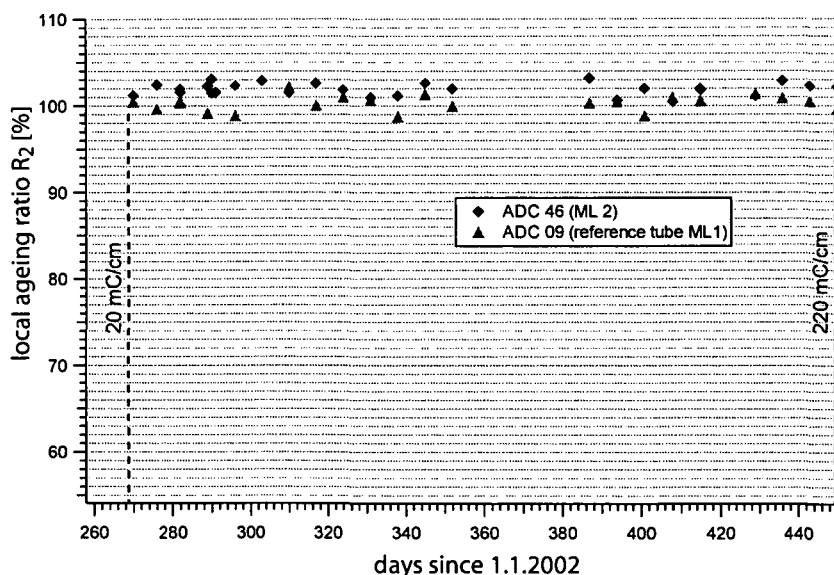
Figure 5.19: Local ageing ratio R_2 with time for a reference tube and a tube from the non-aged multilayer 2

5.7.3 Cross Check with a moveable γ-Source

To exclude that the discovered effect was obtained just because of a wrong reconstruction of the second coordinate, due to a wrong calibration, geometry description or a wrong track reconstruction algorithm, a direct pulseheight measurement with a γ-source was performed. For this the DAQ was modified in such a way as to allow triggering on a MDT signal itself for one tube at a time.
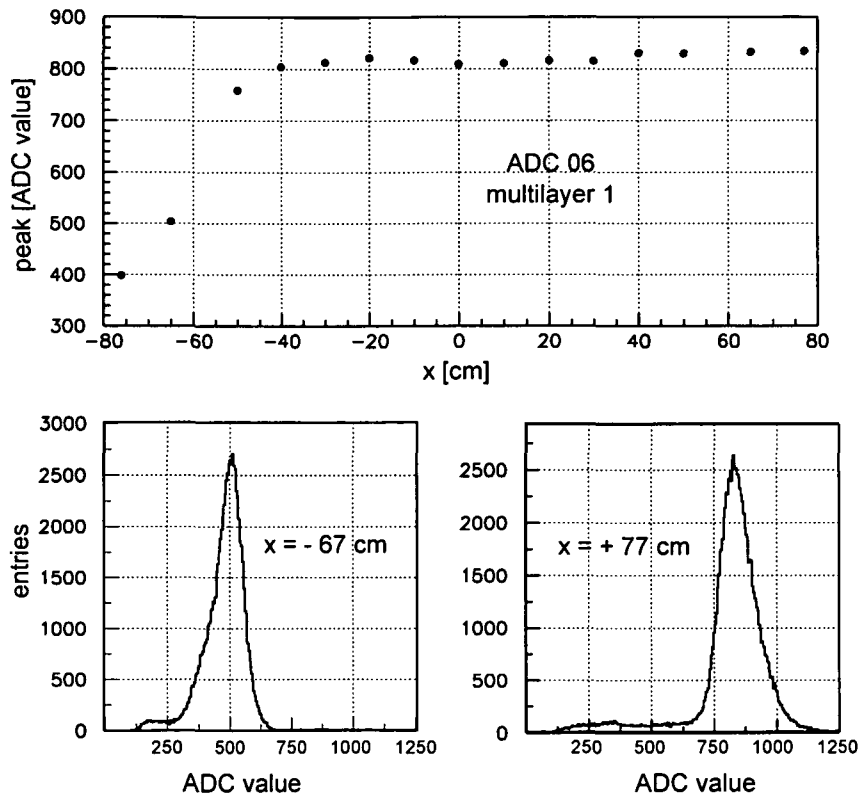

Figure 5.20: *bottom:* Recorded Cd^{109} pulseheight spectra at a position near to the gas inlet (*left*) and in the non-aged area (*right*). *top:* Fitted peak position of the taken spectra along the tube length.

A small Cd^{109} source, emitting $22\,keV$ photons, was used for these tests by placing the collimated source in different distances from the tube end. Figure 5.20 shows the results for a tube which suffered from the local ageing effect (ADC channel 6) whereas figure 5.21 show measurements taken on a reference tube and a tube from multilayer 2. This direct measurements clearly affirm the results from the last section, showing again a pulseheight degradation in the about first $30\,cm$ of the tubes on the gas inlet side.

5.7.4 Gas and Surface Analysis

When the local pulse height drop was detected, gas samples from both multilayers as well as from the fresh gas intake have been taken using evacuated stainless steel containers
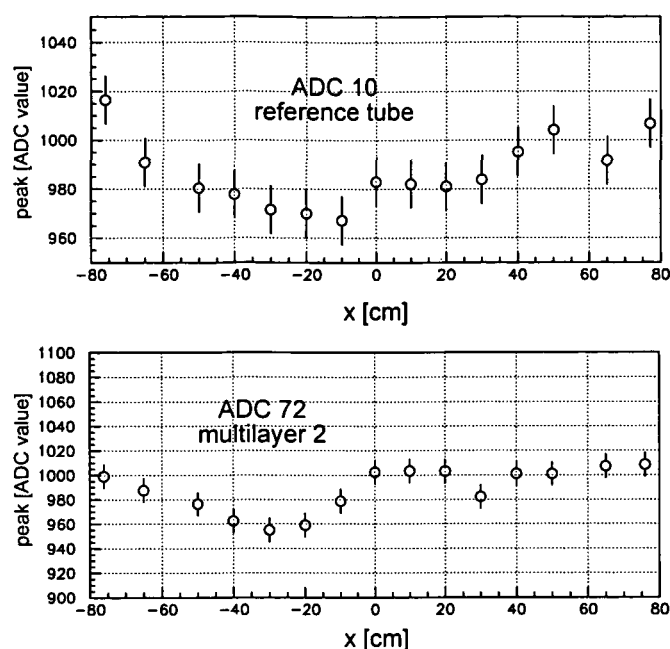
Figure 5.21: Fitted peak of Cd^{109} spectra taken at different positions along the tube length for a reference tube of multilayer 1 (*top*) and a tube of multilayer 2 (*bottom*)

for gas chromatography[13] analysis. Beside the peaks belonging to the components of the gas mixture (argon and carbondioxid) no other peaks, which would indicate a pollution, have been found. The used gas chromatography system was sensitive to gas impurities on the level of $100\,ppm$ according to the experiences of the experts.

After dismantling the ageing setup in May 2003 two tubes[14] of the recirculated multilayer have been opened to remove the anode wires and to take cathode samples. Analyzing the specimens of the anode wires with a scanning electron microscope (SEM) showed deposits in the shape of needles[15] sticking perpendicular out of the wire surface in the area near to the gas inlet side (left top image in figure 5.22). The length and density of the needles decreased when scanning along the wire in accordance to the pulseheight results. Applying energy dispersive X-ray analysis (EDX) to areas of the needle structure, showed beside the anode surface material (gold) a clear peak of silicon and oxygen (left bottom picture). As the drift gas is only containing argon, carbondioxid and to a small amount water and air, the measured spectra are a clear evidence that contaminants were present as major ingredient for building up the polymerisation structure. Similar EDX-spectra of the anode wire in an unaged region indicated just gold and small deposits containing carbon (right-hand side). The utilised EDX-measurement is sensible to all elements apart from hydrogen and helium and detects surface material for a layer thickness $>\ 0.2\,\mu m$.

---

[13]Gas chromatography is based on the different diffusion velocity of the gas constituents through a capillary column. The evolution of the signal coming from a sensor (here a sensor measuring the thermal conductivity) located at the outlet of the column shows the arrival peaks of the gas constituents.

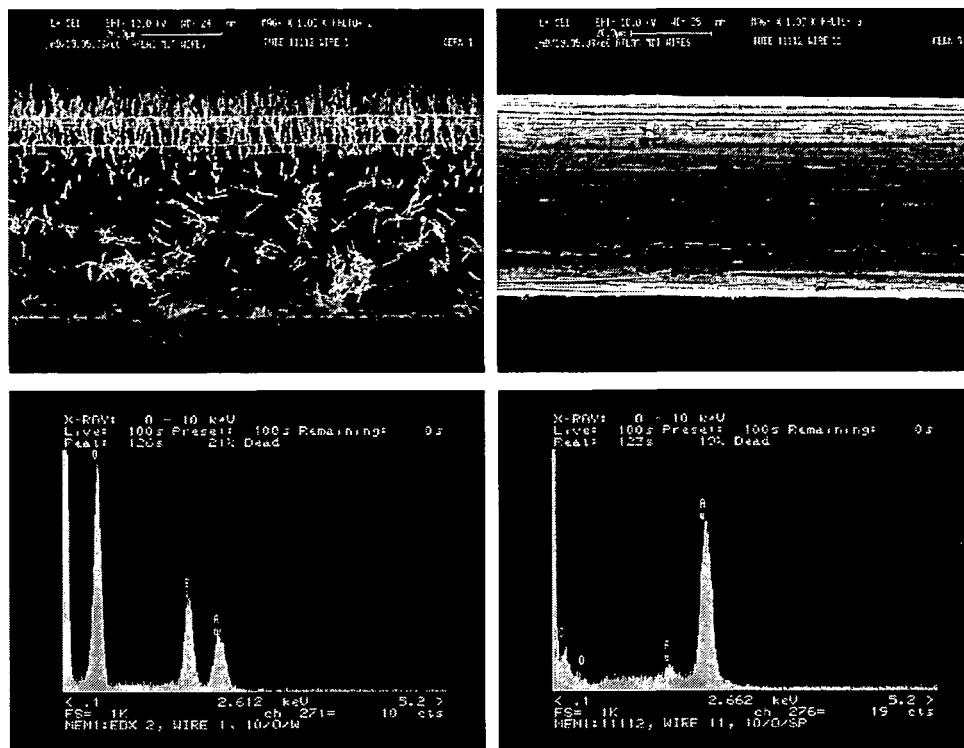[14]belonging to ADC channel 2 and 7

[15]5 to $7\,\mu m$ in length

Figure 5.22: *top:* Scanning electron microscope images of the anode wire taken in the aged region at $x \simeq -75\,cm$ (*left*) and in the non-aged region (*right*). The aged region shows a needle structure, which was identified by EDX-measurements (*bottom*) to consist of silicon and oxygen.

The method gives no direct information on chemical bonds and structure.

The chemical substance building the needle structure is likely silicon oxide coming from a gas contamination based on silicone, which is broken up in the gas amplification process and polymerises on the anode wire. This process depends on both the electric field and the irradiation level.

A lot of care was taken in the choice and treatment of the components which were in contact with the drift gas. Nevertheless the origin of the silicone contamination must come from industrial products which unintentionally were used within the recirculated gas system. Substances which come into question are sealants, greases (vacuum grease, low vapour pressure oil), mold release agents in mold injection processes and lubricants (i.e. used for metal machining). The search for the silicone source is topic of the next section.

The scanning electron microscopy occasionally showed spheres with a diameter between 2 and 3 μm sitting on the needle structure (see figure 5.23). Spot-specific EDX analysis identified them as made out of pure carbon. The origin of these spheres was not clear at the time of writing. One explanation is that they come from abrasion of the graphite in the bearings of the ATEKO turbine, but the manufacturer claims that such abrasion would not have the spherical shape of the observed particles.
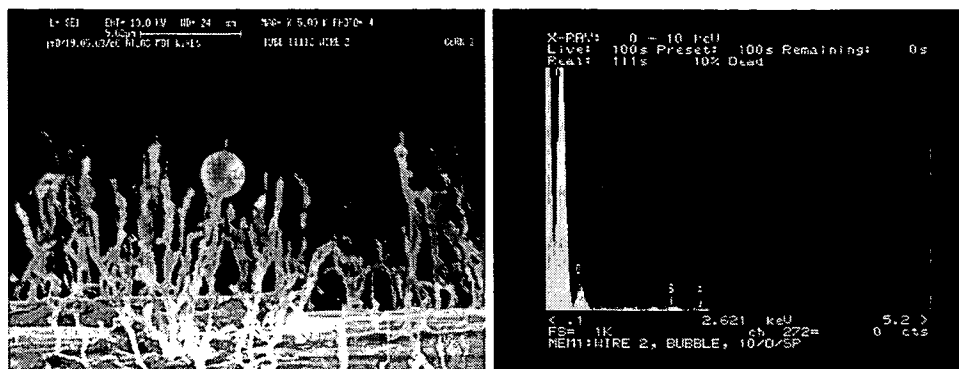
Figure 5.23: Spheres with a diameter of around $3\,\mu m$ were seen occasionally, which were attached to the needles (*left*). They have been found to be made out of carbon (*right*).
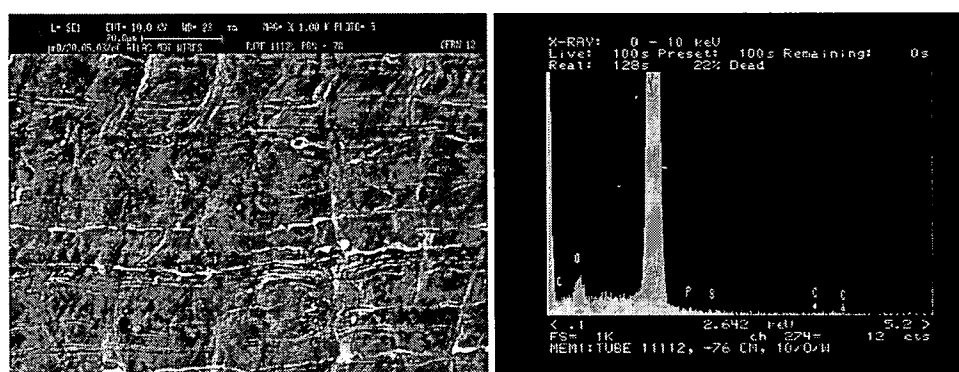

Figure 5.24: The surface analysis of the cathode surface, here shown for a specimen taken near the gas inlet ($x \simeq -75\,cm$), indicated only the element of the tube material aluminium plus oxygen from surface oxidation.

Finally the surface of cathode specimens along the opened tube were inspected with SEM. No contamination was found, the spectra showed only peaks of aluminium and oxygen (see figure 5.24). Thin uniform deposits would not be seen because the minimum detectable layer thickness of the measurement was about $0.2\,\mu m$.

5.7.5 Cleanliness Check of System

The components of the drift tubes, like the tubes itself, the endplugs and the MDT O-rings, have been excluded as silicone sources since these components have been identical between the two multilayers. The analysis[16] of the tubelets of the circulated multilayer showed strong variations in the level of cleanliness but no correlation with the strength of the observed ageing and moreover unclean tubelets were also found in multilayer 2.

---

[16]by optical inspection and by UV spectroscopy of high purity hexane, which was used to rinse the tubelets

EDX analysis of opened tubelets showed oxygen, carbon and a small amount of sulfur but no silicon (see figure 5.25).
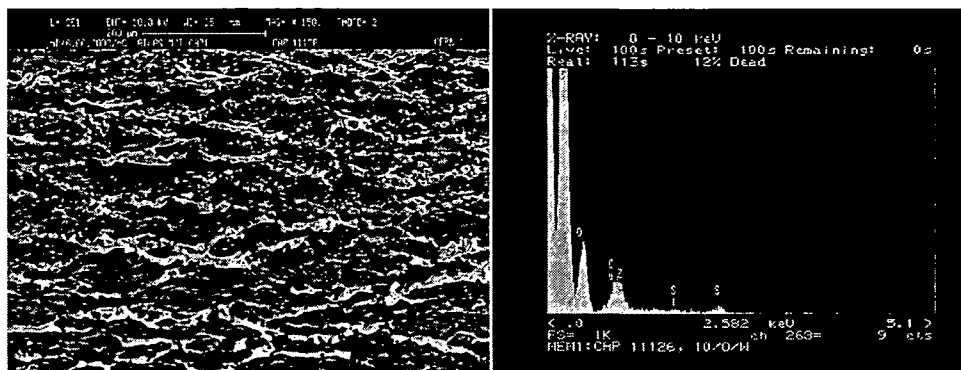

Figure 5.25: *left:* Electron microscope images of the inner surface of an opened tubelet. The impurities of this tublet were seen as black film already by eye. *right:* The EDX showed no indication of silicon.

In the circulation loop ("big loop") contaminations can strongly accumulate and the ultra-turbulent flow can remove more easily impurities from surfaces into the gas. The prototype system might even be more sensitive to contaminants in the system than in ATLAS as the gas volume is exchanged within $\sim 12\,s$ compared to one exchange per day in the final system.

After the aging test the recirculating gas system was dismantled into pieces to systematically inspect the cleanliness of the components. Rinsing some stainless steel pipes of the "big loop" as well as of the "small loop" with hexane and analyzing them with UV spectroscopy showed some impurities, but based on hydrocarbons.

One O-ring, which sealed a maintenance opening of a dewpoint meter was found to be lubricated with a silicone grease. Since the effect was there before the instrument was included into the small circulation loop to measure the water amount of the gas coming from multilayer 2 (see section 3.2.3), this impurity was excluded to be the main source of silicone for the observed ageing.

A sealing compound, located in the flanges of the big manual valve (number 15 in the gas diagram 3.2) used as main restriction in the "big loop", was analyzed by a company[17] with infrared spectroscopy. They identified the specimen to be made up of silicone rubber and moreover could verify that it contained volatile components in the form of low-molecular silicones. This sealing compound was assumed to be the main source of silicone at the time of writing this work.

On O-rings sealing the $50\,mm$ bellow pipes of the "big loop" oily residues have been found. IR spectroscopy of the same company as above identified the found lubricant as ester oil, but could not find any traces of silicone contamination.

Finally the turbine was disassembled by an expert from the manufacturer. Traces of

---

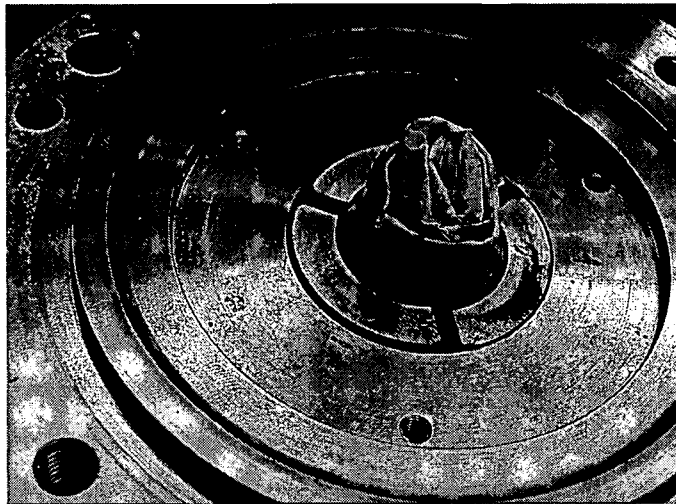[17]ACL GmbH, Hailfingen, 72108 Rottenburg, Germany

Figure 5.26: Observed lubricant on the back flange near the fixation holes for the disk of the radial bearing. Graphite powder coming from abrasion of the gas bearings can be seen as well.

graphite powder were found on several parts of the turbine, for instance in proximity of the thrust and radial bearings and also on one side of the gas outlet. The amount of powder concerning the time of operation was found reasonable by the expert. On the back flange, traces of grease were found near the threaded holes for the fixation of the disk of the radial bearings (see figure 5.26). This may be a lubricant used in drilling or threading the holes, which was not properly cleaned before assembly. This part was exposed to the circulating gas and therefore could pollute it. Again Uv analysis of hexane, rinsing the contaminated parts, showed that the oil was based on hydrocarbons and gave no evidence for silicone contamination.

Chapter 6

High Rate Studies

The MDT chambers will have to work under substantial background rates of photons and neutrons (see sec. 2.2). Within this work a production MDT chamber was exposed to an intense adjustable photon flux generated by a ^{137}Cs radioactive source. In combination with a $100\,GeV$ muon beam the detector performance could be studied in an environment similar as expected in ATLAS. In this chapter measurements on the maximal drift time change with the background level are presented. The applied analysis of the drift time spectra is explained (sec. 6.2) and the method of measuring the gamma background rates is given (sec. 6.1).

6.1 Gamma Background Rates

The $655\,GBq$ ^{137}Cs source at GIF emits photons of $660\,keV$ energy. Part of the photon flux is scattered on the walls and floor of the experimental zone which results in a broad lower-energetic spectrum in addition to the sharp primary peak. For a MDT the efficiency for photon detection is below $1\,\%$ [66]. The dominant interaction mechanism is via Compton scattering in the aluminium tube wall and to a lower extend in the operating gas. From measured tube count rates and the drawn tube current the average number of primary electrons created in the gas by one interacting photon can be calculated as

$$\bar{N}_{p.i.} = \frac{1}{G\,e}\frac{\bar{I}_{tube}}{\bar{R}_{tube}} \tag{6.1}$$

for a gas gain G, an average HV current per tube[1] $\bar{I}_{tube}$ and an average tube count rate $\bar{R}_{tube}$. Figure 6.1 shows the measurement results of the average current per tube for each multilayer versus the average background rate per tube, varied by applying different lead filters in front of the ^{137}Cs source. The slope of the applied linear fit corresponds therefore to the ratio $\frac{\bar{I}_{tube}}{\bar{R}_{tube}}$ of equation (6.1). With an assumed gas gain G of 2×10^4 an value of

$$\bar{N}_{p.i.} = 1260 \pm 20\% \tag{6.2}$$

---

[1] The current was measured collective for each chamber multilayer.

is determined for the average number of primary electrons per γ-photon for the BIS chamber in the study presented.
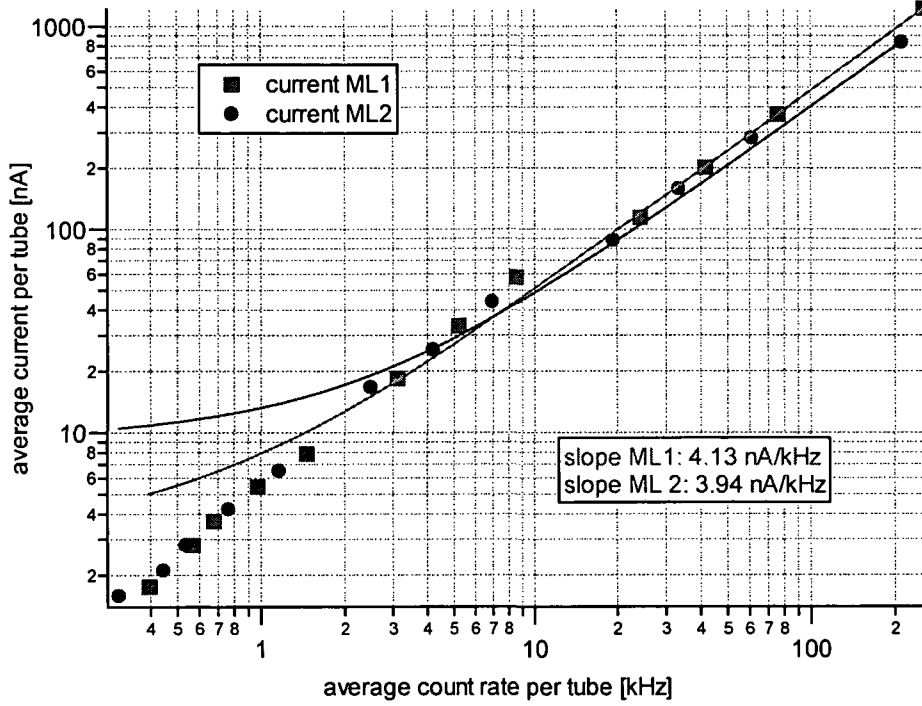

Figure 6.1: Average drawn current per tube versus average tube background rate. The HV current was measured for each multilayer in common and the count rates given here are averaged values of the tube rates of one multilayer.

The γ-rates were measured with the help of a "random" trigger, released by a pulse generator and therefore not correlated to the particles in the beam. The γ-rate determination is complicated by the fact that the used ASD-lite chip (see section 4.4.2) does not have a dead time large enough to ensure a single threshold crossing ("hit") per event as will be the case for the final ATLAS version. The average number of hits per γ-event was found to be around 3. To deal with multiple threshold crossings only the first hit found by the AMT in its match time window Δt_w is counted. Count rates calculated in this way as

$$R_{meas} = \frac{N_{first}}{n\,\Delta t_w} \tag{6.3}$$

with the total number of first hits N_{first} and the total number of events n, are too small since not only multiple hits from the same event, but also hits from a second event within the same AMT match window Δt_w are suppressed. This can be corrected in the following way. Assuming the true count rate is R, then the probability to observe one or more

hits in a single AMT match interval Δt_w is

$$\int_0^{\Delta t_w} R\,e^{-Rt}\,dt = 1 - e^{-R\,\Delta t_w} \tag{6.4}$$

From n accumulated events thus

$$n \cdot \left(1 - e^{-R\,\Delta t_w}\right) = N_{first} \tag{6.5}$$

contain on average one or more hits, which is equal to the measured number of first hits N_{first}. Using this expression with equation (6.3) gives the relation between the measured and true count rate:

$$R = -\frac{1}{\Delta t_w}ln(1 - \Delta t_w\,R_{meas}) \tag{6.6}$$

The ratio between the corrected count rate R and the measured value R_{meas} is shown in figure 6.2 for a AMT match window Δt_w of $1\,\mu s$.
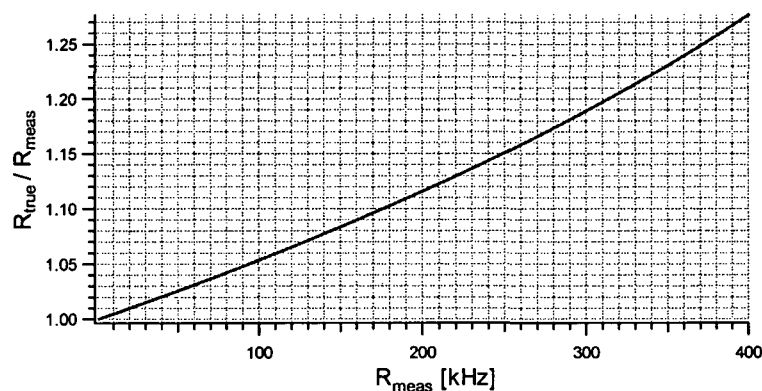

Figure 6.2: Ratio between the true count rate R_{true} and the count rate obtained by registering only the first hit in a fixed match time window Δt_w (shown here for $1\,\mu s$) released by a "random" trigger.

Individual γ-background rates obtained with the described method are indicated in figure 6.3 for the highest irradiation without any lead filter applied. The flux was by no means uniform across the $90\,cm$ wide BIS chamber. Unfortunately even in the much smaller region covered by the muon beam, γ rates varied by almost a factor 2. The observed non-uniformity of the radiation background was attributed to uneven shielding effects of several small size setups present for parasitic ageing between the ^{137}Cs source and the MDT setup.

Figure 6.4 shows measured beam-related particle rates during the SPS spill with no background radiation. There is a significant level of interactions outside the actual beam core. If a beam dimension of $15\,cm$ is assumed also in the vertical dimension with a flat distribution outside the beam core, one gets a ratio of roughly 20:1 for particle intensities in- and outside the beam region, taking into account the $170\,cm$ long drift tubes integrate the rate along their axis.
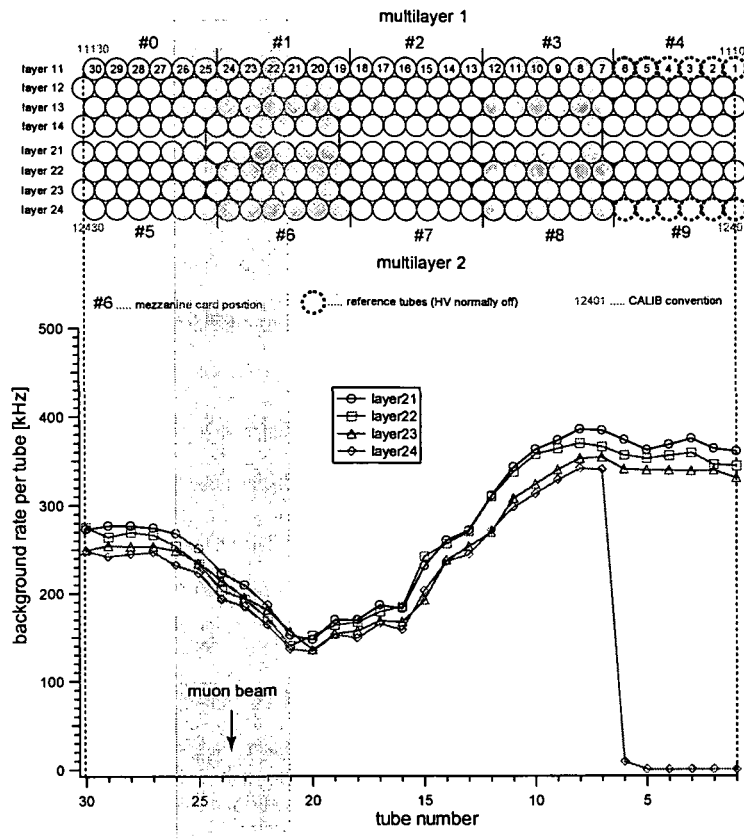
Figure 6.3: Photon background during the testbeam period for highest irradiation. The rate variation for the tubes in multilayer 2 is shown for each layer. In the region covered by the muon beam the background rate changed by almost a factor 2. The tube numbering within each layer corresponds to the cross section of the BIS chamber drawn above.

6.2 Analysis of Drift Time Spectra

The measurement principle of the MDTs is based on drift time measurements which allow to determine the radial position of the track with respect to the anode wire, when the space-driftime relation (rt-relation) is known. A drift time spectrum like in figure 6.5 is obtained by filling a histogram with the measured drift times of muons, assuming that they irradiated the tube uniformly. As the drift velocity increases for the nonlinear gas Ar-CO_2 near the anode, smaller drift times are more populated. The left histogram in figure 6.5 shows the raw drift time implying a spiky shape due to the $25\,ns$ uncertainty, caused by the hardware effect described in section 4.4.3. After subtracting the trigger pulse injection time of the additional mezzanine card this effect vanishes and the drift time spectra gets smooth (right histogram in figure 6.5). When evaluating drift time spectra with data from cosmic muons, like in the studies of the influence of water on the drift properties (see section 3.5.4), two further corrections have to be applied to each
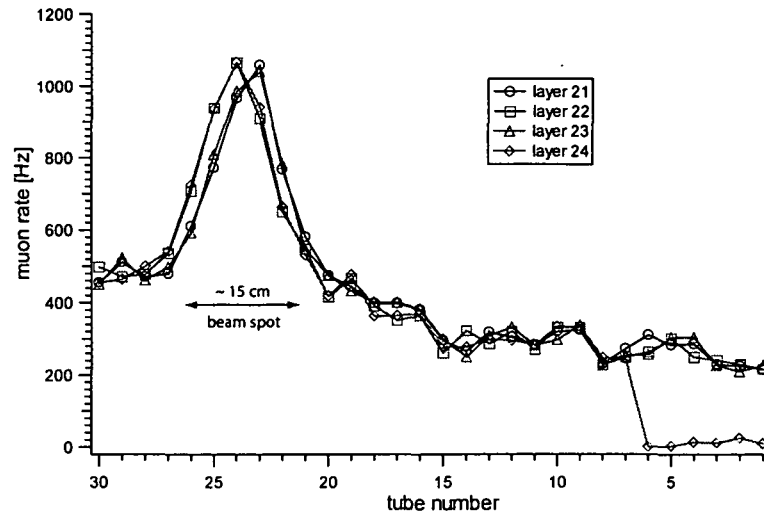
Figure 6.4: Particle count rate for the tubes of multilayer 2 during SPS spills with no photon background. An almost constant particle rate can be observed across the full chamber width outside the X5 beam core. The same "random" trigger method was applied as in the γ-rate measurements.

measured drift time t_{meas}:

$$t_{corr} = t_{meas} - t_{trig} + C + \frac{\Delta s}{c} - \frac{\Delta l}{c^*} \qquad (6.7)$$

where t_{trig} is the mentioned trigger pulse injection time, C a constant to shift the spectrum to positive values and $\frac{\Delta s}{c}$ is the time the trigger is delayed as the muon has to travel the distance Δs from the tube to the bottom hodoscope to release the trigger. The second correction term $\frac{\Delta l}{c^*}$ is the propagation needed from the signal to propagate the distance Δl from the muon crossing position to the readout side of the chamber. The drift time correction for cosmics needs therefore full muon track reconstruction with the cosmic hodoscope (see section 4.5.1).
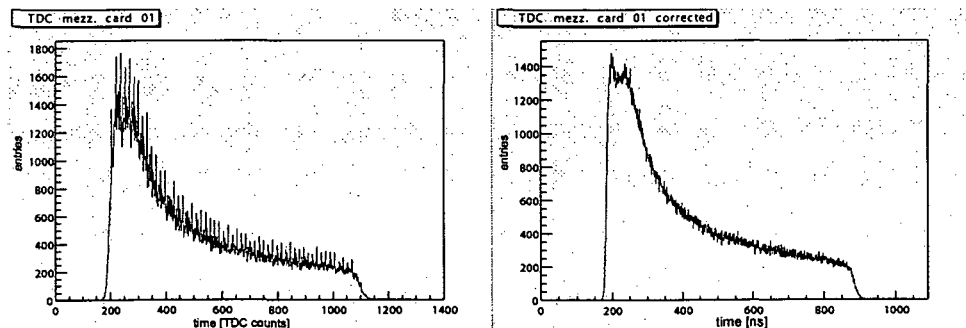

Figure 6.5: Raw drift time spectra (*left*) of testbeam data. After applying the correction for the pulse injection time the spiky shape of the spectrum disappears (*right*).

The maximal drift time t_{max} is defined as the time required by the electrons to drift from the internal tube wall up to the wire. It is an integral and robust figure of the gas drift properties and was obtained from the drift time spectrum in the following way: The rise time t_0 and the fall time t_f of the drift time spectra are determined with proper fits. The measured maximum drift time is then taken as the difference $t_{max} = t_f - t_0$. To obtain t_0 and t_f the rising edge of the spectrum was fitted with a Fermi function

$$f_0(t) = p_1 + \frac{p_2}{1 + e^{(t_0 - t)/p_3}} \qquad (6.8)$$

and the falling edge was fitted with a modified Fermi function taking into account the slope in the trailing part of the spectrum

$$f_f(t) = p_4 + \frac{p_5 + p_6 \cdot t}{1 + e^{(t - t_f)/p_7}} \qquad (6.9)$$

Such fits applied to the right histogram of figure 6.5 are indicated in figure 6.6. The uncertainty on the maximum drift time is dominated by the uncertainty on t_f that is larger than the one on t_0 due to the lower statistics in that region of the spectrum. The statistical uncertainty on t_{max} is of the order of $1\,ns$.
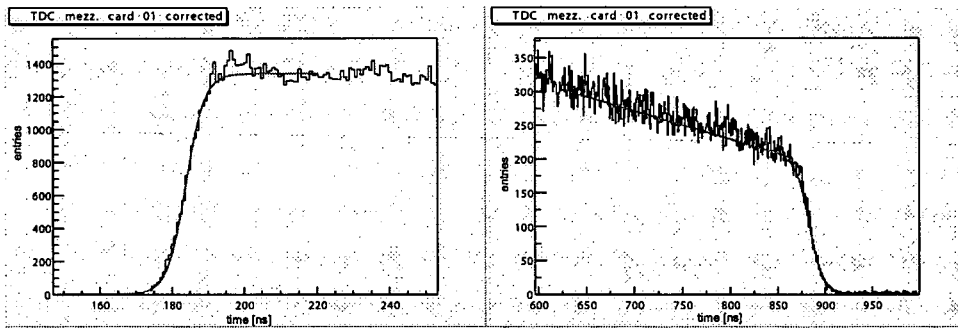

Figure 6.6: Performed Fermi fits to the rising (*left*) and falling edge (*right*) of the drift time spectrum of figure 6.5.

6.3   Temperature Dependence of the Maximum Drift Time

The maximum drift time t_{max} was determined according to the method described in the last section for various testbeam runs. The correlation between t_{max} and the average temperature of the multilayer during the run was studied. The experimental results are shown in figure 6.9. The maximum drift time decreases with the temperature, as the drift gas becomes faster with decreasing gas density. Applying linear regressions an average slope of $-2.3\,ns/K$ was found, which is in agreement with [38] (see also section 3.1.5).
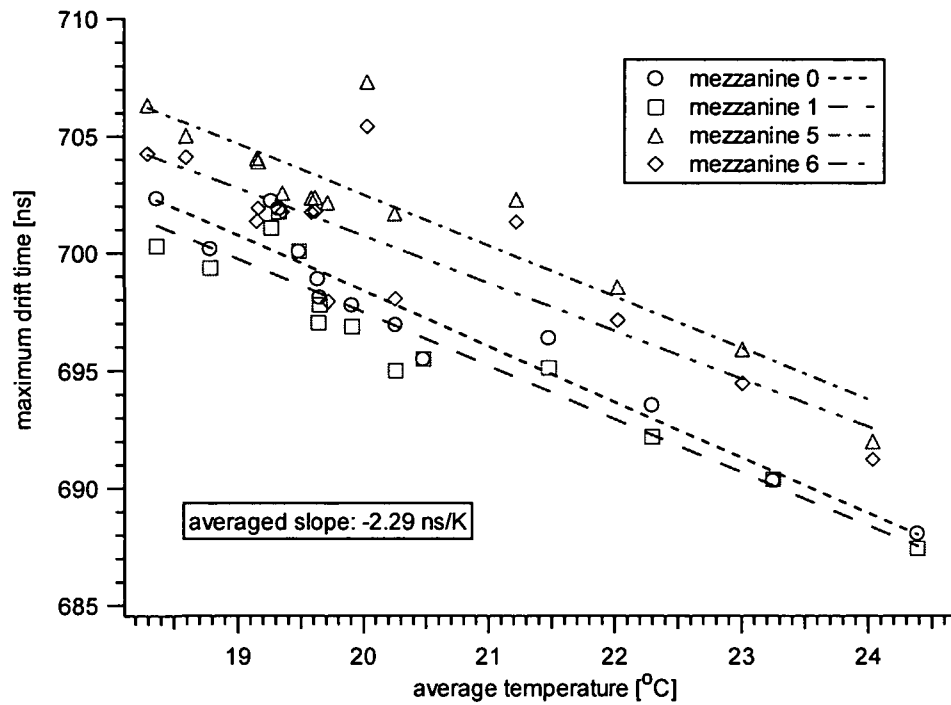
Figure 6.7: Maximum drift time t_{max} versus average multilayer temperature during the testbeam run. The maximum drift time shows a linear decrease with the temperature.

6.4   Maximum Drift Time with Gamma Background

The top histograms of figure 6.8 show drift time spectra accumulated for 24 tubes read by a mezzanine card (left) respectively of a single tube (right) as accumulated during testbeam for full background irradiation (γ-rate of $\sim 250\,kHz/tube$). The level to which the normal drift time spectrum is hidden by γ-hits depends both on the background count rate and on the fraction of events in which the tube under study was actually crossed by muon, which in turn depends on the size of the beam region and beam trigger.

It is difficult to perform precise fits to the rising and falling edge of high background spectra. Therefore the drift time spectra have to be "cleaned" from γ-hits first. Within this work[2] a simple track reconstruction was in use to separate muon hits from γ-hits: First The drift radii were calculated from the measured drift times with an approximate rt-relation. Then the four possible tangents were built to the calculated drift circles between each pair of tubes from the first and last layer which recorded a hit. Finally all these hits were kept, and assumed as muon hits, which had together with $m - 1$ other hits a distance less than d to one of the tangents. The bottom histograms in figure 6.8 show the spectra after applying the reconstruction algorithm. For the shown spectra only hits belonging to a tangent with eight hits closer than $d = 2.5\,mm$ to the tangent have been selected.

---

[2]Another method which unfolds the muon drift time spectrum from the overall spectrum is described in [67].
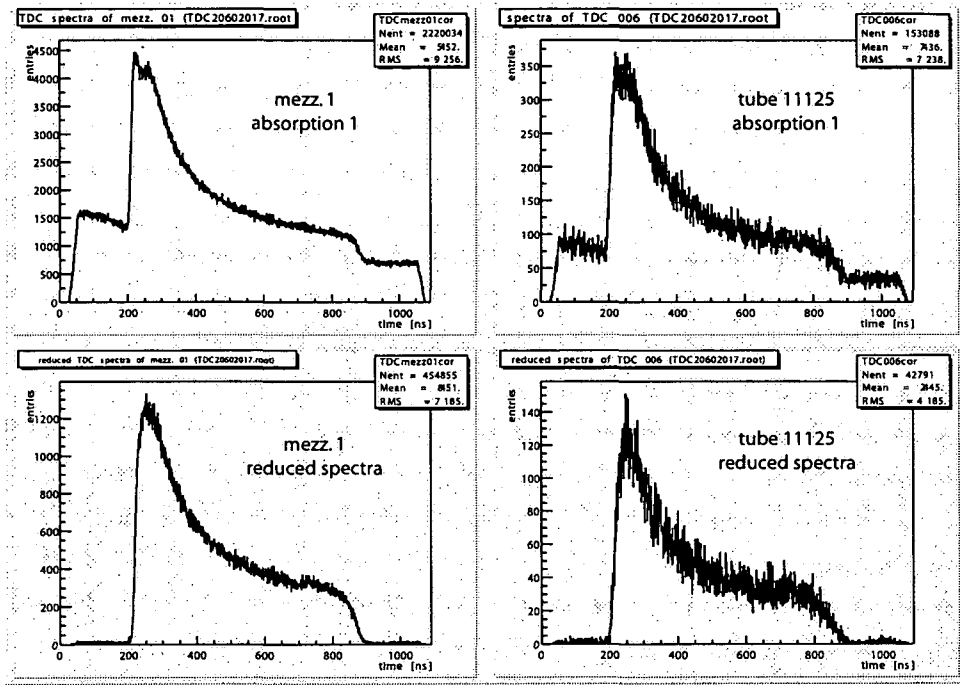
Figure 6.8: *top:* Drift time spectra from testbeam data for tubes belonging to one mezzanine card (*left*) and for a single tube (*right*). *bottom:* Spectra cleaned from γ-hits with a simple track reconstruction algorithm.

Figure 6.9 shows the results for t_{max}, gained from fits to the cleaned spectra at various background rates. The maximum drift time decreases linearly with increasing count rate with a slope of around $-0.13\,ns/kHz$. The change of t_{max} with background rate is caused by space charge, which changes the electric field. A model assuming a time-independent positive ion density is carried out in [23] and [67], which results are in agreement with the measurements presented here.

These measurements confirm that rate-dependent space charge effects are a dominant systematic effect contribution to the overall drift time errors. On the other hand these effects are understood and can be corrected for.
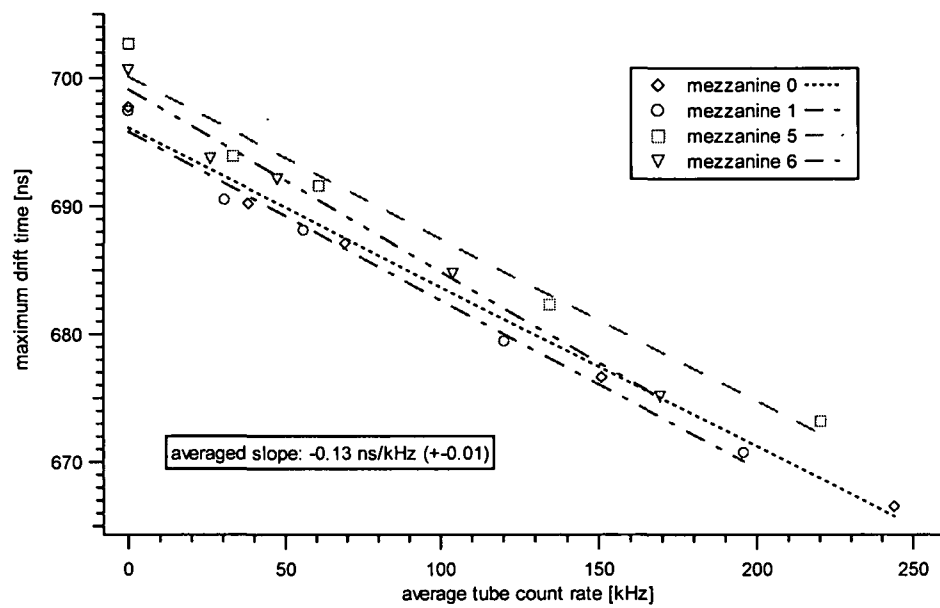
Figure 6.9: Maximum drift time t_{max} versus background rate. The maximum drift time shows a linear decrease with rate.

Chapter 7

Conclusion

This thesis addresses the study of the final systems operation of the precision muon chambers (MDT chambers) of the ATLAS Muon Spectrometer.

The design and realisation of the recirculating gas system prototype for the MDT chambers were presented.

A supervisory control for this system was developed, with particular attention to the specific safety measures of the custom-made turbine. The high-purity turbine, which will recirculate a very large gas detector volume of about $800\,m^3$ (at $3\,bar$) once per day, was commissioned for the first time within this work. For over one year the recirculating gas prototype was permanently operated and passed the system stability and behaviour test. It was demonstrated that the prototype system satisfies the MDT gas systems requirements.

The influence of the gas circulation on the ageing of MDT chambers due to high background radiation was studied in detail. For this purpose a standard MDT chamber, fully equipped with close to final front-end electronics, was connected to the gas prototype system and exposed to an intense photon flux generated by a ^{137}Cs radioactive source. One half of the chamber was supplied by the gas recirculation prototype whereas the second half was operated in a simple flushing gas mode. This was done to distinguish if possibly emerging ageing effects are related to circulation or result from other phenomenons. During this long-term study an average charge of about $250\,mC$ per centimeter anode wire was collected, which corresponds to four years of ATLAS operation with a conservative worst-case assumption for the expected background.

Reference measurements with cosmic muons have been performed regularly to monitor the detector performance during the ageing test. It was proven that the drift tubes connected to the open gas system did not suffer from the accumulated irradiation dose.

A local ageing effect was observed in the drift tubes operated in the recirculated gas mode. Track reconstruction of the cosmic muons and a detailed analysis of the pulseheight spectra showed a gas gain drop of up to $50\,\%$ in the first $\sim 30\,cm$ of the drift tubes on the gas inlet side. This observation was affirmed with direct pulseheight measurements along the chamber using a ^{109}Cd γ-source. Surface analysis with scanning electron microscopy showed needle-shaped deposits on the anode wire in the area concerned.

With energy dispersive X-ray analysis these deposits have been identified as silicon oxide polymerisation . This proved that external contaminations not related to the recirculated gas system caused the ageing effect.

On the other hand no ageing effect related to the baseline gas Ar-CO_2 (93:7) itself was observed, which demonstrated its compatibility with gas circulation in a long-term operation in a background irradiation environment similar to ATLAS.

All parts of the components of the circulation loop have been systematically checked for cleanliness. Although all effort was taken to select only highly clean components, a sealing compound located in the flanges of a manual valve could be identified as the main source of this silicone contamination. This work demonstrated how much attention must be paid in selecting, cleaning and mounting the gas components for the gas recirculation loop, since contaminations can accumulate to dangerous levels. Moreover the ultra-turbulent flow in the supply pipes to and from the turbine facilitates outgassing from surfaces in contact with the drift gas.

Finally drift time studies have been performed with testbeam muons under different background radiation levels. The decrease of the maximum drift time with the background rate was found to be in agreement with calculations, evaluating space charge effects.

Based on those studies the final gas system for the ATLAS Muon Spectrometer is ready for construction.
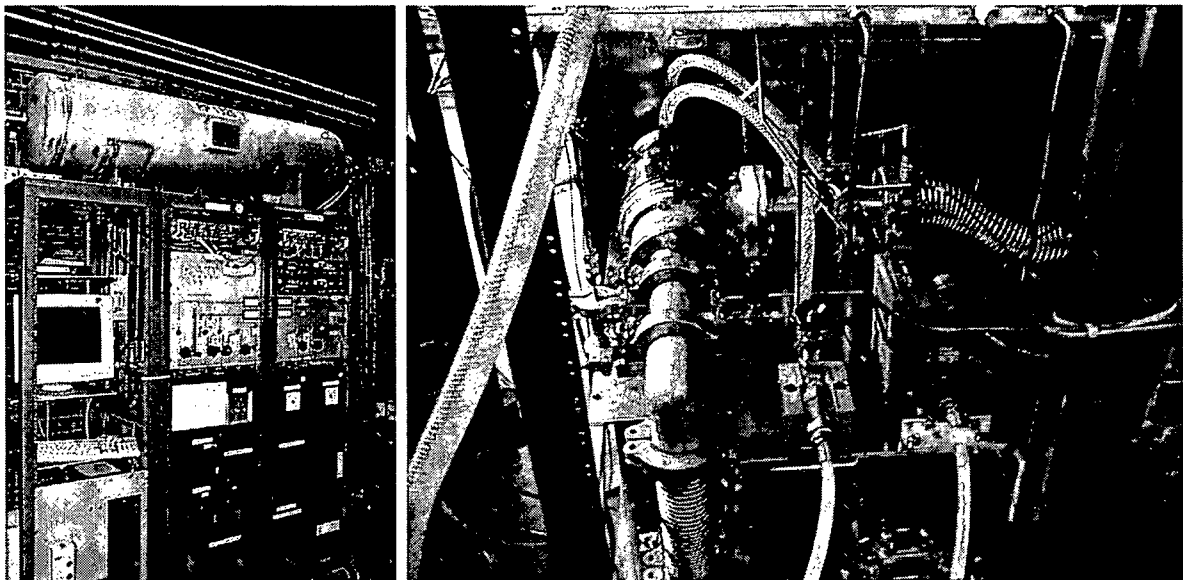
Appendix A

Pictures

Figure A.1: *left:* The racks of the recirculating gas prototype, which house the gas system and its control. The gas buffer of the "big loop" is mounted on top of the racks. *right:* The ATEKO turbine as it was installed in the gas rack. The gas enters in the pipe coming from the front and is thrust out to the pipe connected to the flange on the right hand side. The motor cable supplying the turbine with the 3 phases and the cooling water connection is also visible.
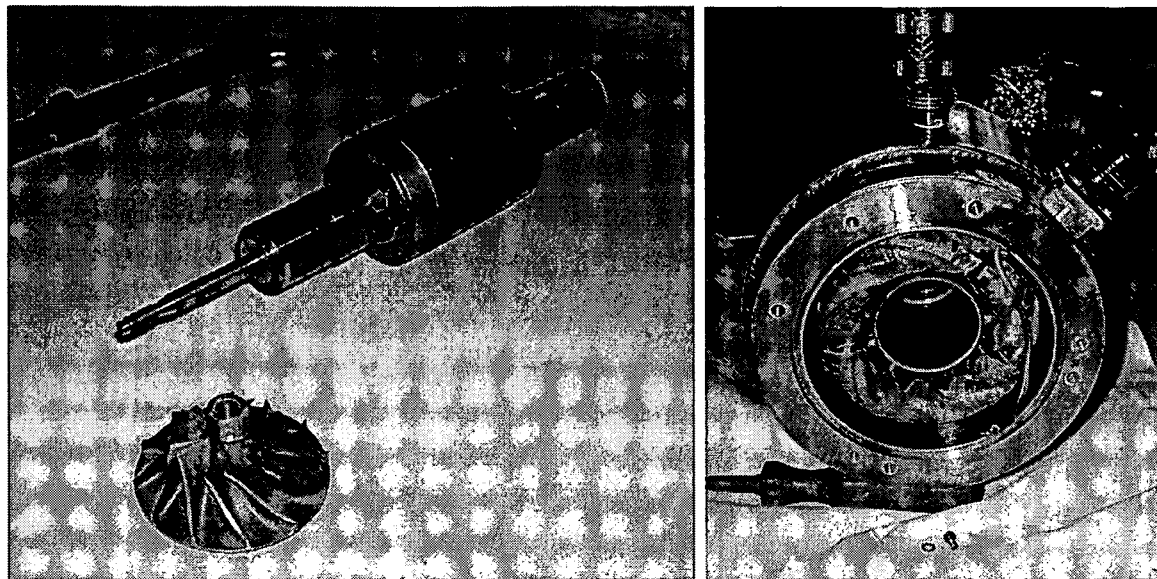
Figure A.2: *left:* Rotor shaft of the ATEKO turbine with the dismantled blade wheel. *right: Opened body of the turbine seen from the side of the thrust bearing. The stator windings and the separation sleeve are visible.*
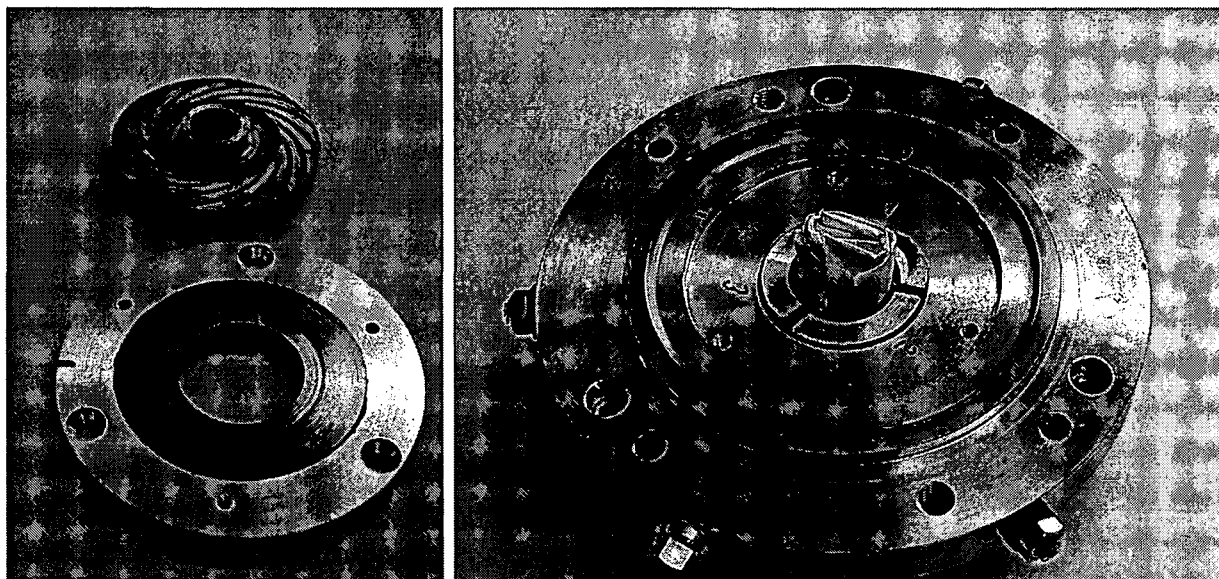

Figure A.3: *left:* Dismantled thrust bearing showing its spiral grooves. *right:* The back flange for the fixation of the disk of the radial bearings showed some grease after disassembling in the end of the ageing test.
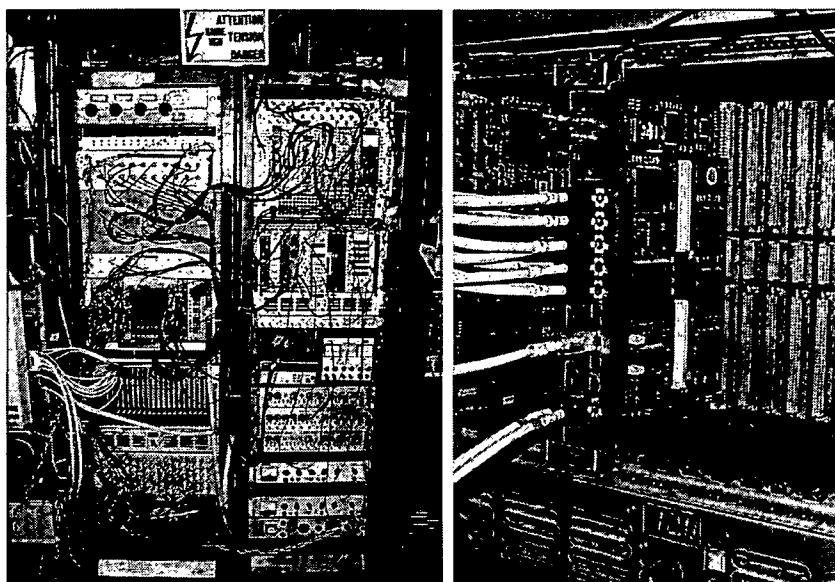
Figure A.4: *left:* The DAQ racks which include the cosmic trigger electronic, the Csm-0, the ADC readout and the HV supplies for chamber and hodoscope *right:* The Csm-0 module plugged into the VME crate and connected with LVDS cables to the front-end electronics.
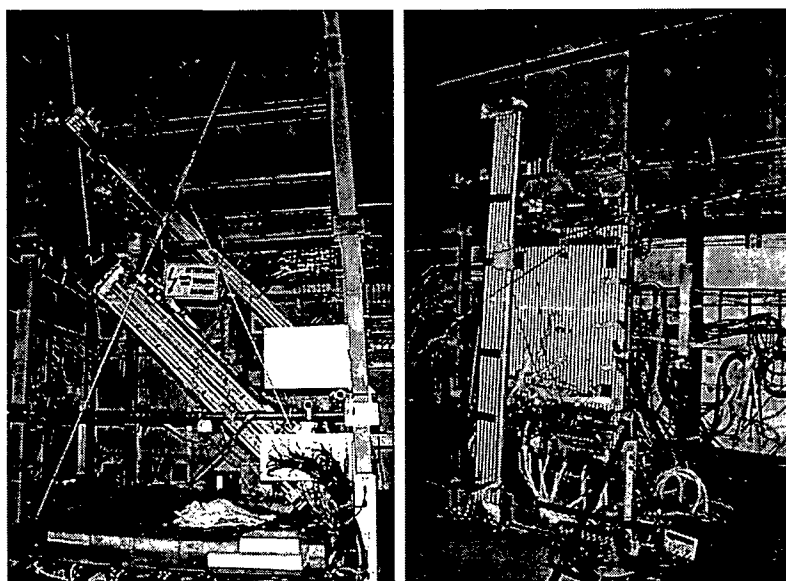
Figure A.5: *left:* The setup with the big hodoscope tower during ageing period 1. The long chamber consisting only of 24 tubes was operated by another group to test the serial gas connection. *right:* The light moveable setup as used during the testbeam period.

Figure A.6: The setup with inclined hodoscope layers during ageing period 2. The area of trigger acceptance of cosmic muons is highlighted.

Figure A.7: The LVDS Repeater PCB, which was designed within this work to provide the long distance communication between CSM-0 and front end electronics.

Appendix B
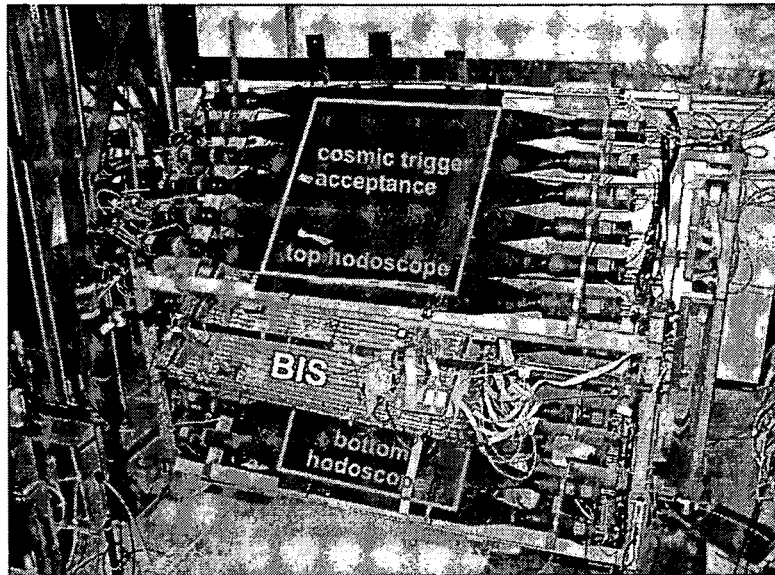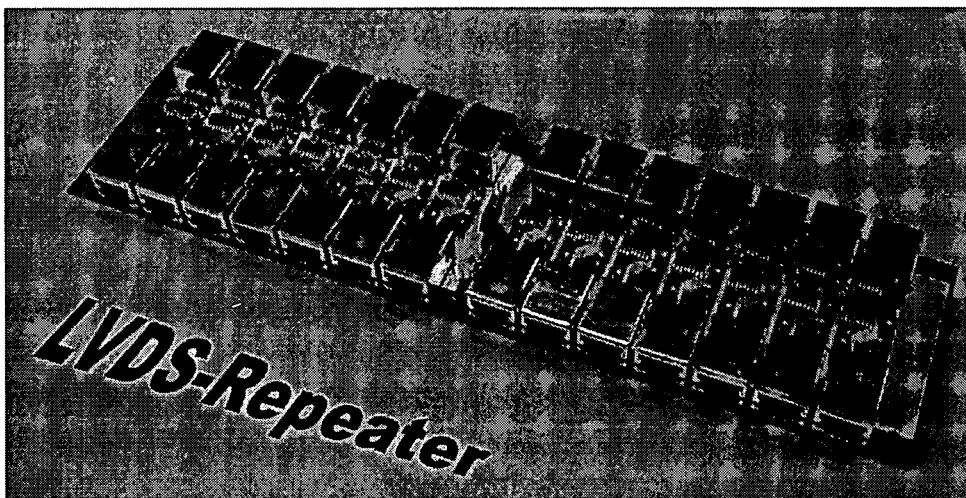
Glossary

ADC	Analog to Digital Converter
ALICE	A Large Ion Collider Experiment)
ASCII	American Standard Code for Information Interchange
ASD	Amplifier Shaper Discriminator chip
AMT	ATLAS Muon TDC
ATC	Argon Turbo Circulator
ATLAS	A Toroidal LHC ApparatuS
BIS	Barrel Inner Small MDT chamber
CAN	Controller Area Network
CASTOR	Cern Advanced STORage Manager
CDR	Central Data Recording
CERN	Centre Europèen pour la Recherche Nuclèaire
CMOS	Complementary Metal-Oxide Semiconductor
CMS	Compact Muon Solenoid)
CSC	Cathode Strip Chambers
CSM	Chamber Service Module
DAQ	Data AcQuisition
DATCHA	Demonstration of ATlas CHamber Alignment
DIN	Deutsche Industrie-Norm
DLL	Delay Locked Loop
EDX	Energy Dispersive X-ray
ELMB	Embedded Local Monitor Board
FIFO	First In First Out buffer
GIF	Gamma Irradiation Facility
HV	High Voltage
H8	sc Sps beam line in the north area at CERN
ISO	International Organisation for Standardisation
IR	InfraRed
JTAG	Joint Test Action Group

LEP	Large Electron Positron collider
LHC	Large Hadron Collider
LINAC	LINear ACcelerator
LVDS	Low Voltage Differential Signaling
MDT	Monitored Drift Tube
MROD	MDT Read-Out Driver
OLE	Object Linked Embedded
OPC	OLE for Process Control
PC	Personal Computer
PCB	Printed Circuit Board
PCI	Peripheral Component Interconnection
PS	Proton Synchrotron
PSB	Proton Synchrotron Booster
PTC	Positive Temperature Coefficient
QCD	Quantum Chromo Dynamic
QED	Quantum Electro Dynamic
ROB	Read Out Buffers
RPC	Resistive Plate Chambers
SCADA	Supervisory Control and Data Acquisition
SCT	Semi Conductor Tracker
SEM	Scanning Electron Microscopy
SMS	Short Message Service
SPS	Super Proton Synchrotron
TCP/IP	Transmission Control Protocol/Internet Protocol
TDC	Time to Digital Converter
TGC	Thin Gap Chambers
TPC	Time Projection Chamber
TRT	Transition Radiation Tracker
UV	Ultra Violet
VME	Versa Module Europa)
X5	SPS beam line in the west area of CERN

Bibliography

[1] Particle Data Group: *The Review of Particle Physics*, Phys. Rev. D66 (2002), web site: http://pdg.lbl.gov/

[2] R. Cahn, G. Goldhaber: *The Experimental Foundations of Particle Physics*, Cambridge University Press, 1989

[3] P.W. Higgs, Phys. Rev. lett. 12 (1964), p. 132; Phys. Rev. lett. 145 (1966), p. 1156

[4] The LEP Higgs working group, hep-ex/0107029 and hep-ex/0107030, July 2001

[5] Y. Baconnier et al.: *LHC: The Large Hadron Collider Accelerator Project*, CERN/AC/93-03 (1993)

[6] Cern Web Site: www.cern.ch

[7] Y. Baconnier et al.: *LHC: the Large Hadron Collider Accelerator Project*, CERN/AC/93-03 (1993)

[8] ATLAS Collaboration: *ATLAS Technical Proposal*, CERN/LHCC/94-43 (1994)

[9] CMS Collaboration: *CMS Technical Proposal*, CERN/LHCC/94-38 (1994)

[10] LHC-B Collaboration: *LHCb Technical Proposal*, CERN/LHCC 98-4 (1998)

[11] ALICE Collaboration: *ALICE Technical Proposal*, CERN/LHCC/95-71 (1995).

[12] ATLAS Inner Detector Community: *ATLAS Inner Detector Design Report*, CERN/LHCC/97-16&17 ATLAS TDR 4&5, April 1997

[13] ATLAS Collaboration: *Calorimeter Performance Technical Design Report*, CERN/LHCC/96-40, January 1997

[14] ATLAS LARG Unit: *Liquid Argon Calorimeter Technical Design Report*, CERN/LHCC/96-41, December 1996.

[15] ATLAS Tile Calorimeter Collaboration: *Tile Calorimeter Technical Design Report*, CERN/LHCC/96-42, 15 December 1996

[16] ATLAS Muon Collaboration: *ATLAS Muon Spectrometer Technical Design Report*, CERN/LHCC/97-22 ATLAS TDR 10, 1997

[17] ATLAS Level-1 Trigger Group: *Level-1 Trigger Technical Design Report*, ATLAS TDR-12, June 1998, updated 20 August 1998; ATLAS HLT/DAQ/DCS Group: *ATLAS High-Level Triggers, DAQ and DCS Technical Proposal*, CERN/LHCC/2000-17, March 2000, updated September 2000

[18] A. Schricker: *The Alignment System of the ATLAS Muon End-Cap Spectrometer*, PhD Thesis, CERN (2002)

[19] G. Viehhauser: *Detector Physics of the ATLAS precision muon chambers* PhD Thesis, CERN(1996)

[20] S. Ramo: *Currents induce in electron motion*, PROC. IRE 27, (1939) 584

[21] V. E. Battistoni et al.: *Background Calculations for the* ATLAS *Detector and Hall*, ATL-GEN-NO-94-10, CERN (1994)

[22] W. Riegler: *Limits to Drift Chamber Resolution*, PhD Thesis, CERN (1997)

[23] M. Aleksa: *Performance of the ATLAS Muon Spectrometer*, PhD Thesis, CERN (1999)

[24] W. Riegler, M. Aleksa: *Bipolar versus Unipolar Shaping of MDT Signals*, ATLAS Muon Internal Note, ATL-MUON-NO-99-03, CERN 1998

[25] M. Deile: *Optimization and Calibration of Drift-Tube Chambers for the ATLAS Muon Spectrometer*, PhD Thesis, Ludwig Maximilian Universität München (2000)

[26] S. Palestini: *Permeability of MDT end plugs*, ATLAS Muon Internal Communications, ATL-COM-MUON-2003-026, CERN (2003)

[27] M. Spegel: *On the lifetime of proportional counters*, PhD Theis, Freiburg, 1998

[28] M. Deile et al.: *Test Beam Studies of the Gas Mixtures ... for Drift Tubes*, ATLAS Muon Internal Note, ATL-MUON-NO-96-122, CERN 1996

[29] M. Kollefrath et al.: MDT *ageing studies using different cathodes*, ATLAS Muon Internal Note, ATL-MUON-NO-176, CERN 1997

[30] M. Kollefrath: *Entwicklung, Aufbau und Durchführung von Alterungsuntersuchungen an Driftröhren für das ATLAS-Myon-Spektrometer*, Doktorarbeit an der Albert-Ludwigs-Universität Freiburg, 1999

[31] MDT *Production Readiness Review*, CERN, June 1999

[32] C. Ramsauer: *Über den Wirkungsquerschnitt der Gasmoleküle gegenüber langsamen Eletronen*, Ann. Phys. **66** (1921) 546.

[33] V. Paschhoff: *Gasstudien für die Myonkammern des ATLAS Detektors*, Diplomarbeit an der Albert-Ludwigs-Universität Freiburg, 1994

[34] M. Kollefrath et al.: *Ageing studies for the ATLAS-monitored drift tubes*, Physics Research A 419 (1998) 351-356

[35] V. Paschhoff, M. Spegel: *Ageing studies for the ATLAS MDT's using Ar-CO₂ 90:10*, ATLAS Muon Internal Note, ATL-MUON-2000-004, CERN (1999)

[36] S. Kircher, M. Kollefrath, G. Herten, W. Mohr: *Parameter of MDT Ageing and Reanimation*, ATLAS Muon Internal Note, ATL-MUON-2001-012, CERN (2001)

[37] A. Romaniouk: *Choice of the materials for the construction of the TRT*, Atlas Internal Note, ATL-INDET-98-211, CERN (1998)

[38] F. Cerutti et al.: *Study of the MDT drift properties under different gas conditions*, ATLAS Muon Internal Note, ATL-COM-MUON-2003-022, CERN (2003)

[39] F. Hahn, S. Palestini, M. Treichel: *The MDT Gas System, a Design Report*, Atlas Internal Document, CERN 2002

[40] H. Kroha: *Quality Assurance and Control Reference Document for ATLAS MDT Chmaber Construction*, Atlas Internal Document version 1.1.3, CERN, May 1999

[41] I. Lehraus, M. Treichel: *Circulators for the ATLAS MDT Gas System*, ATLAS Muon Internal Note, ATL-MG-ER-00001, CERN 2000

[42] ATC a.s.: *Argon-Turbo-Circulator, Technical Description and Service Instructions*, Hradec Králové, Czech Republic, February 2001

[43] National Instruments Corporation, LABVIEW, graphical development environment for signal acquisition, measurement analysis, and data presentation, web site: http://www.ni.com/labview/, Version 6i

[44] ETM Corporation, PVSS, object-oriented process visualization and control system, web site: www.pvss.com, Austria

[45] ATC a.s.: *Argon-Turbo-Circulator, Technical Description and Service Intructions*, Hradec Kralove, Czech Republic, 2001

[46] H. Burckhart et al.: *Technical Description of the ATLAS ELMB*, Atlas Internal Document, ATIDCELMB-0001, CERN 2002

[47] I.E. Idelchik: *Handbook of Hydraulic Resistance*, CRC Press, ISBN 0-8493-9908-4, 3ʳᵈ edition, Moscow, 1994

[48] Control Techniques Drives Ltd: *Unidrive, Unidrive VTC, Unidrive LFT Installation Guide*, Part No 0447-0088, Issue 5, September 1998

[49] S. Agosteo et al.: *A facility for the test of large area muon chambers at high rates*, CERN Internal Note, CERN-EP-2000-031, CERN 2000

[50] F. Bauer et al.: *The First Precision Drift Tube Chambers for the ATLAS Muon Spectrometer*, ATLAS Muon Internal Note, ATL-MUON-NO-2001-015, CERN 2001

[51] G. Kaptis, C. Petridou, I. Tsiafis, J. Wotschak: *Mechanical design of the BIS module zero MDT chamber*, Atlas Muon Internal Note, ATL-MUON-98-242, CERN 1998

[52] Th. Alexopoulos et al. : *A Quality Assurance and Quality Control Procedure of the Monitored Drift Tubes for the BIS-Chambers of the ATLAS Muon Spectrometer*, IEEE Transactions oon Nuclear Science, Volume 49, nr. 5, p. 2484-2487, October 2002

[53] D. Sampsoinidis et al. : *Construction of the BIS MDT Chamber Modul 0*, ATLAS Internal Note, ATL-COM-MUON-2001-006, CERN, 2001

[54] R. Avramidou et al. : *X-ray tomograph study of the MDT-BIS chambers 'Beatrice' and 'Camille'*, Atlas Muon Internal Note, ATL-MUON-2003-001, October 2001

[55] A. Lanza: *Technical Description of the Components of the High Voltage Hedgehogs for the ATLAS MDT Chambers*, Atlas Muon Internal Note, October 2001

[56] E. Hazen et al. : *Signal Hedgehog PC Boards*, Atlas MDT Electroncs PDR - 2001-02-22, CERN (2001)

[57] C. Posch, E. Hazen, J. Oliver: *MDT-ASD, CMOS front-end for ATLAS MDT*, Atlas Internal Note, ATL-COM-MUON-2001-019, CERN, June 2001

[58] Y. Arai, T. Emura: *Development of a 24 channel TDC LSI for the ATLAS Muon Detector*, Nucl. Instrum. Methods Phys. Res., A 453 (2000) 365-71

[59] W. Riegler: *MDT Resolution Simulation Frontend Electronics Requirements*, Atlas Internal Note, ATL-MUON-NO-137, CERN (1997)

bibitemcsm J. Chapman, P. Binchi: *CSM Design Manual*, University of Michigan (2001)

[60] R. Ball, J. Chapman, J. Hollar, J. Kuah: *ATLAS MiniDAQ Reference Guide*, software reference manual, Univeristy of Michigan (2000)

[61] P. Bagnaia et al.: *Calib: a package for MDT calibration studies – User Manual*, Atlas Internal Note, ATL-COM-MUON-2002-004, Geneva (2002)

[62] L.D. Landau, J. Exp. Phys. (USSR) 8, 201 (1944).

[63] C. Cernoch, S. Zimmermann: *Evidence for Ageing in the longterm X5 MDT test*, Atlas Internal Note, Geneva 2003

[64] W.R. Leo: *Techniques for Nuclear and Particle Physics Experiments*, Springer-Verlag Berlin Heidelber New York, ISBN 3-540-57280-5, $2^n d$ edition, Berlin (1994)

[65] W. Diethorn: *A methane proportional counter system for natural radiocarbon measurements*, USAEC Report NY06628 (1956)

[66] s. Baranov et a.: *Gamma sensitivity of Pressurized Drift Tubes*, Atlas Internal Note, ATL-MUON-93-019, Geneva (1993)

[67] C. Cernoch et. al.: *MDT performance in the prescence of a high photon background*, Atlas Internal Note, ATL-COM-MUON-2003-024, Geneva 2003

Curriculum Vitae

Born in Vienna on 4th April 1974

Feb. 01 – Aug. 03   Selected for the "Austrian Doctoral Student Programme" at CERN (Geneva, Switzerland):
Doctoral thesis within the ATLAS Muon Collaboration about "Performance of ATLAS Muon Precision Drift Chambers in a High Radiation Environment".

Feb. 00 – Jan. 01   Alternative Civilian Service as ambulance man at the Austrian "Samariterbund"

Nov. 99   Degree of Diploma-Engineer at Vienna University of Technology

Oct. 93 – Nov. 99   Study of Physics at the "Technische Universität Wien". Diploma thesis: "Process Automatisation of a 3 dimensional Neutron Spinpolarimeter".

Sept. 88 – June 93   Technical High School for Electronics ("HTL Wien XXII")

Sept. 84 – June 88   High School ("Bundesrealgymnasium Wien XXI")

Sept. 80 – June 84   Primary School in Vienna

List of Publications

1. C. Cernoch: *Prozessautmatisierung eines 3 dimensionalen Neutronen-Spinpolarimeters*, diploma thesis, Vienna (1999)

2. Th. Alexopoulos et al.: *Extensive performance studies for the* ATLAS BIS-MDT *precision muon chambers*, IEEE Transactions on Nuclear Science, TNS-00003-2003.R1, 2003

3. C. Cernoch, S. Zimmermann: *First experience with the prototype* ATLAS MDT *gas circulation system at* GIF, Atlas Internal Note, ATL-COM-MUON-2002-023, Geneva 2002

4. C. Cernoch, S. Zimmermann: *Evidence for Ageing in the longterm X5* MDT *test*, Atlas Internal Note, Geneva 2003

5. C. Cernoch et. al.: *MDT performance in the prescence of a high photon background*, Atlas Internal Note, ATL-COM-MUON-2003-024, Geneva 2003

Curriculum Vitae

Born in Vienna on 4th April 1974

Feb. 01 – Aug. 03   Selected for the "Austrian Doctoral Student Programme" at CERN (Geneva, Switzerland):
Doctoral thesis within the ATLAS Muon Collaboration about "Performance of ATLAS Muon Precision Drift Chambers in a High Radiation Environment".

Feb. 00 – Jan. 01   Alternative Civilian Service as ambulance man at the Austrian "Samariterbund"

Nov. 99   Degree of Diploma-Engineer at Vienna University of Technology

Oct. 93 – Nov. 99   Study of Physics at the "Technische Universität Wien". Diploma thesis: "Process Automatisation of a 3 dimensional Neutron Spinpolarimeter".

Sept. 88 – June 93   Technical High School for Electronics ("HTL Wien XXII")

Sept. 84 – June 88   High School ("Bundesrealgymnasium Wien XXI")

Sept. 80 – June 84   Primary School in Vienna